

Fission products chemistry and scenario analysis of accident progression at Fukushima-Daiichi nuclear power station: Investigation of the Ba-Sr-Cs- Mo-O system

F. A. A. Grimmon

Master Thesis report
Reactor Physics and Nuclear Materials

Fission products chemistry and scenario analysis of accident progression at Fukushima-Daiichi nuclear power station: Investigation of the Ba-Sr-Cs-Mo-O system

by

F.A.A. Grimmon

In partial fulfillment of the requirements to obtain the degree of
Master of Science at the Delft University of Technology,
to be defended publicly on Tuesday 22-02-2022 at 2 pm.

| | | |
|-------------------|------------------------------|----------------------|
| Student number: | 4288718 | |
| Thesis committee: | Dr. A.L. Smith | TU Delft, supervisor |
| | Dr. ir. A.G. Denkova | TU Delft |
| | Prof. Dr. ir. R.J.M. Konings | TU Delft |

An electronic version of this thesis is available at <http://repository.tudelft.nl/>.

Abstract

The severe accident at the Fukushima-Daiichi Nuclear Power Station in 2011 has shown the necessity to study the impact of the release of hazardous fission products. This work investigates the Ba-Cs-Sr-Mo-O system, which contains some of the most abundantly produced fission products, as well as fission products that carry a great health risk on release. The study of this system is broken up into four subsystems: Ba-Sr-O, Ba-Mo-O, Sr-Mo-O and Ba-Cs-Mo-O. A literature study into the ternary Ba-Sr-O system, including existing thermodynamic models, showed the formation of no stoichiometric ternary compounds due to the mutual miscibility of Ba and Sr. Despite this mutual solubility, a miscibility gap is shown to be present in the solid region of the binary BaO-SrO phase diagram below a certain temperature. Thermogravimetric differential scanning calorimetry (TG/DTSC) investigations of the BaMoO₄ – MoO₃, SrMoO₄ – MoO₃ and BaMoO₄ – Cs₂MoO₄ pseudo-binary systems revealed likely compositions for the eutectic equilibria at $0.792 \leq x(\text{MoO}_3) \leq 0.80$, $0.806 \leq x(\text{MoO}_3) \leq 0.82$ and $0.909 \leq x(\text{Cs}_2\text{MoO}_4) \leq 0.976$, respectively. These measurements also allowed for the development and optimisation of a new thermodynamic model of the BaMoO₄ – Cs₂MoO₄ system using the CALPHAD (Calculation of Phase Diagram) method. Syntheses of BaMoO₄, BaMo₃O₁₀, Ba₂MoO₅ and BaCs₂(MoO₄)₂ were successfully completed. A partially successful synthesis method was developed for Ba₃MoO₆ that needs further optimisation. The novel synthesis of Ba₂MoO₅ allowed for solution calorimetry measurements to be performed, leading to the determination of its standard enthalpy of formation $\Delta_f H_m^\circ(298.15\text{K}, \text{Ba}_2\text{MoO}_5) = -(2169.0 \pm 14.7) \text{ kJ/mol}$. Vapour pressure studies of BaMoO₄ by means of Knudsen Effusion Mass Spectrometry (KEMS) gave insight into the composition of the vapour formed above BaMoO₄ after vaporisation. The results showed extensive influence of fragmentation reactions and only a small amount of congruent evaporation, indicated by the high partial pressure of BaO(g) and other binary molecules. A partial reduction of the BaMoO₄ sample to BaMoO₃ could have occurred, but this cannot be confirmed due to the full evaporation of the KEMS sample. Further studies are required to investigate a potential reduction.

Acknowledgements

Most of all, I would like to thank Anna Smith for being such a kind, flexible and attentive supervisor. She molded the project to suit my areas of interest and was always available to answer the many questions that I had throughout this process. Thank you to John Vlieland for teaching me how to work in the lab and for walking all the way back with me when I had (once again) locked my keys inside. Thank you to Dick de Haas for helping me with my computer problems. Thank you to Gilliam van Oudenaren, Wouter van Burik, Thomas Dumaire and Andries van Hattem for providing some welcome face-to-face conversations during these Covid times and also thank you to Gilliam for reading my thesis (here you go, I said it).

Contents

| | |
|---|------------|
| Abstract | i |
| Acknowledgements | iii |
| Introduction | 2 |
| 1 Literature Review | 7 |
| 1.1 Ba-Sr-O system | 7 |
| 1.1.1 Phase diagram | 7 |
| 1.1.2 Lattice parameters vs. composition | 10 |
| 1.1.3 Volatility studies | 11 |
| 1.1.4 Ba-O, Sr-O and Ba-Sr systems | 13 |
| 1.1.5 Structural data of the compounds | 14 |
| 1.2 Ba-Mo-O system | 15 |
| 1.3 Ba-Cs-Mo-O system | 15 |
| 1.4 Sr-Mo-O system | 15 |
| 2 Theoretical Background | 17 |
| 2.1 Solid state synthesis | 17 |
| 2.2 X-ray Diffraction (XRD) | 18 |
| 2.2.1 Theory: Bragg's Law and atomic planes | 18 |
| 2.2.2 Powder X-ray Diffraction | 19 |
| 2.2.3 Method | 21 |
| 2.2.4 Analysis | 21 |
| 2.3 Thermogravimetric differential scanning calorimetry (TGDCS) | 23 |
| 2.3.1 Theory | 23 |
| 2.3.2 Method | 25 |
| 2.4 Solution calorimetry | 26 |
| 2.5 Knudsen Effusion Mass Spectrometry (KEMS) | 29 |
| 2.5.1 Knudsen Effusion cell | 29 |
| 2.5.2 KEMS set-up | 30 |
| 2.5.3 Partial pressure calculation | 33 |
| 2.6 CALPHAD modelling | 35 |
| 2.6.1 Solid phase: the Compound Energy Formulism (CEF) | 36 |
| 2.6.2 Liquid phase: the Ionic two-Sublattice Model (I2SL) | 37 |
| 2.6.3 Gaseous phase: ideal mixture | 38 |

| | | |
|----------|---|------------|
| 3 | Experimental, Results and Discussion | 39 |
| 3.1 | Ba-Mo-O system: investigation of the BaMoO ₄ - MoO ₃ pseudo-binary section | 40 |
| 3.1.1 | Syntheses and structural characterisation | 40 |
| 3.1.2 | Thermodynamic property measurements on Ba-Mo-O compounds | 50 |
| 3.1.3 | Phase diagram investigations by DSC | 51 |
| 3.2 | Ba-Cs-Mo-O system: investigation of the BaMoO ₄ - Cs ₂ MoO ₄ pseudo-binary section . . | 57 |
| 3.2.1 | BaCs ₂ (MoO ₄) ₂ synthesis and structural characterisation | 57 |
| 3.2.2 | Phase diagram investigations by DSC | 58 |
| 3.2.3 | BaMoO ₄ - Cs ₂ MoO ₄ CALPHAD Model | 64 |
| 3.3 | Sr-Mo-O system: investigation of the SrMoO ₄ - MoO ₃ pseudo-binary section | 67 |
| 3.3.1 | Phase diagram investigations by DSC | 67 |
| 4 | Vapour pressure studies: results and discussion | 72 |
| 4.1 | Literature study results | 72 |
| 4.2 | Experimental results | 73 |
| 4.2.1 | Method | 73 |
| 4.2.2 | Relative ion intensities | 73 |
| 4.2.3 | Determination of appearance energies and parent molecules | 74 |
| 4.3 | Partial pressure calculations | 78 |
| 4.4 | Reaction pathways | 80 |
| 4.5 | TGDSC experiment BaMoO ₄ | 81 |
| | Bibliography | 89 |
| | Appendices | 98 |
| A | Partially successful synthesis methods | 99 |
| A.1 | BaMo ₃ O ₁₀ | 100 |
| A.1.1 | Variation 2: partially successful | 102 |
| A.2 | Ba ₂ MoO ₅ | 103 |
| B | Additional Rietveld and PowderCell analyses | 106 |
| B.1 | BaMo ₃ O ₁₀ | 106 |
| B.2 | Ba ₂ MoO ₅ | 108 |
| C | Outlying data point discussions | 109 |
| C.1 | Ba-Mo-O system | 109 |
| C.2 | BaMoO ₄ - Cs ₂ MoO ₄ system | 111 |
| C.3 | Sr-Mo-O system | 114 |
| D | Neumann-Kopp Approximation | 116 |
| D.1 | Neumann-Kopp Approximation | 116 |

Introduction

The analysis of the composition of nuclear fuel is a very complicated process. Irradiated UO_2 produces over 40 fission products [57] that react to form a multitude of different compounds and phases. The behaviour of these fission products is highly dependent on the condition of the surrounding fuel and changes with varying temperature, pressure, oxygen potential, redox conditions and the presence of other elements and compounds. The severe accident at the Fukushima-Daiichi Nuclear Power Station in 2011 has shown the necessity to study the impact of the release of these fission products and the potential health implications that arise when they do. To this effect, the TCOFF¹ project of the OECD/ NEA² was initiated. It consists of a network of research facilities and academic institutions that contribute to thermodynamic databases by doing research on the behaviour of fission products from normal power plant operation to severe accident (SA) conditions. The TCOFF project seeks to give a much better understanding of the (phase) composition and release behaviour of fission products in SA conditions, as well as thermodynamic information on these compounds that is applicable to many other areas of research.

Table 1: Abundance of fission product elements in LWRs [94]

| FP element | Fission yield | FP element | Fission yield | FP element | Fission yield |
|------------|---------------|------------|---------------|------------|---------------|
| Zr | 0.326 | Ce | 0.154 | Te | 0.026 |
| Nd | 0.303 | Ru | 0.142 | I | 0.011 |
| Mo | 0.248 | Ba | 0.084 | Nb | 0.008 |
| Xe | 0.241 | Sr | 0.078 | Eu | 0.002 |
| Cs | 0.182 | La | 0.065 | Sb | 0.0003 |

This thesis contributes to the TCOFF project by investigating the fission product sub-system Ba-Sr-Cs-Mo-O. This subsystem contains some of the most abundantly produced fission products (table 1), as well as fission products that carry a great health risk if they are released into the environment [67, 99, 106].

Strontium has three fission product isotopes (Sr - 88, 89 and 90) that, because of their chemical similarity, act as calcium mimics and can be incorporated in bones. The long half-life of especially Sr-90 (28.70 years) causes prolonged radiation exposure, which can lead to leukaemia, bone cancer or thyroid tumours [13, 18, 19, 90].

Caesium isotopes (Cs – 133, 134, 135 and 137) are produced at a high yield. Part of the caesium that is produced is released as the water-soluble compound CsI, which can contaminate the water and hence

¹Thermodynamic characterisation of fuel debris and fission products based on scenario analysis of severe accident progression at Fukushima-Daiichi nuclear power station

²Organisation for Economic Co-operation and Development and the Nuclear Energy Agency

the soil around a disaster site very easily [77, 79]. The long half-life of especially Cs - 137 (30.17 years) means that its influence on the contaminated area is long-lived. It is reported that the gamma-dose rate above a contaminated area with caesium 20 years later, is still one fifth of what it was initially [79].

Molybdenum and barium are both dangerous at high exposure levels and are produced at a relatively high yield [94, 99]. Barium only poses a danger as a soluble compound, which can cause cardiac irregularities, shortness of breath and paralysis [33, 97]. However, barium tends to form precipitates (either metallic or oxides as will be discussed below) during fuel irradiation, therefore it is less likely to form a health risk after its release. The half-lives of the barium fission product isotopes are quite short, Ba - 138 is stable, Ba - 139 and 140 have half-lives of 83.06 minutes and 12.75 days respectively. Molybdenum dust or fumes are toxic and can cause headaches, joint pains or death at chronic high exposures [41]. Four of its fission product isotopes are stable (Mo - 95, 97 and 98) or nearly stable (Mo - 100, $t_{1/2} = 8.5 \cdot 10^{18}$ years). The last, Mo - 99, has a short half-life of 2.75 days. Neither barium nor molybdenum isotopes are likely to cause long-term radiation exposure, but their radiation chemistry is interesting to study because of their complex behaviour in nuclear fuel and their association with the other problematic fission products in the form of oxide precipitates.

To properly understand the health hazards of this system of fission products, it is important to study their chemical state under normal and severe accident conditions, because it has an impact on the properties of the fuel (such as thermal conductivity and swelling) and it influences the chemical properties of other fission products with which they associate. The chemical state also determines the release kinetics and volatility of the compounds within the Ba-Sr-Cs-Mo-O system and are thus of primary interest [108].

The composition of formed phases within the fuel pellet depends mostly on burnup (and thus oxygen potential), the initial composition of the fuel, the neutron energy spectrum of the reactor, fissile material composition and temperature gradients in the fuel pin [68]. Burnup is a measure of fuel depletion and describes the amount of energy that has been extracted from nuclear fuel. It is measured in %FIMA (fissions per initial metal atom) or in units of GWd/tU (gigawatt days per metric ton of heavy metal). A higher burnup gives rise to a higher oxygen potential (figure 1) as more oxygen is released from the (U,Pu)O₂ fuel. The higher oxygen potential allows more compounds in the fuel to form oxides and thus influences its composition.

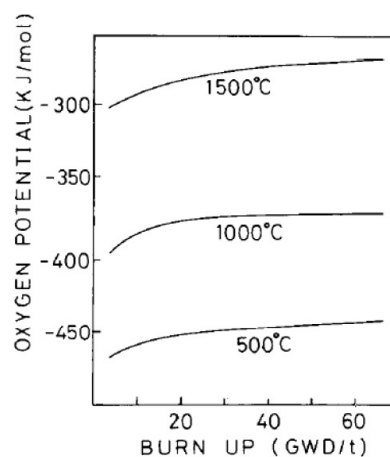


Figure 1: Change in oxygen potential as a function of burnup for three temperatures in LWRs [57]

Brillant [14] explores a study done by Ducros et al. [35] that describes release fractions of various fission products from enriched UO₂ and mixed-oxide (MOX) fuel pellets in a pressurised water reactor (PWR) in medium burnup scenarios (40-50 GWd/tU). They give the following classification of fission products (FPs):

1. Volatile – FPs that are rapidly released, mainly because they diffuse through fuel grains (Cs, I, Te, Sb)
2. Semi-volatile – FPs with large release fractions depending on the redox conditions of the surrounding fuel (**Mo**, Rh, **Ba**)

3. Low-volatile – FPs with low release fractions independent of redox conditions or temperature (Ru, Ce, Np, **Sr**, Eu)
4. Non-volatile – FPs that are only released in the case of fuel vaporisation (Zr, Nb, La, Nd)

Caesium falls under the volatile category and was reported to have a release fraction of 93-100%, depending on the burnup (from 38.3 – 49.4 GWd/tU). Molybdenum and barium are both semi-volatile, but their release fractions are highly dependent on the atmosphere under which the fuel pellets were heated. Molybdenum has a release fraction of 92-100% under oxidising conditions and 33 – 49% under reducing conditions. Barium is the opposite; it has a higher release fraction under reducing conditions: 80-85% vs. 38-55% under oxidising conditions. The release of barium starts around 2000K in most tests and is significantly slower than the release of caesium and molybdenum. The release fraction of strontium was below 6% and is therefore classified as a low-volatile fission product [14, 35, 43, 45].

In order to further analyse the behaviour of these fission products in nuclear fuel, it is useful to consider Kleykamp's [67] classification system:

1. Fission gases and other volatile fission products: Kr, Xe, Br, I
2. Fission products forming metallic precipitates: **Mo**, Tc, Ru, Rh, Pd, Ag, Cd, In, Sn, Sb, Te
3. Fission products forming oxide precipitates: Rb, **Cs**, **Ba**, Zr, Nb, **Mo**, Te
4. Fission products dissolved as oxides in the fuel matrix: **Sr**, Zr, Nb and the rare earth elements Y, La, Ce, Pr, Nd, Pm, Sm

Kleykamp reports a continuous transition between groups 2 and 3, because some fission product oxides have similar oxygen potentials to the nuclear fuel. Imoto [57] investigated the compositions of barium, strontium, caesium and molybdenum compounds as a function of oxygen potential shown in figure 2. The vertical line represents an oxygen to metal ratio of O/M = 2.0.

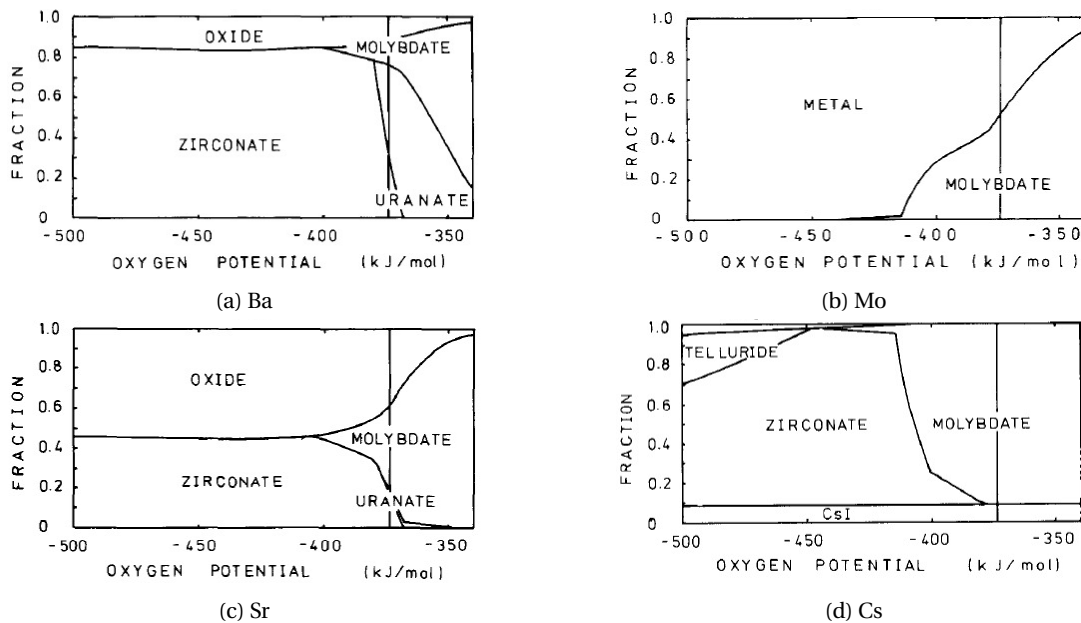


Figure 2: Chemical form of fission products Ba, Mo, Sr and Cs in LWR fuel [57]

Most importantly for this thesis, compounds in the Ba-Sr-Cs-Mo-O system form the so-called grey phase (because of its grey colour in microscopic pictures) in the form of $(\text{Ba}_{1-x-y}, \text{Sr}_x, \text{Cs}_y)(\text{Zr}, \text{U}, \text{Pu}, \text{Mo}, \text{RE})\text{O}_3$ (RE = rare earth elements at high burnup) [24, 67, 68, 84, 113]. The grey phase is a complex multicomponent oxide phase that forms at low oxygen potentials and consists of a large variation of compounds. The formation of this phase is mostly due to the low solubility of barium in the nuclear fuel matrix (because of its large ionic radius). Figure 3 shows two microscopic images of the grey phase reported by Lucuta et al. [84] and Hiezl et al. [55], both produced during the analysis of UO_2 SIMFUEL (simulated high-burnup nuclear fuel).

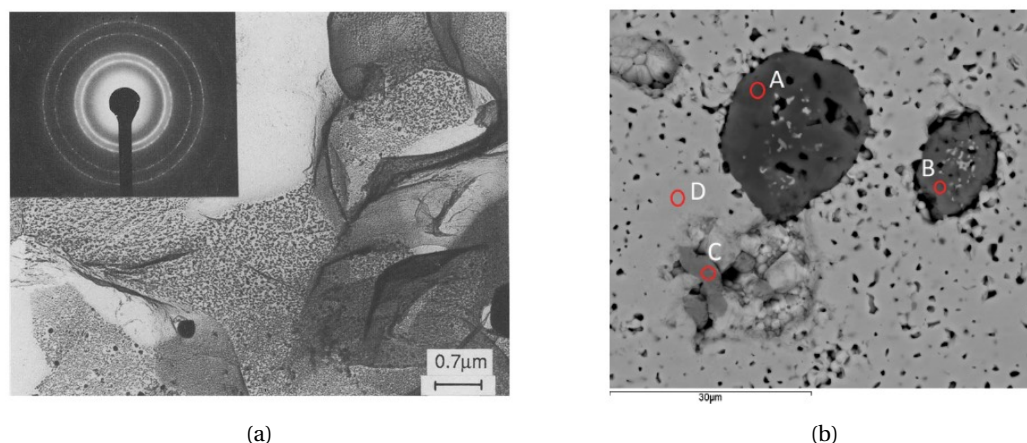


Figure 3: Studies on UO_2 pellet SIMFUEL experiments at (a): 6 at% (atomic percent) and (b): 43 GWd/tU burnup. (a): Lucuta et al. [84]: Grain boundary speckled with small perovskite crystallites (grey phase). SAED (selected-area electron diffraction) pattern shows crystal structure compatible with BaZrO_3 perovskite. (b): Hiezl et al. [55]: Area D shows the UO_2 matrix, area C a “white inclusion” metallic precipitate with Mo, Ru and Pd, area B and A are both grey phase oxide precipitates with significant amounts of BaZrO_3 and SrZrO_3 respectively.

The grey phase consists of elements that are accommodated on two cation sites (A and B) within a cubic perovskite lattice, mainly Ba^{2+} (on A) and Zr^{4+} ions (on B) forming BaZrO_3 . Sr^{2+} can substitute Ba^{2+} on the A-site to form $(\text{Ba}, \text{Sr})\text{ZrO}_3$ [23]. Other, less dominant, compounds in the grey phase are BaMoO_3 , BaUO_3 and Cs_2ZrO_3 [14, 68, 94, 108]. The incorporation of Mo_4^+ ions on the B-site increases with the oxygen potential of the fuel. This is caused by the oxidation of metallic molybdenum stored in so-called “white inclusions” in the nuclear fuel [15, 22, 68] (figure 3. Hietzl. et al. reported that the grey phase (in analysed SIMFUEL) consisted mainly of BaZrO_3 and that Sr and U concentrations were found to be less than 1% [55]. Sari et al. detected a grey phase in an irradiated UO_2 pellet with the composition $(\text{Ba}_{0.90}\text{Sr}_{0.05}\text{Cs}_{0.05})(\text{Zr}_{0.54}\text{Mo}_{0.14}\text{U}_{0.18}\text{Pu}_{0.14})\text{O}_3$. The phase was found at the columnar grain region of the pellet (a circular area at half the radius of the pellet, $r_0/2$) in the temperature range 1600 – 2000K [113]. Aging of the fuel changes the composition of the grey phase, as $^{90}\text{Sr}^{2+}$ decays to $^{90}\text{Zr}^{4+}$ and $^{137}\text{Cs}^+$ decays to $^{137}\text{Ba}^{2+}$. These changes in ionic charge result in further compositional alterations. Additionally, the formed Zr^{4+} is not accommodated on the A-site, which causes more instability in the perovskite phase and makes it susceptible to dissolution at higher burn-up rates [15]. With the passing of time and the increase of fuel burnup, higher oxygen potential causes further oxidation of compounds within the grey phase.

The study of the Ba-Sr-Cs-Mo-O system was broken up into the quaternary sub-system Ba-Cs-Mo-O and the ternary sub-systems Ba-Sr-O, Ba-Mo-O and Sr-Mo-O. A literature study in chapter 1 on Ba-Sr-O combines previously reported information on the system and shows the current phase diagrams of

the Ba-Mo-O, Sr-Mo-O and Ba-Cs-Mo-O systems that will be the basis of experimental measurements reported in chapter 3. These experimental studies allow for the further investigation or novel characterisation of the thermodynamic models using the CALPHAD method. This chapter also includes solution calorimetry measurement results on the successfully synthesised compound Ba_2MoO_5 . Knudsen effusion mass spectrometry (KEMS) measurement results on BaMoO_4 are depicted in chapter 4. Chapter 2 contains information on the theory behind all of the measurement techniques that are discussed in chapters 3 and 4. This thesis is a continuation of research done by Anna Smith [120, 121, 123], Nathan de Zoete [27], Maikel Rutten [111] and Lex Herrmann [53].

Chapter 1

Literature Review

This chapter is focused on providing an overview of previously published data on the Ba-Sr-O system, including thermodynamic and volatility studies as well as three reported pseudo-binary BaO – SrO phase diagrams. Published literature data on the Ba-Mo-O, Ba-Cs-Mo-O and Sr-Mo-O systems have already been compiled and reported on by Anna Smith [120, 123], Nathan de Zoete [27], Maikel Rutten [111] and Lex Herrmann [53], so this thesis will solely focus on experimental work for these three systems, specifically on the improvement of their phase diagrams. For this purpose, the current phase diagrams are shown in this chapter and these will be used as the basis for experimental measurements that are reported in chapter 3.

1.1 Ba-Sr-O system

The most important property of the Ba-Sr-O system is that barium and strontium are chemically alike and can dissolve in each other's oxide crystal lattices. BaO & SrO and BaO₂ & SrO₂ have the same crystal space group (Fm-3m (225) and I4/mmm (139) respectively) [37, 49, 76, 129] and Ba and Sr are found in the same group in the periodic table (alkaline-earth metals), so the miscibility is not surprising. The difference in Ba²⁺ and Sr²⁺ ionic radius however, induces some deviations from ideality in the miscibility of either ion in the oxide crystal structure of the other. This is reflected in the BaO – SrO phase diagrams documented by van der Kemp et al. [133, 134], Jacob et al. [59] and Gong et al. [47], which show a miscibility gap and no ternary compounds. Because of the mutual miscibility, here are no stoichiometric ternary compounds reported for this system [59, 110, 134], but studies did show the occurrence of nonstoichiometric compounds [16, 59, 93]. No ternary phase diagram has been found in the literature.

1.1.1 Phase diagram

Three sketches of a BaO-SrO pseudo-binary phase diagram were found in literature. They are shown in figure 1.1. Van der Kemp et al. [134] performed Knudsen effusion mass spectrometry measurements for 9 different compositions of (1-x)BaO + xSrO to analyse the intensity of ¹³⁸Ba²⁺ and ⁸⁸Sr²⁺ ions within a temperature range of 1430 – 1530K. The ratio between these two ions was used to determine the partial derivative of the molar excess Gibbs energy as a function of x, that was then calculated at T = 1490K (it is not specified why this specific temperature) and written in the form:

$$G_m^E [\text{kJ} \cdot \text{mol}^{-1}] = x(1 - x) \cdot 20.45 \quad (1.1)$$

Using equation 1.1 and the experimentally determined enthalpy of mixing by Flidlider et al. [40] (equation 1.2, found by means of solution calorimetry), the excess molar entropy was calculated (equation 1.3). It was assumed that the excess heat capacity could be neglected. Equations 1.2 and 1.3 were then used to make a pseudo-binary phase diagram of $(1-x)\text{SrO} + x\text{BaO}$. Ideal mixing was assumed for the liquid phase.

$$H_m^E [\text{kJ} \cdot \text{mol}^{-1}] = x(1-x) \cdot 37.12 \quad (1.2)$$

$$S_m^E [\text{J} \cdot \text{K}^{-1} \cdot \text{mol}^{-1}] = x(1-x) \cdot 11.19 \quad (1.3)$$

In a later paper by van der Kemp et al. [134], the previous phase diagram was revised. Thermodynamic functions of the binary alkaline earth oxide (BAEO) group were compared to analyse correlations between these oxide systems. During this investigation, the previously published phase diagram was slightly altered (it was found that the experimental enthalpy of mixing in equation 1.2 was too high) and the final diagram is presented in figure 1.1a.

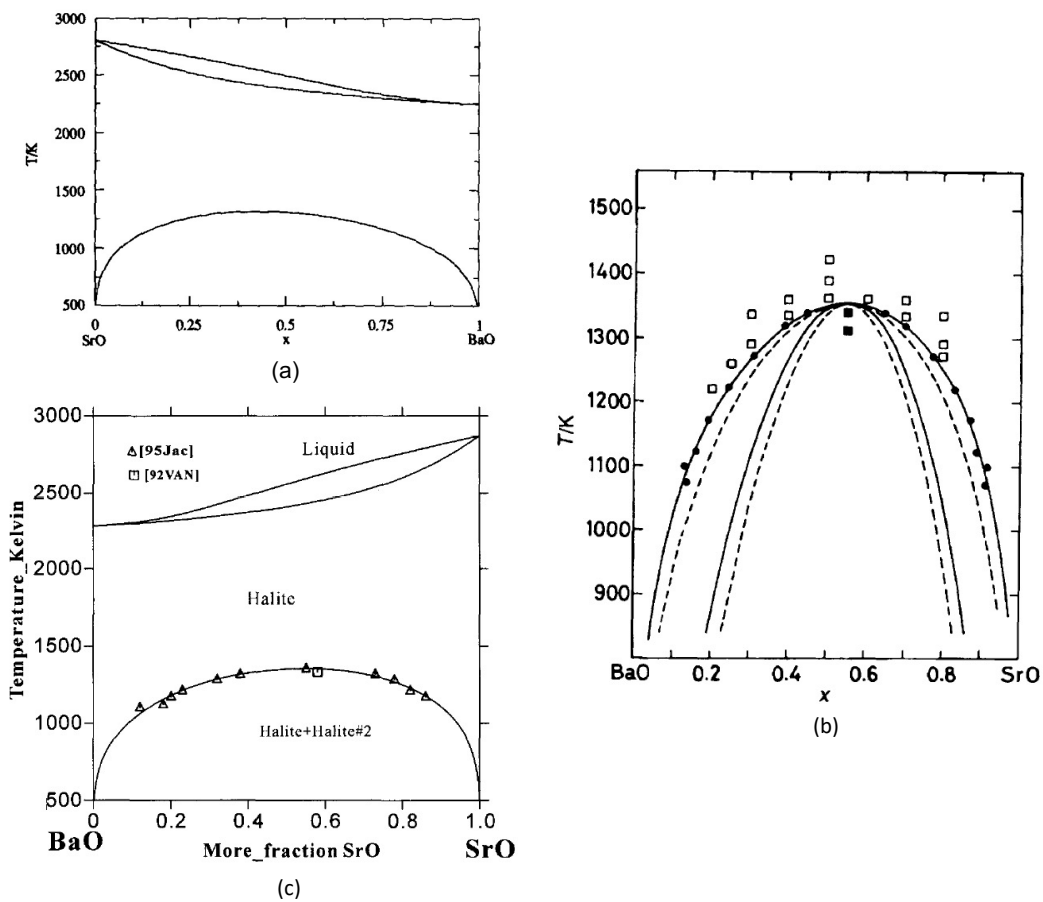


Figure 1.1: Published phase diagrams of the BaO - SrO system by (a) van der Kemp et al. [133, 134] (b) Jacob et al. [59] (c) and Gong et al. [47]

The phase diagram shows a miscibility gap in the solid region, meaning that below the lowest curve, a solid mixture exists between two phases. Above this curve, a homogeneous solid solution forms. The

highest point on the curve is called the critical point. Van der Kemp et al. [134] found the temperature at the critical point to be $1334 \pm 60\text{K}$. The transition from the homogeneous solid solution to homogeneous liquid were shown to mostly take place through incongruent melting (more so at low values of $x(\text{BaO})$) [133, 134].

After van der Kemp et al., Jacob et al. [59] published the phase diagram depicted in figure 1.1b, which also shows that the BaO-SrO system has a miscibility gap. This phase diagram shows two sets of lines, as opposed to the phase diagram in figure 1.1a. The upper set demonstrate the binodal curves (the same curve as in the van der Kemp et al. phase diagram), and the lower set represent the spinodal curves. Binodal curves denote the separation between the stable and the metastable region in a phase diagram. The metastable region describes the temperature and composition of a mixture where it fluctuates between stable (only consisting of one phase) and unstable (consisting of multiple phases). The line between the metastable and unstable regions is denoted by the spinodal curve (where $\delta^2 G / \delta x^2 = 0$) [9, 72]. The intercept between the binodal and spinodal curves is called the critical point, or in the phase diagram by van der Kemp et al., the highest point on the binodal curve.

Two models were used to calculate the binodal and spinodal curves in this phase diagram; the sub-regular model (assuming ideal mixing) [52] represented by dashed lines, and the pseudo-subregular model (including a G^{excess} term) represented by solid lines. The latter clearly has a better fit. The optimised G^{excess} term is given in equation 1.4. The temperature-dependent terms represent the enthalpy of mixing and the temperature-independent terms represent the excess entropy [59].

$$\Delta G^E [\text{J} \cdot \text{mol}^{-1}] = x(1-x) [(33390 - 7.09T)x + (29340 - 6.23T)(1-x)] \quad (1.4)$$

The calculated critical temperature by Jacob et al. was within the uncertainty margins of van der Kemp et al.: $1356 (\pm 4)\text{K}$ (compared to $1334 \pm 60\text{K}$ [134]). The critical composition above the binodal curve was found to be $x = 0.55 \pm 0.008$ (in $\text{Sr}_x\text{Ba}_{1-x}\text{O}$). This value is matched by W.G. Burgers [16], who found a critical composition of $x = 0.57$, but at a different temperature: around 1200K . Grebenyuk et al. [48] reported a homogeneous solid solution at 1373K over the entire composition range, but do not give the composition of this solution.

In the unstable region of the phase diagram, two phases were found to coexist by Jacob et al., with compositions $x = 0.38 \pm 0.06$ and $x = 0.73 \pm 0.05$. These values were determined by means of energy-dispersive analysis of X-rays (EDAX) and X-ray diffraction (XRD) measurements of annealed samples [59]. These findings differ from a study by Eisenstein et al. [39], which shows a solid solution between compositions $x = 0.05$ and $x = 0.25$ below an approximate temperature of 1083K . A homogeneous solution was reported at $1073 - 1123\text{K}$ (depending on the heating time and the crystal size). The composition was not specified.

Lastly, Gong et al. [47] used a substitutional solution model to combine the phase diagrams in figure 1.1a and b to give the phase diagram shown in figure 1.1c. Only the spinodal curves from Jacob et al. [59] were not included. It was found that both phase diagrams were in fair agreement with each other. The thermodynamic functions used by Gong et al. to model the phase diagram are reported in table 1.1. The BaO and SrO functions come from Lu et al. [83] and the SGTE database (1994) respectively and have been subsequently modified by Risold et al. [107]. Ideal mixing was assumed for the liquid phase, so no interaction parameters were used. These are the 0th and 1st order optimised interaction parameters for the solid halite phase [47]:

$$L^0(\text{Ba}^{2+}, \text{Sr}^{2+})(\text{O}^{2-}) = 31365 - 6.66T \quad (1.5)$$

$$L^1(\text{Ba}^{2+}, \text{Sr}^{2+})(\text{O}^{2-}) = -2025 + 0.43T \quad (1.6)$$

Table 1.1: Thermodynamic functions used by Gong et al. [47] to model the BaO - SrO phase diagram

| Phase | Function | Temperature range |
|--------|--|---|
| Liquid | ${}^{\circ}G_{\text{BaO}}^{\text{Liquid}} - H_{\text{Ba}}^{\text{SER}} - H_{\text{O}}^{\text{SER}}$ $= -504636.303 + 126373.536T^{-1} + 212.590092T - 45.367112T \ln T$ $-0.0088301228T + 9.53812533 \cdot 10^{-7} T^3$ $= -507499.47 + 390471.8T^{-1} + 251.681742T - 51.308392T \ln T$ $-0.003335694T^2 + 7.57304 \cdot 10^{-9} T^3$ $= -525650.131 + 373.045092T - 66.944T \ln T$ | $298.15 \leq T \leq 900$ $900 \leq T \leq 2286$ $2286 \leq T \leq 3000$ |
| | ${}^{\circ}G_{\text{SrO}}^{\text{Liquid}} - H_{\text{Sr}}^{\text{SER}} - H_{\text{O}}^{\text{SER}}$ $= G_{\text{SrO}}^{\text{Halite}} + 89410 - 31.1533101T$ | $298.15 \leq T \leq 5000$ |
| Halite | ${}^{\circ}G_{\text{BaO}}^{\text{Halite}} - H_{\text{Ba}}^{\text{SER}} - H_{\text{O}}^{\text{SER}}$ $= -563212.303 + 126373.536T^{-1} + 238.213889T - 45.367112T \ln T$ $-0.0088301228T^2 + 9.53812533 \cdot 10^{-7} T^3$ $= -566075.47 + 39047.8T^{-1} + 277.305539T - 51.308392T \ln T$ $-0.003335694T^2 + 7.57304 \cdot 10^{-9} T^3$ $= -584226.131 + 398.668889T - 66.944T \ln T$ | $298.15 \leq T \leq 900$ $298.15 \leq T \leq 900$ $2286 \leq T \leq 3000$ |
| | ${}^{\circ}G_{\text{SrO}}^{\text{Halite}} - H_{\text{Sr}}^{\text{SER}} - H_{\text{O}}^{\text{SER}}$ $= -607329.171 + 178730T^{-1} + 252.319465T - 44.96126T \ln T$ $-0.0082634T^2 + 8.58696333 \cdot 10^{-9} T^3$ $= -609963.764 + 426014.9T^{-1} + 287.955734T - 50.37118T \ln T$ $-0.003286532T^2 + 3.136675 \cdot 10^{-9} T^3$ | $298.15 \leq T \leq 900$ $900 \leq T \leq 2870$ |

1.1.2 Lattice parameters vs. composition

The three compositions found by Jacob et al. [59] that were described above ($x = 0.55 \pm 0.008$, $x = 0.38 \pm 0.06$ and $x = 0.73 \pm 0.05$) were analysed in the paper by means of XRD and EDAX for their lattice parameters and crystal structure. All compositions had the same cubic rock-salt crystal structure with identical space groups, only the lattice parameter changed as a function of composition. This linear relationship is given in figure 1.2.

W.G. Burgers [16] also reported the miscibility of Ba^{2+} and Sr^{2+} ions into the SrO and BaO lattices respectively. Heating three mixtures with different molar ratios of BaCO_3 and SrCO_3 (which also decarbonated these compounds) gave the lattice parameters of three mixed crystals: $\text{Ba}_{0.20}\text{Sr}_{0.80}\text{O}$, $\text{Ba}_{0.428}\text{Sr}_{0.572}\text{O}$ and $\text{Ba}_{0.692}\text{Sr}_{0.308}\text{O}$ (table 1.2). The linear correlation between the composition of the mixed crystals and their lattice parameter is also shown in figure 1.2. This line is slightly lower than that of Jacob et al., but both sets of data seem to match well. Burgers also found that SrO diffuses quicker into BaO than the other way around, probably because of the difference in radius between the Ba^{2+} and Sr^{2+} ions ($r(\text{Ba}^{2+}) = 0.136 \text{ nm}$ and $r(\text{Sr}^{2+}) = 0.116 \text{ nm}$ [16]).

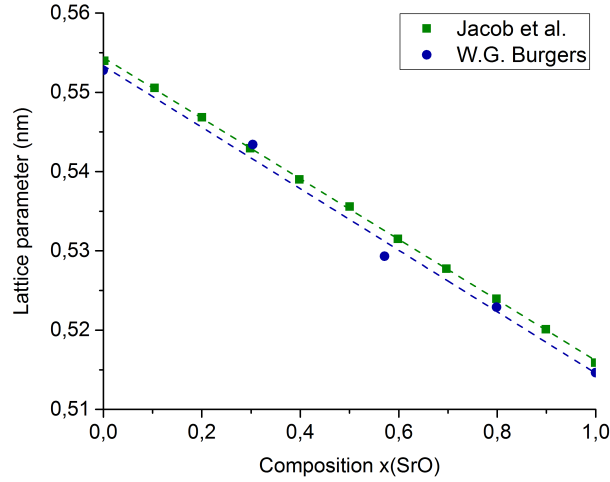


Figure 1.2: Correlation between the lattice parameter of the $\text{Sr}_x\text{Ba}_{1-x}\text{O}$ unit cell and its composition. Samples were heated up to $\pm 1400\text{K}$ by Burgers [16], the heating temperature was not specified by Jacob et al. [59].

1.1.3 Volatility studies

As mentioned above, van der Kemp et al. [134] performed Knudsen effusion mass spectrometry (KEMS) measurements on 9 different compositions within the $(1-x)\text{BaO} + x\text{SrO}$ system. Figure 1.3 shows the relative intensities of $\log(^{88}\text{Sr}^{2+} / ^{138}\text{Ba}^{2+})$ vs. $1/T$ for the 9 different mole fractions x . It is clear from the figure that the relative intensity of $^{88}\text{Sr}^{2+}$ ions increases more quickly than the intensity of $^{138}\text{Ba}^{2+}$ ions and that hence the Sr ions are more volatile as temperature increases. The figure also shows that the individual intensity of $^{88}\text{Sr}^{2+}$ ions was higher than that of the $^{138}\text{Ba}^{2+}$ ions (where $\log(^{88}\text{Sr}^{2+} / ^{138}\text{Ba}^{2+}) = 0$, their ratio equals 1), for all compositions except for one with $x = 0.352$ [134]. This is strange, considering the higher volatility of Ba (as was discussed in the introduction of this thesis), but could maybe be explained by the smaller ionic radius of Sr^{2+} compared to Ba^{2+} .

The study by Burgers [16] disputes the finding by van der Kemp et al. [134], claiming that while the amount of evaporating BaO diminishes at increasing temperature, it evaporates more rapidly than SrO, leaving a higher percentage of SrO in the surface layer of the sample. This study was done by means of XRD analysis [16]. H. Gaertner [42] studied layers of $(\text{Ba},\text{Sr})\text{O}$ by means of electron diffraction (which only causes scattering by the top atomic layers in contrast to XRD) and found that the top ± 20 surface layers only contained about 10 percent BaO and 90 percent SrO, therefore confirming Burgers' findings (whether this is wt% or mol% is not said). This phenomenon was explained by the higher volatility of BaO compared to SrO, which caused BaO to evaporate faster than it could be replaced by diffusion from the interior of the sample. This conclusion was backed by the determined cubic lattice parameter of the surface layers (5.12\AA), which was compatible with the lattice parameter of SrO (5.15\AA [49]) and not that of BaO (5.54\AA [59]). Also, BaO has a higher scattering intensity under electron diffraction than SrO, due to its higher atomic number. Since no BaO scattering was detected, despite its higher scattering intensity, it was a further confirmation of the low amount of BaO in the surface layers [42].

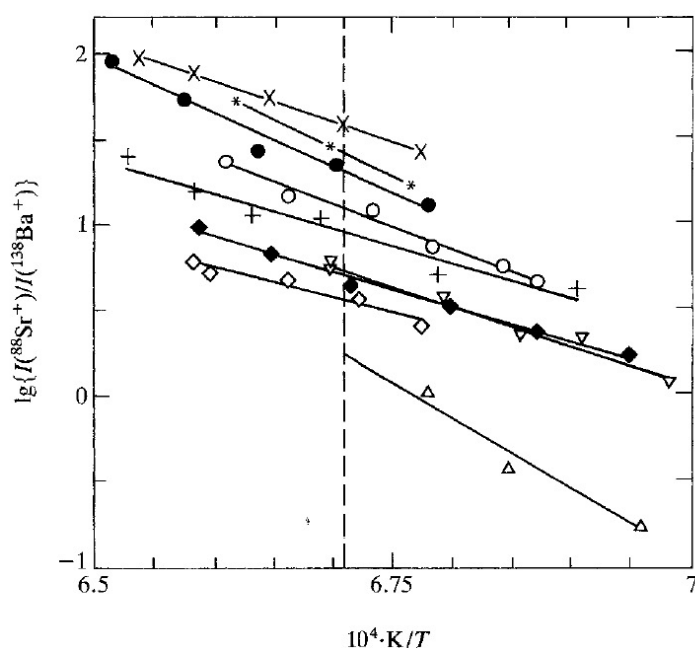


Figure 1.3: Plot of $\log(I(^{88}\text{Sr}^{2+}) / I(^{138}\text{Ba}^{2+}))$ against $1/T$ for the mole fractions x . $+ x = 0.101$; $\nabla x = 0.200$, $\blacklozenge x = 0.352$; $\Delta x = 0.351$; $\circ x = 0.470$; $\bullet x = 0.568$; $\times x = 0.675$; $* x = 0.795$; $\diamond x = 0.872$ [134]

Results by Claassen et al. [20] also show that BaO evaporates more quickly than SrO at the same temperature. When a mixed sample of (Ba,Sr)O was heated, the amount of SrO that evaporated was too low to be detected and the amount of BaO that evaporated decreased over time. This was also considered to be due to the increased amount of SrO in the surface layers over time and the low diffusion rate of BaO in the crystal lattice [20].

Using the data by Burgers (which penetrates deeper into the sample due to the use of XRD), Gaertner calculated that SrO was predominant in the top 10 000 atomic layers [42]. Benjamin et al. [11] show that prolonged heating (for several hundred hours at 1100K) of a (Ba,Sr)O sample resulted in a predominance of SrO throughout the whole thickness of the sample (average 5wt% BaO and 95wt% SrO over 8 measurements), with an average weight loss of 41.2% (all assumed to be due to BaO). The starting composition of the sample was found not to make a difference in terms of the final composition. Just like Burgers, Benjamin et al. reported the decreased emission of BaO over time in a (Ba,Sr)O sample, due to the increasing amount of SrO in the surface layer (figure 1.4) [11].

It must be mentioned that the papers by Burgers, Gaertner, Claassen et al. and Benjamin et al. were published in 1932, 1935, 1932 and 1933 respectively, compared to the paper by van der Kemp et al. in 1992. However, considering the higher volatility of BaO, the compatible lattice parameter of the surface layers to SrO and the similar conclusions by all of these studies, the findings by the first four papers cannot simply be dismissed due to their age. More volatility studies of the (Ba,Sr)O system are needed to confirm the results by these studies and to give new data on the intensities of Ba^{2+} and Sr^{2+} ions after a KEMS measurement.

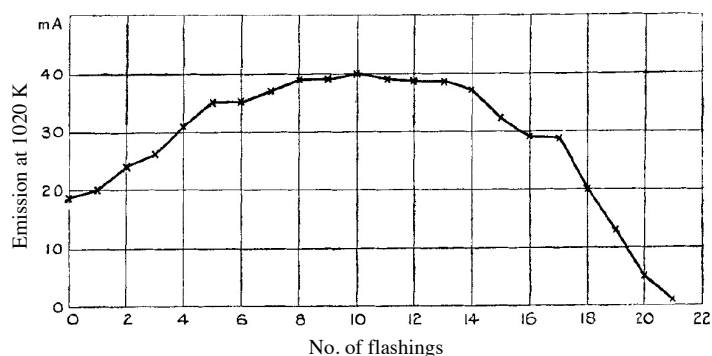


Figure 1.4: The emission of BaO from a (Ba,Sr)O sample at 1020K [11]

1.1.4 Ba-O, Sr-O and Ba-Sr systems

The Ba-O and Sr-O systems each contain two stable binary compounds: the monoxides BaO and SrO and peroxides BaO₂ and SrO₂ respectively. The Ba – Sr system does not form any binary compounds, due to the miscibility of Ba and Sr. Limited research has been done into establishing phase diagrams of these systems, but since they are not the focus of this thesis, these findings will not be discussed here. The reader is referred to studies by Zimmermann et al. [142], Kedrovskii et al. [66], Jorda et al. [62], Zhou et al. [141] and Smith et al. [120] for binary phase diagrams of the Ba-O system, to a study by Risold et al. [107] for a binary phase diagram of the Sr-O system and to an yet unpublished TAF-ID model of the binary phase diagrams of the Ba-O, Sr-O and Ba-Sr systems by A.L. Smith.

The only research that will be discussed on the Ba-O and Sr-O systems, is the nonstoichiometry of the peroxide compounds BaO₂ and SrO₂, because it ties in with the lattice parameter vs. composition discussion depicted in figure 1.2. A study by Königstein [76] investigated the nonstoichiometry of BaO₂ and SrO₂ by mixing BaO and SrO with BaO₂ and SrO₂ respectively, in a range of different ratios, and heating them for 30 min at 10kbar and at 1400-1800°C. The resulting compounds were analysed via powder and single crystal X-ray diffraction. It was found that both barium and strontium peroxide form nonstoichiometric compounds, but only in the ranges of $1.72 \leq (2-x) \leq 1.97$ for BaO_{2-x} and $1.90 \leq (2-x) \leq 1.98$ for SrO_{2-x}. These compounds form

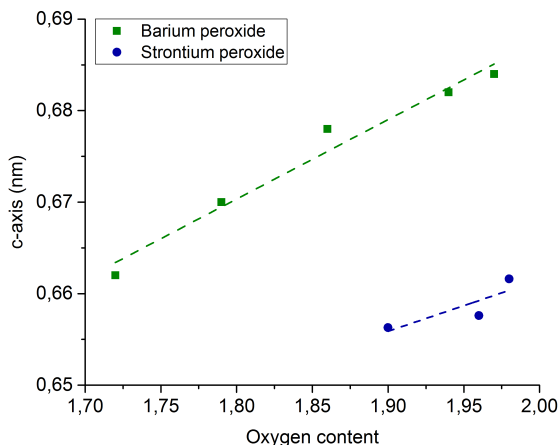


Figure 1.5: Correlation between the c-axis length and the composition of barium and strontium peroxide [76]

when the lattice site with peroxide ions (O₂²⁻) (position 4e in the space group) is not fully occupied and oxide ions (O²⁻) are present on the 2b position. The extent to which peroxide ions are replaced by oxide ions determines the length of the c-axis of the crystal lattice structure.

The larger the nonstoichiometry of the compound, the shorter the c-axis becomes. This is due to the shortening of the peroxide bond length ($O^- - O^-$), which is aligned with the c-axis. The length of the a-axis remains almost constant. The linear relation between the c-axis length and the peroxide composition is shown in figure 1.5 for both BaO_{2-x} and SrO_{2-x} [76]. A study by Range et al. [104] also reports on the nonstoichiometry of the strontium peroxide compound and expects that some level of lattice defect will always be present. Therefore, the lattice parameters of stoichiometric SrO_2 cannot be determined empirically and have to be based on the extrapolation of the linear correlation between the lattice parameter and the peroxide composition [104].

1.1.5 Structural data of the compounds

The structural data of all reported compounds of the Ba-Sr-O, Ba-O and Sr-O systems are shown in table 1.2.

Table 1.2: Structural information of compounds in the Ba-Sr-O system

| Compound | Space group | Structural parameters | Analysis method | Reference |
|-------------------------|--------------|--|-----------------------|-----------|
| BaO_2 | I4/mmm (139) | $a = 0.38118(2)$, $b = 0.38118(2)$, $c = 0.68476(6)$ nm, $\alpha, \beta, \gamma = 90^\circ$ | XRD | [37] |
| $BaO_{1.97}$ | I4/mmm (139) | $a = 0.38059(2)$, $b = 0.38059(2)$, $c = 0.6837(2)$ nm, $\alpha, \beta, \gamma = 90^\circ$ | XRD | [76] |
| $BaO_{1.94}$ | I4/mmm (139) | $a = 0.38071(3)$, $b = 0.38071(3)$, $c = 0.6816(1)$ nm | XRD | [76] |
| $BaO_{1.86}$ | I4/mmm (139) | $a = 0.38096(2)$, $b = 0.38096(2)$, $c = 0.6780(1)$ nm | XRD | [76] |
| $BaO_{1.72}$ | I4/mmm (139) | $a = 0.38076(3)$, $b = 0.38076(3)$, $c = 0.6621(2)$ nm, $\alpha, \beta, \gamma = 90^\circ$ | XRD | [76] |
| $BaO_{1.79}$ | I4/mmm (139) | $a = 0.38085(5)$, $b = 0.38085(5)$, $c = 0.66986(6)$ nm, $\alpha, \beta, \gamma = 90^\circ$ | XRD | [76] |
| $Ba_{0.20}Sr_{0.80}O$ | Fm-3m (225) | $a = 0.5225$, $b = 0.5225$, $c = 0.5225$ nm, $\alpha, \beta, \gamma = 90^\circ$ | Debye-Scherrer camera | [16] |
| $Ba_{0.428}Sr_{0.57}O$ | Fm-3m (225) | $a = 0.529$, $b = 0.529$, $c = 0.529$ nm, $\alpha, \beta, \gamma = 90^\circ$ | Debye-Scherrer camera | [16] |
| $Ba_{0.692}Sr_{0.308}O$ | Fm-3m (225) | $a = 0.543$, $b = 0.543$, $c = 0.543$ nm, $\alpha, \beta, \gamma = 90^\circ$ | Debye-Scherrer camera | [16] |
| BaO | Fm-3m (225) | $a = 0.554$, $b = 0.554$, $c = 0.554$ nm, $\alpha, \beta, \gamma = 90^\circ$ | XRD | [59] |
| $Ba_{0.5}Sr_{0.5}O$ | Fm-3m (225) | $a = 0.536$, $b = 0.536$, $c = 0.536$ nm, $\alpha, \beta, \gamma = 90^\circ$ | XRD | [59] |
| $Ba_{0.504}Sr_{0.496}O$ | Fm-3m (225) | $a = 0.5332$, $b = 0.5332$, $c = 0.5332$ nm, $\alpha, \beta, \gamma = 90^\circ$ | Unknown | [93] |
| $SrO_{0.95(2)}$ | I4/mmm (139) | $a = 0.35626(3)$, $b = 0.35626(3)$, $c = 0.66159(6)$ nm, $\alpha, \beta, \gamma = 90^\circ$ | Single-crystal XRD | [104] |
| SrO | Fm-3m (225) | $a = 0.51484(2)$, $b = 0.51484(2)$, $c = 0.51484(2)$ nm, $\alpha, \beta, \gamma = 90^\circ$ | XRD | [49] |
| $SrO_{1.90}$ | I4/mmm (139) | $a = 0.35585(4)$, $b = 0.35585(4)$, $c = 0.6563(1)$ nm, $\alpha, \beta, \gamma = 90^\circ$ | XRD | [76] |
| $SrO_{1.96}$ | I4/mmm (139) | $a = 0.35619(3)$, $b = 0.35619(3)$, $c = 0.6576(1)$ nm, $\alpha, \beta, \gamma = 90^\circ$ | XRD | [76] |
| $SrO_{1.98}$ | I4/mmm (139) | $a = 0.35630(2)$, $b = 0.35630(2)$, $c = 0.6616(1)$ nm, $\alpha, \beta, \gamma = 90^\circ$ | XRD | [76] |

1.2 Ba-Mo-O system

The Ba-Mo-O system has been thoroughly investigated and described by A.L. Smith et al., in their 2021 paper [120]. Previous work on this system was done by Nathan de Zoete [27], Maikel Rutten [111] and Lex Herrmann [53]. Figure 1.6 shows the latest pseudo-binary BaO – MoO₃ phase diagram that was presented by Smith et al., which will be used as the basis for experimental measurements in this thesis.

1.3 Ba-Cs-Mo-O system

The quaternary compound BaCs₂(MoO₄)₂ was successfully synthesised by Nathan de Zoete [27] and subsequently characterised by Maikel Rutten [111] and by Smith et al. [123]. After this, Maikel Rutten made a preliminary study into the pseudo-binary BaMoO₄ – Cs₂MoO₄ phase diagram, but did not model it yet using the CALPHAD method. This phase diagram is shown in figure 1.7 and will be used as the basis for further experimental measurements.

1.4 Sr-Mo-O system

Literature data published on the Sr-Mo-O system has previously been combined and analysed by Maikel Rutten [111]. A model of the pseudo-binary SrO – MoO₃ phase diagram was first published by Zhukovskii et al. [137] and was subsequently modelled by A.L. Smith using the CALPHAD method (as yet unpublished). This model is shown below in figure 1.8 and will be used as a basis for further experimental measurements.

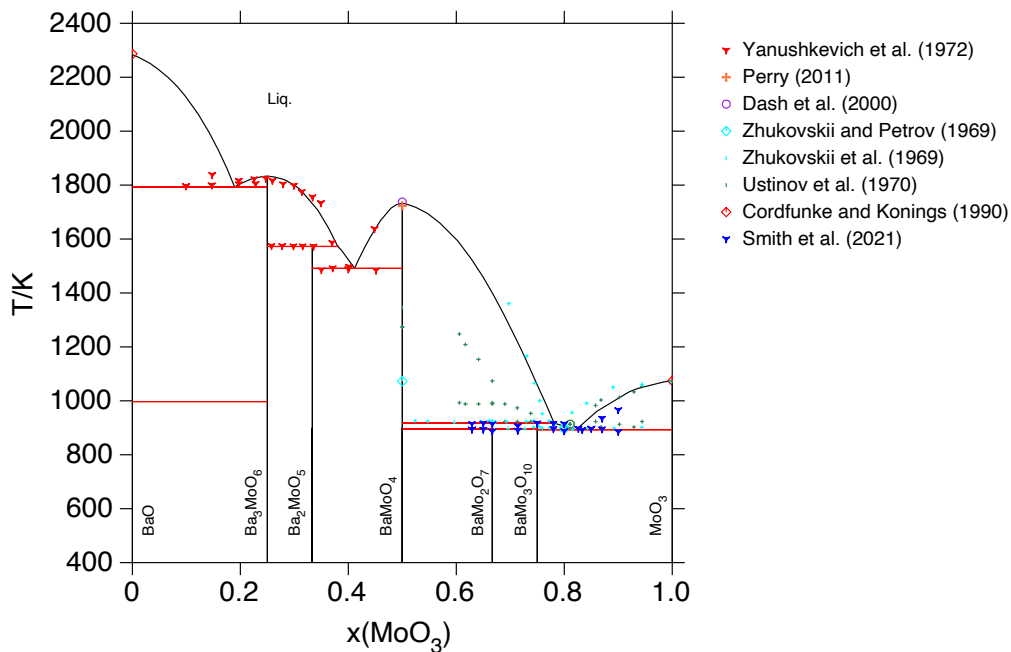


Figure 1.6: Pseudo-binary BaO - MoO₃ phase diagram published by Smith et al. [120]. Data points by Yankuskevich et al. [130], Perry [98], Dash et al. [96], Zhukovskii et al. [137], Ustinov et al. [89], Cordfunke and Konings [38] and Smith et al. [120]

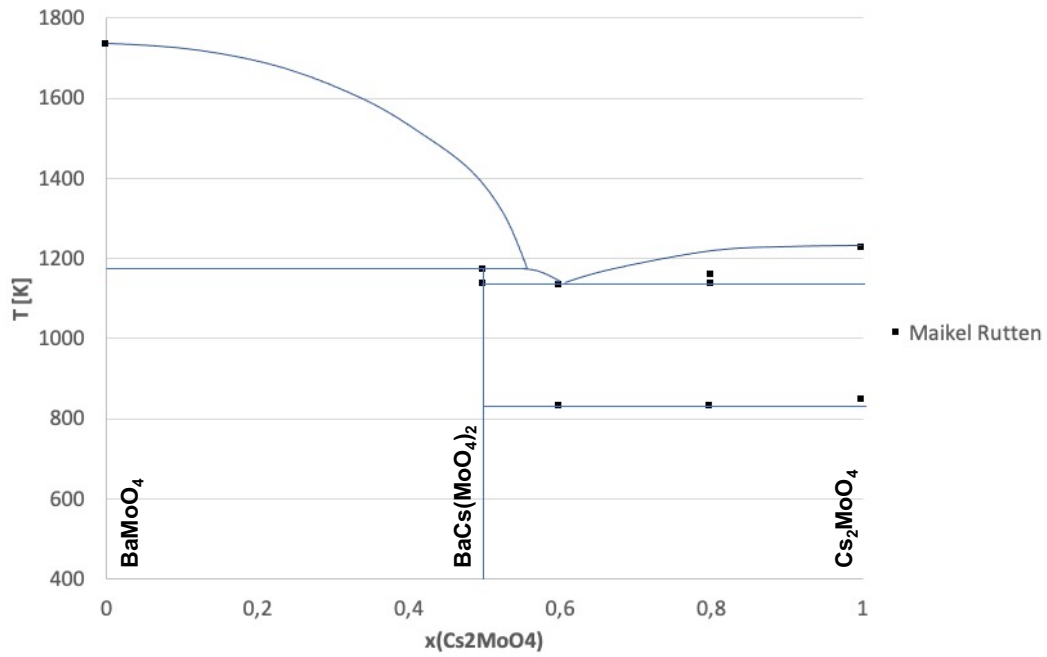


Figure 1.7: Original excel model of the $(1-x)\text{BaMoO}_4 - (x)\text{Cs}_2\text{MoO}_4$ phase diagram [111]

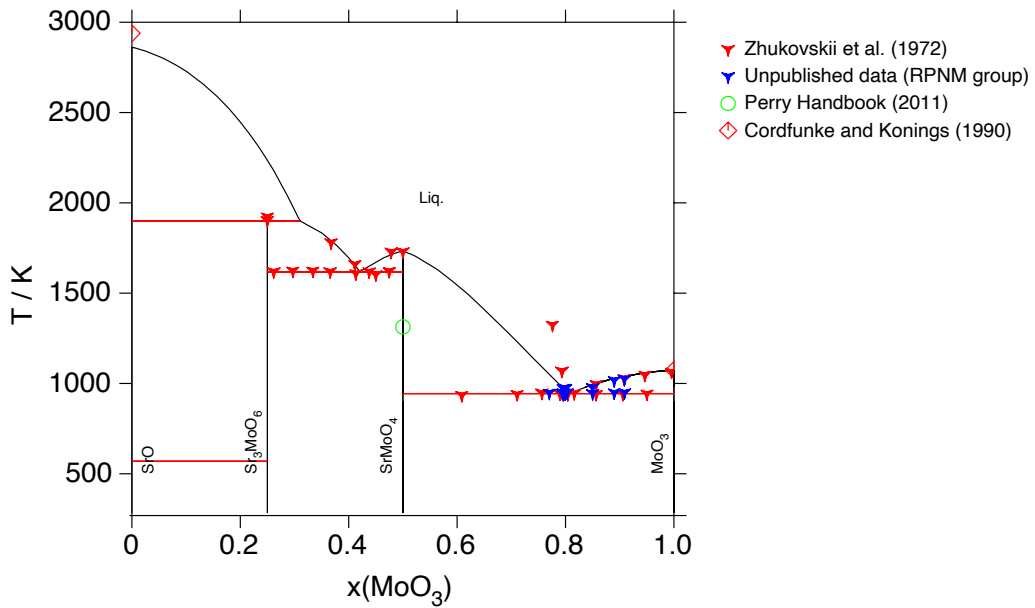


Figure 1.8: Current pseudo-binary SrO - MoO_3 phase diagram. Data points by Zhukovski et al. [130], the Perry handbook [98], Cordfunke and Konings [38] and unpublished data by the RPNM research group.

Chapter 2

Theoretical Background

Many steps go into the making of a phase diagram. First, the synthesis of relevant compounds (solid state synthesis (2.1)) that are tested for their purity by Rietveld refinement (2.2.4.2) of their X-ray diffraction (XRD (2.2)) pattern, or analysed graphically using the PowderCell software (2.2.4.1)). Then these compounds are used for Thermogravimetric Differential Scanning Calorimetry (TGDCS (2.3)) measurements to determine the phase transition temperatures that are needed to model a phase diagram by means of the Calculation of Phase Diagram (CALPHAD) method (2.6). Thermodynamic properties of individual compounds may further be investigated by means of Solution Calorimetry (2.4) and Knudsen Effusion Mass Spectrometry (KEMS (2.5)), to improve the accuracy of the thermodynamic model. This chapter discusses the theoretical background of these techniques.

2.1 Solid state synthesis

The only synthesis technique that was used to make compounds in this thesis is the solid-state synthesis technique, also called the ceramic method. As the name predicts, solid-state reagents are reacted to form a solid-state product. The reagents are mixed together with a mortar and pestle to ensure a homogeneous mixture (or with a ball-mill for an industrial scale production) and are heated at high temperatures for relatively long reaction times (12h or even days). These long reaction times are necessary because the diffusion rate during these syntheses is limited. Purification steps after the synthesis are very difficult, therefore it is important to prepare a homogeneous mixture from the beginning to favour a complete reaction.

The synthesis temperature is determined based on the melting and boiling points of the reactants, depending whether the intention is for the reactants to melt or to stay solid. Melting the reactant mixture speeds up the reaction process, because it increases the diffusion rate. However, if reactants are volatile, it is better to stay under the melting point to avoid evaporation and mass loss. Because of this reason, syntheses in this thesis are all performed at a temperature under the melting point of the reactant mixture. Syntheses are performed under ambient atmosphere or under O₂ flow to promote oxidation/ to avoid reduction of the prepared sample to lower valence states [6].

2.2 X-ray Diffraction (XRD)

X-ray diffraction (XRD) combined with the Rietveld refinement technique or PowderCell software analysis was used to determine the purity of the compounds that were made during this thesis. XRD produces a unique “fingerprint” pattern of a pure crystal structure, with information on atomic positions, lattice parameters and the space group of a compound. This chapter will briefly explain the theory behind this measurement technique and the XRD pattern analysis programmes FullProf and PowderCell.

2.2.1 Theory: Bragg’s Law and atomic planes

Crystal compounds are made up of series of stacked identical unit cells that all have the same proportions and atomic positions. These unit cells are selected so that they can be used to form the entire crystal structure using only translational displacements. The shape and size of the unit cell depend on the space group of the crystal structure and are denoted by the lattice parameters a , b and c (lengths of the sides) and α , β and γ (angles between the sides).

A plane going through a unit cell can be defined by the Miller indices (hkl) , where h , k and l are the reciprocals of the intersections that the plane has with the unit cell axes (or sides). Figure 2.1 shows three examples of a plane going through a unit cell with its corresponding Miller index [8].

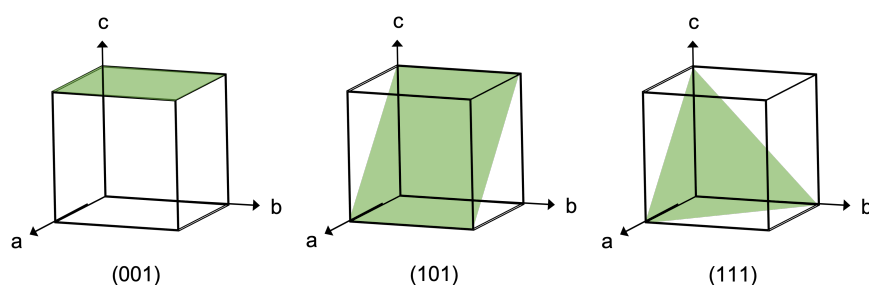


Figure 2.1: Visual representation of three examples of atomic planes and their respective Miller indices

X-rays have a wavelength that is compatible with the unit cell parameters of crystalline materials. This condition allows for X-ray beams to scatter in a mirror-like reflection off the atoms in a crystal structure (or rather, the electron clouds cause elastic scattering of the X-ray beams). The scattered waves interfere constructively and destructively with each other to give a specific wave pattern that depends on the distance between the lattice planes (d) of a crystal structure [8]. This pattern made by the constructive scattering waves is represented by Bragg’s Law:

$$n\lambda = 2d \sin \theta \quad (2.1)$$

where ‘ d ’ is the distance between two lattice planes, ‘ n ’ is a positive integer, ‘ λ ’ is the wavelength and θ is the diffraction angle. Figure 2.2 gives a visual representation of two incoming waves that scatter on an atomic plane and diffract with angle θ . Bragg’s law is determined as follows. The lower wave travels further than the upper wave by a distance of $xy + yz$. If a signal is to reach the detector so that a peak may be recorded, the waves need to be in phase and interfere constructively. In order for this to occur, the longer distance travelled by the lower wave must be equal to its wavelength times some integer ($n\lambda$). The two triangles on the right show that: $xy = d \sin \theta$ and $yz = d \sin \theta$, which gives $xy + yz = 2d \sin \theta$. Therefore $n\lambda = 2d \sin \theta$ [8].

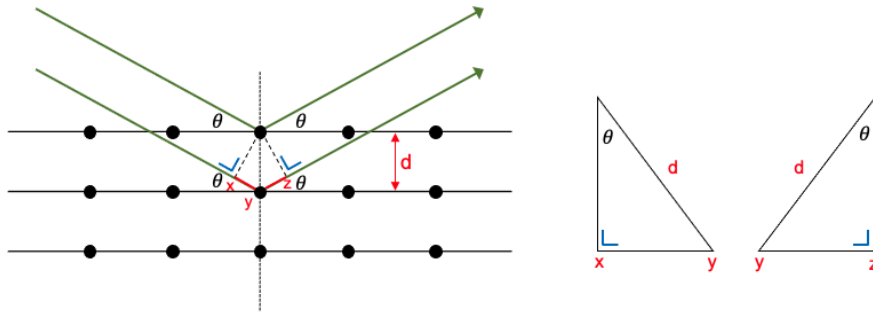


Figure 2.2: Visual representation of two incoming X-rays on an atomic plane with diffraction angle θ

Each atomic plane with individual distance 'd' has a specific diffraction angle θ at which waves interfere constructively to give a signal to the detector. The smaller the distance 'd', the larger the diffraction angle at which the peak will occur. Each peak on the XRD pattern can therefore be ascribed to a specific plane in the crystal structure of the sample. The location of the peak also depends on the size of the atoms in the crystal structure. The larger the atoms, the larger the displacement between the atomic planes and hence the smaller the diffraction angle θ must be. The intensity of the peaks depends on the electron density of the atoms, the diffraction angle and the position of the atoms in the unit cell. The larger the electron density and the lower the diffraction angle, the more the X-rays are scattered from one atom in the unit cell. This is why the higher intensity peaks are usually seen at lower diffraction angles on an XRD pattern [135, 136].

2.2.2 Powder X-ray Diffraction

It is possible to study both single crystals and powders by using X-ray diffraction. When X-rays diffract off a single crystal, it results in a reciprocal pattern that is characteristic of its crystal structure. This method is not used for the purposes of this thesis however, because the samples that were measured consisted of powders containing many small crystals with random orientations. These random orientations present in a ring-like pattern, called Debye-Scherrer rings. Figure 2.3 shows the reciprocal patterns of a single crystal lattice on the left and Debye-Scherrer rings on the right. Each ring represents one atomic plane and results in one peak [143].

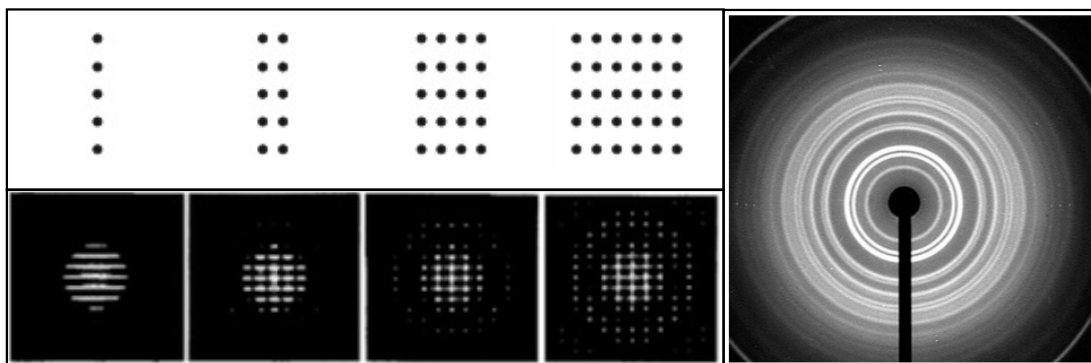


Figure 2.3: Reciprocal patterns of pure crystals on the left and Debye-Scherrer rings on the right (figure adapted from [143])

During a powder XRD measurement, an X-ray source is rotated in an arc around the fixed sample, in conjunction with a detector on the opposite side (figure 2.4). The X-ray source consists of an X-ray tube that converts an electrical input into X-ray beams. In it, electrons emitted by a metal cathode collide with a metal anode (usually tungsten, molybdenum or copper) to produce X-rays by means of bremsstrahlung [122]. Bremsstrahlung is the emission of radiation when an incoming electron is slowed down by its attraction to the positive nucleus of an atom. Its loss of energy in slowing down is compensated by the emission of an X-ray, complying with the law of conservation of energy. The metal used for the anode affects the wavelength of the produced X-rays. A monochromator is attached to the X-ray tube to select X-rays with the desired wavelength. The detector is a scintillation detector, it uses a photomultiplier to enlarge the number of electrons that are released by the diffracted x-ray photons, in order to heighten the signal to be detected [4, 25, 74]. This signal is sent to the computer and recorded as an XRD pattern of intensity vs. 2θ . The result is an XRD pattern as shown in figure 2.5.

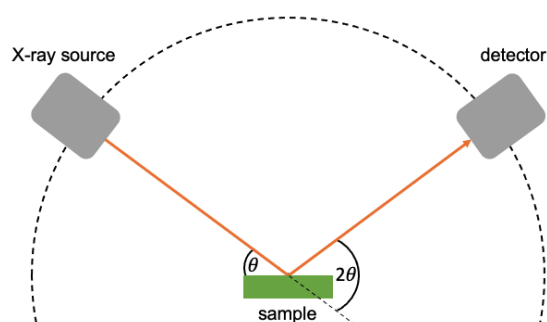


Figure 2.4: Visual representation of an X-ray source and detector rotating around a sample in an XRD

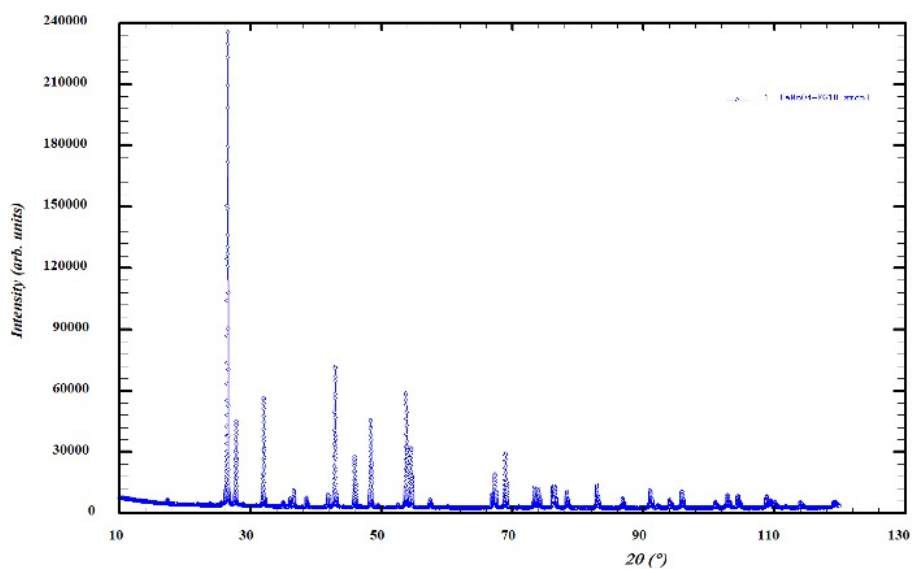


Figure 2.5: XRD pattern of BaMoO_4 . Intensity in arbitrary units vs. 2θ (°)

2.2.3 Method

XRD measurements were all performed using a Philips PANalytical X'Pert PRO X-ray diffractometer (figure 2.6) using a Cu-anode (45kV, 40mA) with a real time multi strip (RTMS) detector. Measurements were done from $10^\circ \leq 2\theta \leq 120^\circ$ at a step size of 0.00837° for 8h. Most samples were hygroscopic and thus assembled in the argon atmosphere of the glovebox in an air-tight sample holder. The samples that were stable in an ambient atmosphere were prepared outside the glovebox on a silicon wafer.



Figure 2.6: Philips PANalytical X'Pert PRO X-ray diffractometer [111]

2.2.4 Analysis

The analysis of XRD patterns was done either by means of PowderCell analysis or a Rietveld refinement or for phase identification. The sections below will elaborate on both techniques and will show under which circumstances they were used.

2.2.4.1 PowderCell analysis

PowderCell is a software programme that compares the experimental XRD pattern of a sample to theoretical patterns of selected phases in order to identify all the peaks in the original pattern. There are many software programmes that can do this, but PowderCell was used for this thesis. First a number of compound patterns are manually selected to be shown, after which the experimental pattern is placed above them, so that their peaks may be compared. It requires an idea as to which compounds might be present in a sample, because the software offers no suggestions. Once all the phases in the sample have been identified, a Rietveld refinement can be performed. PowderCell analysis can also be used after a Rietveld refinement, in order to match theoretical patterns to unidentified peaks. An example of a PowderCell analysis is shown in figure 2.7 from 23 to 42 degrees.

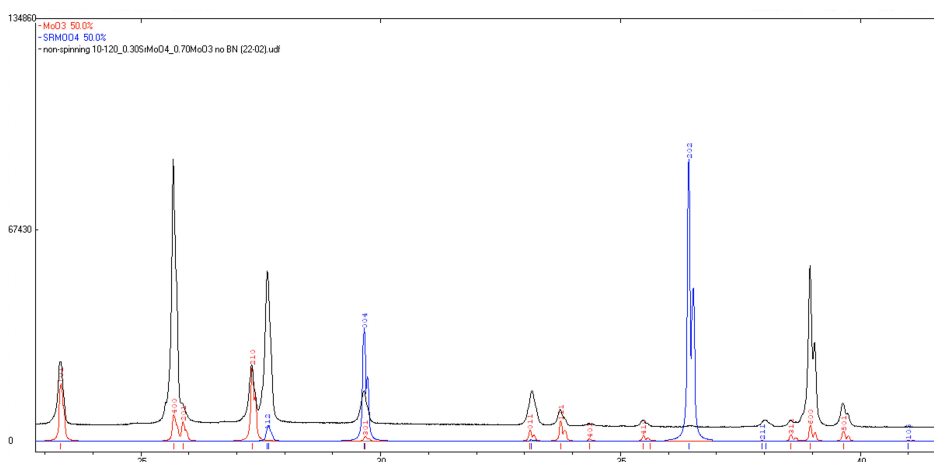


Figure 2.7: Example of a powdercell analysis between 23 and 42 degrees (intensity on the y-axis and 2θ on the x-axis). The blue and the red are calculated patterns of SrMoO_4 and MoO_3 , respectively, and black is the experimental XRD pattern.

2.2.4.2 Rietveld refinement

Rietveld refinement is an analytical method that was used to determine whether or not a tested sample was pure. It minimises the fit between a measured XRD pattern of a compound to a calculated XRD pattern of that compound and records the difference. This analysis reveals any additional peaks present in the measured pattern that are not in the calculated pattern of the pure compound. If the compound is pure, the Rietveld refinement can determine atomic positions and lattice parameters of the crystal structure. It can also be used to find mass ratios between multiple phases in a sample. The software programme FullProf was used to perform this analysis technique.

Firstly, the programme requires structural data of the compound that is to be analysed, such as its space group, lattice parameters and atomic positions. It gradually refines these and many other parameters that influence the position and the shape of the peaks in the XRD pattern. Which parameters are refined is determined manually and the number of refined parameters is increased as the refinement goes on, gradually improving the fit to the experimental pattern. The accuracy of the fit is determined by the least-square minimisation [109]:

$$\chi^2 = \frac{\sum_i w_i |Y_{obs}^i - Y_{calc}^i|^2}{N - P} \quad \text{where} \quad w_i = \frac{1}{\sigma(T_{obs}^i)} \quad (2.2)$$

where w_i is the weighting factor, Y_{obs}^i the observed counts, Y_{calc}^i the calculated counts, P the number of refined parameters, $\sigma(T_{obs}^i)$ the standard deviation of T_{obs}^i values and \sum_i the summation over the N points of the fitted region [109]. The purity of a sample is indicated by the χ^2 value (only for 1-phase refinements), the better the fit, the lower its value. If there are no noticeable additional peaks, the sample is considered pure at χ^2 values lower than approximately 15. The Rietveld refinement of the previously shown XRD pattern (figure 2.5) is depicted in figure 2.8. The red line shows the experimental pattern (Y_{obs}^i) and the black line the fitted pattern (Y_{calc}^i). The blue line shows the difference between the red and the black lines ($Y_{obs}^i - Y_{calc}^i$), it is clear that no missing peaks are present. The green lines depict the Bragg positions of the peaks that can be traced back to individual atomic planes as was discussed above.

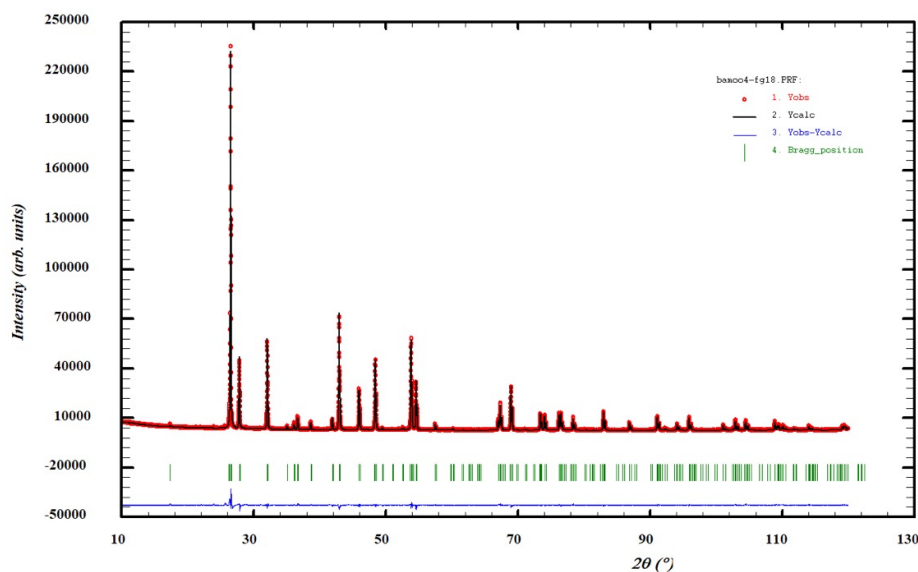


Figure 2.8: Rietveld refinement of previously shown XRD pattern in figure 2.5 with $\chi^2 = 6.67$

2.3 Thermogravimetric differential scanning calorimetry (TGDCS)

Thermogravimetric differential scanning calorimetry (TGDCS) was used to determine phase transition temperatures of the various systems that were investigated in this thesis. The resulting data points were then used as the experimental basis for subsequent CALPHAD modelling.

2.3.1 Theory

Differential scanning calorimetry (DSC) is a measurement technique used to detect thermal fluctuations in a material associated with the phase changes or chemical reactions that occur when the material is heated or cooled in a controlled manner. Phase changes, such as evaporation, melting, polymorphic phase transitions, etc., cause a change in enthalpy in the material and are detected as endothermic or exothermic events [17]. These events are recorded by measuring the difference in heat flow between a sample and a reference crucible.

TGDCS is based on this principle and can, in addition to DSC, precisely balance both the sample and the reference crucible from a weighing scale, so that any change in mass of the sample crucible is detected and recorded. This additional information can lead to a more definitive diagnosis as to which type of phase transition or change in composition has occurred. For example, a reduction in mass could mean the evaporation of some of the sample and an increase in mass could point to oxidation. Also, some phase transitions are not associated with a mass change, such as congruent melting or crystallisation.

TGDCS measurements were done using the Setaram Multi HTC module on a 96 Line calorimeter (figure 2.9a). Figure 2.9b shows the reference crucible (on the left) and sample crucible (on the right) suspended on a wire that is connected to a scale that is situated above. Both crucibles are identical. The reference crucible is not necessarily empty, and can be filled with a substance that has well-documented phase transitions.



Figure 2.9: (a) Picture of the thermogravimetric differential scanning calorimeter that was used for measurements (b) The positioning of the reference crucible (left) and the sample crucible (right) suspended from the scale that is positioned on top of the TG/DTG machine

After both crucibles are inserted into the TG/DTG, they are heated and cooled in a controlled atmosphere (Ar or O₂) according to a programme with predetermined heating and cooling rates. One measurement programme may contain many heating and cooling cycles in order to obtain statistically relevant data. Most measurements presented in this thesis were done under oxygen atmosphere, to discourage the potential reduction of the samples.

The TG/DTG is connected to a computer that records the data that is collected during the measurement. When a phase transition occurs, the relative change in heat flow between the reference and sample crucibles is recorded by means of an exothermic or endothermic peak (figure 2.11b). A data analysis programme allows for the determination of the phase transition temperature as is shown in figure 2.11a.

The programme calculates the onset temperature of the transition peak (T_{onset}), the offset temperature (T_{offset}) and the peak-max. temperature ($T_{\text{p-max}}$). By convention, the T_{onset} is used to determine the transition temperature of an event on the eutectic line. This is the horizontal line that crosses the eutectic point or eutectic equilibrium. At the eutectic equilibrium, a heterogeneous mixture of solid components congruently melts into a homogeneous liquid at a melting point that is lower than the melting point of any of the individual compounds. This is illustrated in figure 2.10 [142], with the eutectic point/ equilibrium (arrow) and eutectic line on the Ba – O phase di-

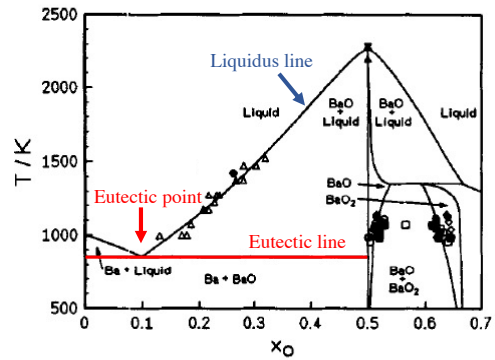
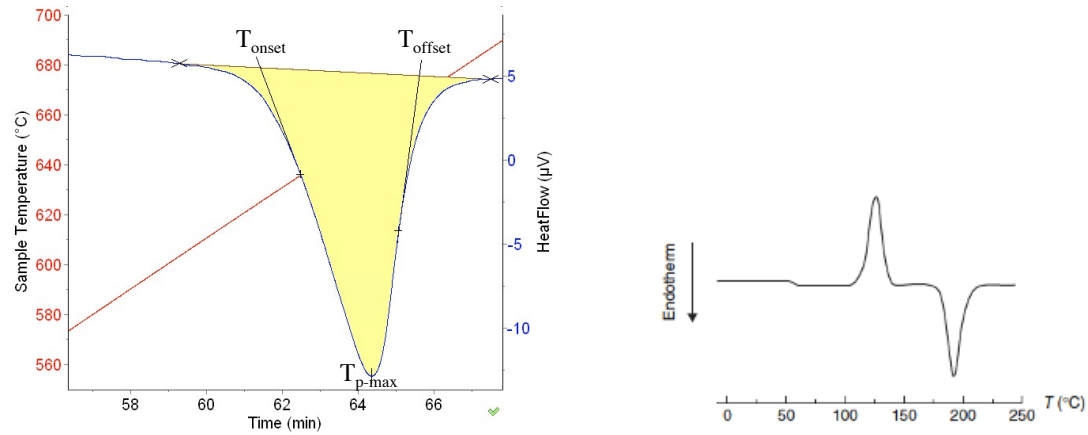


Figure 2.10: Ba-O phase diagram [142]

agram in red. The peak max. temperature is used to describe any liquidus line events, where a mixture of solid and liquid melts into one liquid phase (shown in blue in figure 2.10).



(a) TGDSC peak illustrating the position of the onset (T_{onset}), offset (T_{offset}) and peak-max. (T_{p-max}) temperatures

(b) DSC thermogram illustrating an exothermic and endothermic peak [17, 87]

Figure 2.11

The onset, offset and peak max. temperatures need to be calibrated (corrected) for the programmed heating and cooling rates during the measurement. In order to negate these effects, the (T_{onset}), (T_{offset}) and (T_{p-max}) are corrected by the following correction curve specific to the crucibles and the TGDSC device [111].

$$T_{real} = T_{meas} + A \cdot T_{meas}^2 + B \cdot T_{meas} + C + r(D \cdot T_{meas} + E) \quad (2.3)$$

The melting points of well known reference metals at various cooling and heating rates are compared to their documented melting points and corrected using a linear fit. These are all combined to give the polynomial function of equation 2.3. T_{real} is the corrected temperature, T_{meas} is the measured temperature by the TGDSC, A, B, C, D and E are constants and 'r' is the heating rate calculated by [111]:

$$r = \frac{T_{onset} - T_{offset}}{t_{onset} - t_{offset}} \quad (2.4)$$

where, t_{onset} and t_{offset} are the onset and offset time respectively. After the onset, offset and peak max. temperatures of all cycles are corrected, the eutectic and liquidus phase transition temperatures are found by taking the average of the corrected T_{onset} and T_{p-max} temperatures respectively, that are obtained over successive cycles.

2.3.2 Method

Before each measurement, two end-member compounds were mixed in a pre-determined ratio and ground with a mortar and pestle to ensure a homogenous mixture. Following that, 50 – 70mg of precisely weighed mixture was placed into an aluminium oxide TGDSC crucible (figure 2.12). To prevent the melted sample from reacting with the crucible, boron nitride (BN) or aluminium oxide (Al_2O_3) powder was added below and above the sample.



Figure 2.12: Picture of a TGDSC crucible with a pen tip for size reference (left) and a illustration of its contents after the sample and powder have been added (right)

The crucible was then inserted into the TGDSC, along with an empty reference crucible. To begin, a one-cycle measurement was performed with a heating and cooling rate of 10K/min and 20K/min respectively, to test if all expected events would be visible. If this was the case, the experiment was repeated for four more cycles at a heating rate of 10K/min and various cooling rates of 20, 10, 8 and 5K/min.

A lower cooling rate increases the separation between two peaks, which can be useful if two events occur at a similar temperature range and their peaks overlap.

After the measurement was complete, the contents of the sample crucible were emptied on a glass dish. The agglomerated sample disk (figure 2.13) was removed and ground with a mortar and pestle to make a smooth mixture. This mixture was then analysed using X-ray diffraction (XRD) to see if any unexpected phases had formed.



Figure 2.13: Picture of an agglomerated sample disk right after emptying a TGDSC crucible. The surrounding white powder is BN or Al_2O_3 . The disk is ground into a powder so that it can be measured by XRD.

2.4 Solution calorimetry

Solution calorimetry is used to determine the heat of formation of a compound. It does this by measuring the temperature change when a weighed amount of sample is dissolved in a solvent of a specific concentration. A temperature increase indicates an exothermic reaction and a temperature decrease an endothermic reaction.

Experiments were performed using the TA Instruments TAM IIITM Precision Solution Calorimeter. A carefully weighed amount of a sample is added to a 1 mL glass ampoule and closed with a wax seal. The ampoule is held by a gold stirrer (figure 2.14) in a 25 mL reaction vessel that contains the solvent. Also included in the vessel are a thermistor to measure the temperature and a sapphire tip. The tip is used to crush the ampoule during the experiment and to dissolve the sample in the solvent contained by the reaction vessel. The calorimetric unit containing the ampoule and the vessel is heated up to approximately 25°C by hand and then lifted into a calorimeter cylinder that is surrounded by a large oil bath. The bath has a constant temperature (25°C) that is regulated by a TAM-IV thermostat (accuracy: $\pm 0.0001^\circ\text{C}$ over 24h) [2].

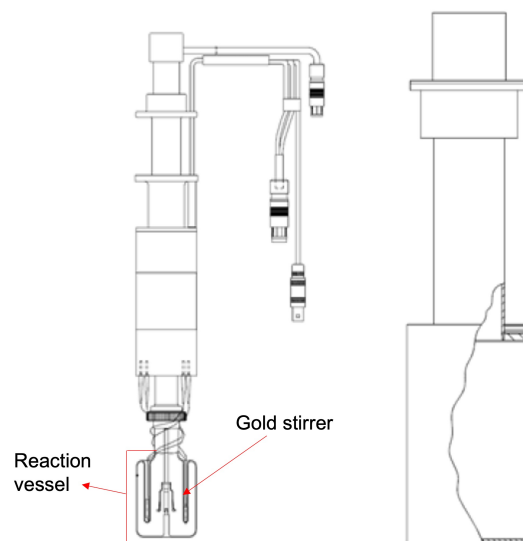


Figure 2.14: Calorimetric unit on the left, calorimetric cylinder on the right [2]

Before and after the ampoule is broken and the change in temperature is recorded, two calibration steps must be performed. Calibration is done by introducing a known amount of energy into the system and measuring the change in temperature that this gives rise to. This allows the heat capacity of the system to be determined, which can then be used to calculate the heat of the dissolution reaction (this will be explained below). When the first calibration step is complete, the ampoule is broken and the change in temperature of the reaction vessel is recorded. This process is shown in figure 2.15.

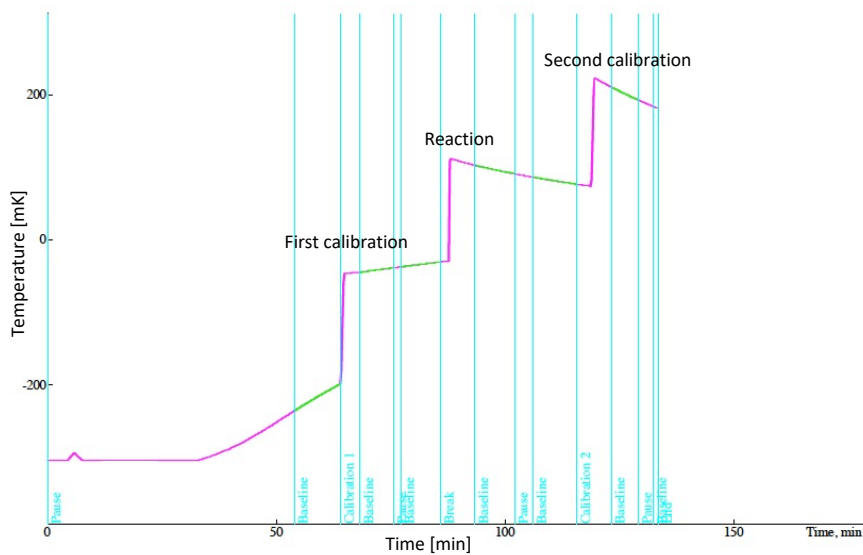


Figure 2.15: Ba_2MoO_5 in 25mL 2M HNO_3 ($y = 0$ represents 25°C)

The principle behind solution calorimetry is based on equation 2.5. It considers the heat coming into the system vs. the heat going out according to the principle of the conservation of energy.

$$-\frac{dQ}{dt} - \frac{dQ_F}{dt} = C \frac{dT}{dt} + k(T - T_S) \quad (2.5)$$

Where $\frac{dQ}{dt}$ is the heat flow caused by the dissolution reaction or electrical calibration, $\frac{dQ_F}{dt}$ is the rate of the energy dissipation caused by stirring and heating from the thermistor, $C \frac{dT}{dt}$ is the heat flow accumulated in the system and $k(T - T_S)$ is the rate of heat exchange between the vessel and its surroundings. C is the heat capacity of the calorimetric vessel, T_S the temperature of the surroundings, T the temperature of the reaction solution and k the heat exchange coefficient characteristic of the system.

During baseline sections there is no reaction or calibration step taking place and $\frac{dQ}{dt} = 0$. Therefore, a baseline equation 2.6 can be determined:

$$-\frac{dQ_f}{dt} = C \frac{dT}{dt} + k(T - T_S) \quad (2.6)$$

In case of a scenario where the baseline section continues for $t \rightarrow \infty$, the system is in a steady state and $\frac{dT}{dt} = 0$. The heat flow of the system is equal to zero since the heat that is exchanged with the surroundings is then equal to the amount of heat generated by the stirrer and the thermistor. The equation then becomes:

$$-\frac{dQ_F}{dt} = k(T_\infty - T_S) \quad (2.7)$$

Where T_∞ is the constant steady-state temperature of the vessel. When equation 2.7 is substituted into equation 2.5, the $\frac{dQ_F}{dt}$ term can be eliminated:

$$-\frac{dQ}{dt} = C \frac{dT}{dt} + k(T - T_\infty) = C \left(\frac{dT}{dt} + \frac{1}{\tau} (T - T_\infty) \right) \quad (2.8)$$

where,

$$\tau = \frac{C}{k} \quad (2.9)$$

Integration of equation 2.8 gives:

$$-Q = \int_{t_{start}}^{t_{end}} -\frac{dQ}{dt} dt = C \left[\Delta T_{obs} + \int_{t_{start}}^{t_{end}} \frac{1}{\tau} (T - T_\infty) dt \right] = C(\Delta T_{obs} - \Delta T_{adj}) \quad (2.10)$$

where,

$$\Delta T_{obs} = T_{t_{end}} - T_{t_{start}} \quad (2.11)$$

and where t_{start} and t_{end} are the times when a reaction or calibration section starts and ends. ΔT_{adj} can be calculated by finding τ and T_∞ by analysing the baseline sections. This can be done by using equation 2.8 and setting $\frac{dQ}{dt} = 0$ to get a steady-state baseline equation 2.12:

$$0 = C \frac{dT}{dt} + k(T - T_\infty) \quad (2.12)$$

Integration gives:

$$T = T_\infty + (T_0 - T_\infty) e^{-t/T} \quad (2.13)$$

where T_0 is the starting temperature of the baseline section. Fitting this equation to the baseline section gives T_∞ and eventually τ using equation 2.8. These values lead to the determination of ΔT_{obs} and ΔT_{adj} . The only unknown variables then left in equation 2.10 are Q and C . This is what the calibration steps are for. By introducing a known amount of electric energy ($Q_{\text{calibration}}$), the heat capacity of the system can be determined, which can then be used during the reaction step to determine the heat of the dissolution reaction (Q_{reaction}). Dividing this value by the amount of the sample that was dissolved gives the molar enthalpy of solution [2].

2.5 Knudsen Effusion Mass Spectrometry (KEMS)

Knudsen Effusion Mass Spectrometry (KEMS) is a high-temperature mass spectrometry technique designed to determine the gaseous components of low-volatile solids (or liquids) and to evaluate their relative partial pressures as a function of temperature. It gives a variety of thermodynamic property information about the chosen sample, as well as the ionisation and dissociation energies of the vapour species that are formed.

2.5.1 Knudsen Effusion cell

The KEMS measurement technique is based on a process called “effusion”. It is similar to diffusion, where molecules disperse through an area based on the number of collisions they experience with each other, flowing from high to low concentration areas. The average distance that a gas particle travels between two collisions is called the mean free path.

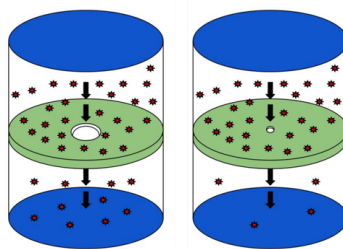


Figure 2.16: Visual representation of diffusion (left) and effusion (right) [126]

To illustrate the difference between diffusion and effusion, a scenario is considered where two chambers are separated by a barrier containing a hole (figure 2.16). One chamber is filled with a gas and the other is not. If the hole is larger than the mean free path of the gaseous particles, they will diffuse through it until the concentration in both chambers is the same. If the hole is significantly smaller than the mean free path, the gas will effuse through the so-called “pinhole” to the other chamber and the concentration of the first chamber will stay relatively constant.

Graham’s law gives the relation between the rate of effusion and the mass of a gaseous particle [1, 3]. The higher the mass (M), the slower the effusion rate:

$$\frac{\text{rate of effusion for gas A}}{\text{rate of effusion for gas B}} = \sqrt{\frac{M_B}{M_A}} \quad (2.14)$$

Because the hole is so much smaller than the mean free path, collisions between particles in the region of the hole are negligible and all particles that arrive there will pass through it. Gaseous particles that would normally collide with the wall, will pass through the pinhole [116]. By measuring the mass loss from the container over a period of time, the vapour pressure of the sample can be calculated [61]. The molecular beam that is formed by the pinhole also gives information on the gaseous particles that are released from the sample when it is passed through a mass spectrometer [112]. The effusion chamber is incorporated in a Knudsen Effusion Cell (figure 2.17).

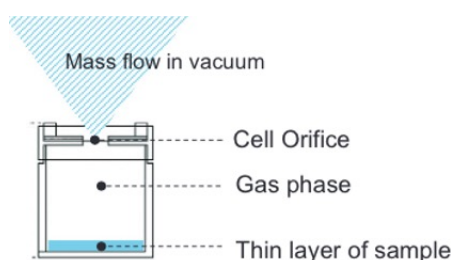


Figure 2.17: Knudsen Effusion Cell [112]

The sample is situated at the bottom of the Knudsen Cell, where it is heated under vacuum (or at a very low pressure) by a high-temperature furnace. Vacuum (or low pressure) is necessary to ensure that there are no interfering gaseous particles and so that the mean free path of the gas is large which causes molecule vs. wall collisions to dominate [112]. The mean free path is inversely proportional to the pressure [8]:

$$\lambda = \frac{kT}{\sigma p} \quad (2.15)$$

where, λ is the mean free path, k is the Boltzmann constant, p is the pressure, T the temperature and σ is the area around a molecule πd^2 , which the centre of another molecule must enter in order to cause a collision. It is called the collision cross section [8]. The Knudsen cell is made of tungsten or aluminium oxide (Al_2O_3), because of their high melting points and low reactivity. The sublimating sample forms a gaseous phase that effuses through the cell orifice (the pinhole) to form a molecular beam [122]. The effusion rate is expressed by means of the Hertz-Knudsen equation:

$$\frac{dN_i}{dt} = \frac{P_i s C}{\sqrt{2\pi M_i R T}} \quad (2.16)$$

where $\frac{dN_i}{dt}$ equals the number of species 'i' effusing through the orifice surface per unit time, P_i is the partial pressure of species 'i' at temperature T , 's' is the surface of the orifice, M_i is the molar mass and R the gas constant. 'C' is the Clausing factor and corrects for the depth of the pinhole. When $C = 1$, the pinhole shape is sharp and has no depth, but in reality, $C < 1$ [21, 122]. The mass loss associated with the effusion of molecules G_i over a period of time δt can be expressed as such:

$$G_i = \frac{dN_i}{dt} M_i \delta t = P_i s C \delta t \left(\frac{M_i}{2\pi R T} \right)^{1/2} \quad (2.17)$$

2.5.2 KEMS set-up

The Knudsen effusion cell is connected to a mass spectrometer as depicted in figure 2.18. A mass spectrometer consists of an ioniser, a mass analyser and a detector.

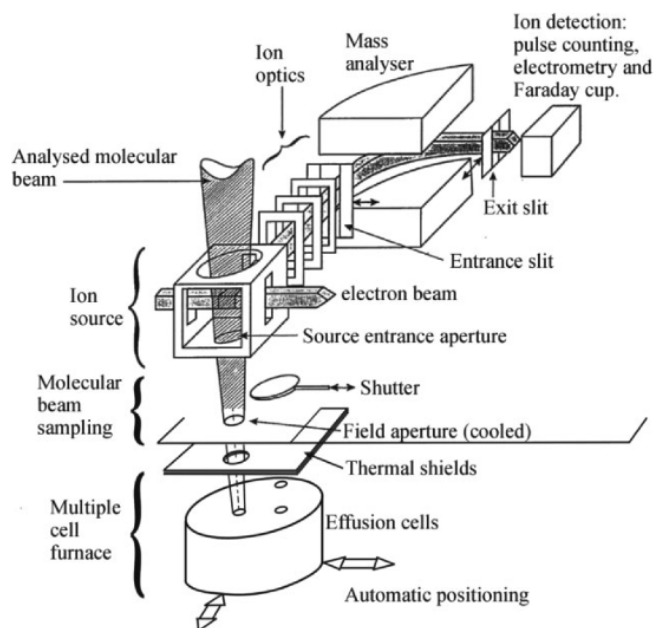


Figure 2.18: Knudsen Effusion Mass Spectrometry set-up [54]

The molecular beam emerging from the Knudsen cell is ionised by electron bombardment. High energy electrons are used to overcome the ionisation energy of the gaseous molecules. This high energy will cause ionisation, but it can also lead to fragmentation, where the emitted molecule splits into stoichiometric ions. Fragmentation complicates the determination of the vaporisation reactions that occur in the Knudsen Cell, because (obviously) the recorded fragmented ions cannot be told apart from the non-fragmented ions as they go through the mass spectrometer. This makes it difficult to piece together which ions came from their own gaseous species and which were caused by a fragmentation reaction. These equations show direct ionisation (2.18) and fragmentation (2.19) [34]:

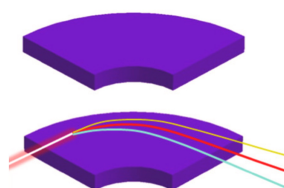
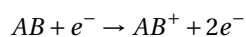


Figure 2.19: Visual representation of a magnetic mass analyser [60]

After the molecular beam is ionised, it is passed through a mass analyser, which separates the ions based on their mass-to-charge ratio. A magnetic mass analyser accelerates the ions with a negative

electric field through an electromagnet as shown in figure 2.19 until they collide with the detector. The magnet bends the path of the ions so that they are separated according to their mass and charge [122]. Ions in this magnetic field experience two equal forces; one due to the centripetal force and one due to the magnetic field. This can be expressed as follows:

$$F_C = F_B \qquad F_C = \frac{mv^2}{r} \qquad F_B = qvB \sin\theta \qquad (2.20)$$

where, m is the mass, v is the velocity, r is the radius of the circular path of the ions, q is the charge and B is the magnetic field magnitude. The path of the ions is perpendicular to the magnetic field, so $\sin(90) = 1$.

$$F_C = F_B = \frac{mv^2}{r} = qvB \qquad \text{which gives} \qquad v = \frac{Bqr}{m} \qquad (2.21)$$

The kinetic energy of the ions equals the change in potential energy, according to the conservation of energy law:

$$KE = PE \qquad \frac{mv^2}{2} = qV \qquad (2.22)$$

Substituting equation 2.21 gives:

$$\frac{m}{2} \left(\frac{Bqr}{m} \right)^2 = qV \qquad (2.23)$$

$$\frac{m}{q} = \frac{B^2 r^2}{2V} \qquad (2.24)$$

This shows that an ion with mass-to-charge ratio $\frac{m}{q}$ will follow a unique path with radius 'r' through the mass analyser if B and V can be held constant [5]. This way all ions with a different mass-to-charge ratio can be separated and their respective intensities can be recorded. This is done by a detector.

The detector receives the ion beam from the mass analyser and increases the intensity of the signal by means of an electron multiplier. It consists of a series of metal dynodes (made of a Be-Cu alloy) that are arranged in such a way that they can increase and reflect the signal to the next dynode (figure 2.20). The first dynode is negatively charged to attract the ion beams that come out of the mass analyser. When they collide with each other, the dynode generates a shower of secondary electrons. These are then attracted to the second dynode, and so on, until the ion beam signal has been multiplied by an order of 10^6 [85]. The signals from the detector are recorded by a computer as graphs of intensity vs. time, temperature or electronvolt (eV).

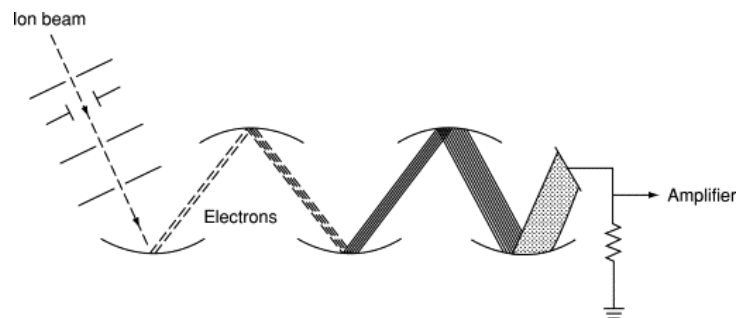


Figure 2.20: Electron multiplier with multiple dynodes [85]

2.5.3 Partial pressure calculation

One of the most important data that result from a KEMS measurement, is the partial pressure of all gaseous species that form during the sublimation of the sample. In order for the partial pressure calculations to be accurate, it is important to determine which ions came from fragmentation and which came directly from the ionisation of a molecule (equations 2.18 and 2.19). How this puzzle is solved will be discussed in chapter 4 with the experimental results. For now, let's assume that all fragmented ions have been determined.

First, the KEMS equipment has to be calibrated so that every measurement yields the same results, independent of which machine was used. This is done by measuring a well-documented sample, such as silver, and calculating the partial pressure of its two isotopes, 107-Ag and 109-Ag. The partial pressures of these isotopes are added together with a weight factor according to their natural abundance. The measured total vapour pressure of silver (vs. temperature) is compared to the documented vapour pressure and corrected with a calibration instrumental factor K_{Ag} .

Before the partial pressure of each gaseous molecule can be calculated, their ionisation cross section needs to be determined. The ionisation cross section of an atom or molecule essentially describes how close an electron needs to get to the atom/ molecule in order for an ionisation reaction to take place. It is not equal to the atomic or molecular radius, because different electron configurations and molecular bonding strengths have an impact on the readiness of an atom or molecule to undergo ionisation. The ionisation cross sections of atoms are well-documented [34], but molecular cross sections are more difficult to find and had to be approximated for the purposes of this thesis. This approximation was done using the methodology developed by Deutsch et al. [31] for basic molecules of the form AB_n [30] and more complicated molecules $A_xB_yC_z$ and $A_pB_sC_tD_u$ [29]. It relies on a simple model of adding cross sections of the relevant atoms together in a stoichiometric ratio, but it also introduces a weighting factor 'f' per atomic cross section which takes into account the effect of molecular bonding. The general equations look like this [29, 30]:

$$\sigma^+(AB_n) = f_a(r_A, r_B, \xi_A, \xi_B)\sigma^+(A) + f_b(r_A, r_B, \xi_A, \xi_B)n\sigma^+(B) \quad (2.25)$$

$$\begin{aligned} \sigma^+(A_xB_yC_z) = & [(y+z)/x]^\alpha f_x(r_A, r_B, r_C, \xi_A, \xi_B, \xi_C)x\sigma^+(A) \\ & + [(x+z)/y]^\beta f_y(r_A, r_B, r_C, \xi_A, \xi_B, \xi_C)y\sigma^+(B) \\ & + [(x+y)/z]^\gamma f_z(r_A, r_B, r_C, \xi_A, \xi_B, \xi_C)z\sigma^+(C) \end{aligned} \quad (2.26)$$

where, $\sigma^+(AB_n)$ and $\sigma^+(A_xB_yC_z)$ are the ionisation cross sections of the molecules AB_n and $A_xB_yC_z$, f_a , f_b and f_c are weighting factors depending on the radius of atom A (r_A), B (r_B) and C (r_C) and the effective number of electrons of A (ξ_A), B (ξ_B) and C (ξ_C). The weighting factors are multiplied by the respective stoichiometrically weighed ionisation cross sections of atoms A, B and C. Filling in the equations for the weighting factors, give the molecular cross section equations [29, 30]:

$$\sigma^+(AB_n) = [r_A^2/r_B^2]^\alpha [\xi_A/(\xi_A + n\xi_B)]\sigma^+(A) + [(nr_B^2)/r_A^2]^\beta [n\xi_B/(\xi_A + n\xi_B)]n\sigma^+(B) \quad (2.27)$$

$$\begin{aligned} \sigma^+(A_xB_yC_z) = & [(y+z)/x]^\alpha [r_A^2/(r_B^2 + r_C^2)]^\alpha [x\xi_A/(y\xi_B + z\xi_C)]x\sigma^+(A) \\ & + [(x+z)/y]^\beta [r_B^2/(r_A^2 + r_C^2)]^\beta [y\xi_B/(x\xi_A + z\xi_C)]y\sigma^+(B) \\ & + [(x+y)/z]^\gamma [r_C^2/(r_A^2 + r_B^2)]^\gamma [z\xi_C/(x\xi_A + y\xi_B)]z\sigma^+(C) \end{aligned} \quad (2.28)$$

where exponents α , β and γ are given by:

$$\alpha = g_1(\alpha^*) \quad \beta = g_2(\beta^*) \quad \gamma = g_2(\gamma^*) \quad (2.29)$$

with:

$$\begin{aligned} \alpha^* &= r_A / (r_B + r_C) \xi_A / (\xi_B + \xi_C) \\ \beta^* &= r_B / (r_A + r_C) \xi_B / (\xi_A + \xi_C) \\ \gamma^* &= r_C / (r_A + r_B) \xi_C / (\xi_A + \xi_B) \end{aligned} \quad (2.30)$$

The functions $g_1(\alpha^*)$, $g_2(\beta^*)$ and $g_2(\gamma^*)$ have been determined empirically. The exponents α , β and γ can be found using the graph depicted below [29, 30].

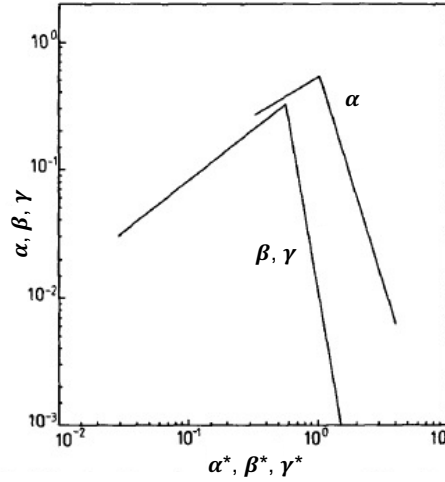


Figure 2.21: Functions to determine α , β and γ . Adapted from [30]

Now that the molecular ionisation cross sections have been calculated, the factor H_i can be determined with the calibration factor K_{Ag} , the cross sections of gaseous species 'i' (σ_i) and silver (σ_{Ag}) and the molecular mass of species 'i' (M_i) and silver (M_{Ag}) [122]:

$$H_i = \frac{\sigma_{Ag}}{K_{Ag} \sigma_i \sqrt{M_i M_{Ag}}} \quad (2.31)$$

Using H_i , the partial pressure can be calculated. The partial pressure is calculated for every gaseous species formed in the Knudsen effusion cell. The addition of all these partial pressures then gives the vapour pressure of the sample material as a function of temperature. When it is clear which ionic species originated from which gaseous molecule, the intensity vs. temperature data of those ions are used to calculate the partial pressures. It is possible for one ionic species to originate from multiple molecules. For example, Ba^+ can originate from the ionisation of $Ba(g)$, but also from a fragmentation reaction with $BaMoO_4(g)$. The ratio of these reactions is determined with the intensity vs. eV data and will be discussed in chapter 4. It is used as a weight factor for the intensity values of the ions to calculate the partial pressure of the molecule. For example, if 20% of the Ba^+ ions were created by the ionisation reaction with $Ba(g)$ and 80% by fragmentation of $BaMoO_4(g)$, then the intensity values

of Ba^+ will be multiplied by 0.20 to calculate the partial pressure of $\text{Ba}(\text{g})$. The remaining 80% of the intensity would be allocated to the partial pressure of $\text{BaMoO}_4(\text{g})$. The equation is as such:

$$P_i = H_i \sum_k I_k T M_k^{1/2} \quad (2.32)$$

where, H_i is the factor calculated by equation 2.31, I_k is the intensity of ionic species 'k', T is the temperature, M_k is the molar mass of species 'k' and P_i is the partial pressure of gaseous molecule 'i' [122].

2.6 CALPHAD modelling

The CALPHAD (Calculation of Phase Diagram) method combines thermodynamic property databases with mathematical models to calculate the thermodynamic stability and properties of multicomponent, multiphase systems as a function of temperature, composition and pressure [50]. For the purpose of this thesis, CALPHAD is used to model phase diagrams by calculating the temperature dependence of phase equilibria as a function of their composition. It does this by minimising the Gibbs free energy of the system (including all stable phases in the system) so that $dG = 0$. A general expression for the Gibbs energy function of a phase α is [128]:

$$G_m^\alpha = G_m^{\alpha, \text{ref}} + G_m^{\alpha, \text{id}} + G_m^{\alpha, \text{excess}} + G_m^{\alpha, \text{phy}} \quad (2.33)$$

where G_m^{id} is the ideal mixing term (assuming no interactions between constituents in a phase), G_m^{phy} is a term used to account for the contribution of any physical effects (like magnetic transitions) and G_m^{excess} is the excess Gibbs energy term that describes the deviation between the ideal and the observed Gibbs energy of mixing functions. G_m^{ref} is the Gibbs energy reference term, representing the combined Gibbs energy contribution of the elements and/ or stoichiometric compounds in the phase. The stoichiometric compounds are called the constituents of a phase. The Gibbs energy of one pure element or stoichiometric compound appearing in stable form α at standard temperature and pressure, is represented by the following polynomial function [132] that can be formulated based on experimental data or supplied by a database such as TAF-ID (the Thermodynamics of Advanced Fuels – International Database [51]).

$$G_A^\alpha(T) = a_0 + a_1 T + a_2 T \cdot \ln T + a_3 T^2 + a_4 T^{-1} + a_5 T^3 + \dots \quad (2.34)$$

The following thermodynamic definitions:

$$H = G - T \left(\frac{\delta G}{\delta T} \right)_{p, N_i} \quad S = - \left(\frac{\delta G}{\delta T} \right)_{p, N_i} \quad C_p = -T \left(\frac{\delta^2 G}{\delta T^2} \right)_{p, N_i} \quad (2.35)$$

can subsequently be used to calculate the polynomial functions for entropy, enthalpy and heat capacity [132]:

$$H_m^\alpha = a_0 - a_2 T + a_3 T^2 + 2a_4 T^{-1} - 3a_5 T^3 + \dots \quad (2.36)$$

$$S_m^\alpha = -a_1 - a_2(1 + \ln T) - 2a_3 T + a_4 T^{-2} - 3a_5 T^2 + \dots \quad (2.37)$$

$$C_p^\alpha = -a_2 - a_3 T - 2a_4 T^{-2} - 6a_5 T^2 + \dots \quad (2.38)$$

CALPHAD offers a range of model options to do phase calculations on a system, depending on that system's characteristics. The G_m^{ref} , G_m^{ideal} and G_m^{excess} functions shown in equation 2.33 all depend on the type of model that is chosen to describe the system. The models that were used in this thesis for the gaseous, liquid and solid phases are discussed below.

2.6.1 Solid phase: the Compound Energy Formulism (CEF)

The solid phase, having long-range ordering with fixed atomic positions contained in a lattice structure, is described using a sublattice model called the Compound Energy Formulism (CEF). It defines the solid phase as being composed of interlocking sublattices that house individual components on fixed lattice sites. These components can mix on the sublattices to form the stoichiometric compounds (end-members) that occur in a phase diagram. The Gibbs energy expression has the same form as equation 2.33, with a G^{ref} , G^{ideal} , G^{excess} and G^{phys} :

$$G = G^{ref} + G_{mix}^{ideal} + G_{mix}^{excess} + G_{mix}^{phys} \quad (2.39)$$

This is a general representation of the sublattice system according to the CEF [50]:

$$(A, B, C, \dots)(D, E, F, \dots)(G, H, I, \dots) \quad (2.40)$$

where the sublattices and the components are represented by the brackets and the letters respectively. A site fraction of each component 'i' on each sublattice 's' is defined as follows:

$$y_i^s = \frac{n_i^s}{N^s} \quad (2.41)$$

where y_i^s is the site fraction, n_i^s the number of atoms of component 'i' on sublattice 's' and N^s the total number of sites on sublattice 's'. N^s is defined as the total number of atoms on sublattice 's' plus the number of vacancies (n_{Va}^s):

$$N^s = n_{Va}^s + \sum_i n_i^s \quad (2.42)$$

This results in the ideal Gibbs energy of mixing function:

$$G_{mix}^{ideal} = -TS_{mix}^{ideal} = RT \sum_s N^s \sum_i y_i^s \ln y_i^s \quad (2.43)$$

The G_{ref} term is defined by the end-members of the sublattice model. To illustrate this, a simple two-sublattice system is taken as a case study, with the following formula [114]:

$$(A, B)_1(C, D)_1 \quad (2.44)$$

The end-members of this system are formed when only pure components exist on each sublattice. For example, when only A occupies sublattice 1 and only C occupies sublattice 2, the end-member AC is formed. This results in four end-members for this system: AC, AD, BC and BD as is represented in figure 2.22. The area within the square represents the composition of the phase.

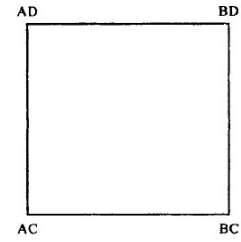


Figure 2.22: Representation of the $(A, B)_1(C, D)_1$ sublattice [114]

G_{ref} is then the summation of the Gibbs energy functions of the end-members (in the polynomial format shown by equation 2.34) times the relevant site fractions [50, 114]:

$$G_m^{ref} = y_A y_C G_{AC}^\circ + y_B y_C G_{BC}^\circ + y_A y_D G_{AD}^\circ + y_B y_D G_{BD}^\circ \quad (2.45)$$

Or extrapolated to the general expression [114]:

$$G_m^{ref} = \sum_I P_I(Y) \cdot G_I^\circ \quad (2.46)$$

where G_T° represents the Gibbs energy function of end-member 'T' and $P_1(Y)$ represents the product of the corresponding site fractions of 'T'. Filling the expressions for G^{ideal} and G^{ref} into equation 2.39 gives the general expression of the Gibbs energy function according to the Compound Energy Formulism [114]:

$$G_m(T) = \sum P_{I_o}(Y)^0 G_{I_o} + RT \sum_{s=1}^n a_s \sum_{i=1}^{n_s} y_i^l \ln(y_i^l) + G_m^{\text{excess}} + G_m^{\text{phys}} \quad (2.47)$$

The G_{phys} term depends on the properties of the system that is modelled and is added here for accuracy but will not be discussed further. The G_{excess} term is optimised during CALPHAD modelling.

2.6.2 Liquid phase: the Ionic two-Sublattice Model (I2SL)

The liquid phase is described using the Ionic two-Sublattice model (I2SL). It is an adaptation of the sublattice model that can account for a pure metallic phase as well as metallic oxides [64]. It does this by modifying the sublattice equation 2.40 to create two sublattices (cationic and anionic) [50]:

$$(C_i^{+v_i})_P (A_j^{-v_j}, Va^{-Q}, B_k^0)_Q \quad (2.48)$$

The first sublattice contains cations ($C_i^{+v_i}$) and the second sublattice contains anions ($A_j^{-v_j}$), vacancies (Va^{-Q}) and neutral species (B_k^0). The terms 'i', 'j' and 'k' represent specific constituents. P and Q are calculated with the following equations [114]:

$$P = \sum_j y_{A_j} v_j + Q y_{Va} \quad (2.49)$$

$$Q = \sum_i y_{C_i} v_i \quad (2.50)$$

where y_{A_j} and y_{C_i} are the site fractions of the j-th anion and i-th cation respectively. P and Q are equal to the total charge of the opposite sublattice, so that the system upholds electroneutrality. If the cationic sublattice (P) is more positive than the anionic sublattice (Q) is negative, the vacancy corrects for this by also carrying a charge.

With this adjusted model, equation 2.47 can be modified to give:

$$G_m(T) = \sum_i \sum_j y_{C_i} y_{A_j} G_{C_i:A_j} + Q y_{Va} \sum_i y_{C_i} G_{C_i} + Q \sum_k y_{B_k} G_{B_k} + RT \left[P \sum_i y_{C_i} \ln y_{C_i} + Q \left(\sum_j y_{A_j} \ln y_{A_j} + y_{Va} \ln y_{Va} + \sum_k y_{B_k} \ln y_{B_k} \right) \right] + G_m^{\text{excess}} \quad (2.51)$$

The G^{ref} function is encompassed by the first three terms showing the Gibbs energy contribution by the end-members (in the polynomial format shown by equation 2.34), including metals and neutral species, and the fourth term represents the ideal Gibbs mixing term. The G^{excess} term is rather extensive, because it has to account for the interactions between all constituents:

$$G_m^{\text{excess}} = \sum_{i_1} \sum_{i_2} \sum_j y_{C_{i_1}} y_{C_{i_2}} y_{A_j} L_{C_{i_1}, C_{i_2}:A_j} + Q y_{Va}^2 \sum_{i_1} \sum_{i_2} y_{C_{i_1}} y_{C_{i_2}} L_{C_{i_1}, C_{i_2}:Va} + \sum_i \sum_{j_1} \sum_{j_2} y_{C_i} y_{A_{j_1}} y_{A_{j_2}} L_{C_i, A_{j_1}:A_{j_2}} + y_{Va} \sum_i \sum_j y_{C_i} y_{A_j} L_{C_i:A_j, Va} + \sum_i \sum_j \sum_k y_{C_i} y_{A_j} y_{B_k} L_{C_i:A_j, B_k} + Q y_{Va} \sum_i \sum_k y_{C_i} y_{B_k} L_{C_i:B_k, Va} + \sum_{k_1} \sum_{k_2} y_{B_{k_1}} y_{B_{k_2}} L_{B_{k_1}, B_{k_2}} \quad (2.52)$$

Each term represents the interaction between two or three constituents. For example, the first term accounts for the interaction between two cations and one anion (like $L_{(Ca^{+2},Mg^{2+},O^{-2})}$ for the system CaO – MgO) and the second term represents the interaction between two metallic elements (like $L_{(Ca^{+2},Mg^{+2},Va)}$ in Ca – Mg) [50]. The interaction parameters are assumed to have a linear relationship with temperature: $L = a_0 + a_1 T$. These parameters are optimised during CALPHAD modelling.

2.6.3 Gaseous phase: ideal mixture

The gaseous phase is assumed to be an ideal mixture of gaseous species 'i' and is described by the following function [120]:

$$G^\psi = \sum_i y_i {}^\circ G_i^\psi + RT \ln \frac{P}{P^\circ} + RT \sum_i y_i \ln y_i \quad (2.53)$$

The first and second term together represent the Gibbs energy of a ideal gas (at standard temperature and pressure) and the third term represents the Gibbs energy of mixing of a perfect gas. G_i^ψ is the standard Gibbs energy of the gaseous species i, y_i is the fraction of the species i in the gas phase, and P° is the standard pressure. The gaseous phase was not optimised in this thesis.

Chapter 3

Experimental, Results and Discussion

This chapter contains a variety of experimental research about the following three systems: (3.1) Ba-Mo-O, (3.2) Ba-Cs-Mo-O and (3.3) Sr-Mo-O. They include the synthesis results of BaMoO₄, BaMo₃O₁₀, Ba₂MoO₅, Ba₃MoO₆ and BaCs₂(MoO₄)₂, as well as the phase diagram investigations for the BaMoO₄ - MoO₃, BaMoO₄ - Cs₂MoO₄ and SrMoO₄ - MoO₃ pseudo-binary sections. Each individual experimental method is accompanied by a direct discussion of the results, due to the large amount of experiments that were conducted.

Synthesis conditions

Table 3.1: Synthesis conditions

| Compound | Starting reagents ^a | Atmosphere ^b | Crucible | Conditions ^c | Result |
|--|---|-------------------------|--------------------------------|---|----------------------|
| BaMoO ₄ | BaCO ₃ + MoO ₃ | Air | Al ₂ O ₃ | 2 cycles for 12h at 973K ^d | Successful |
| BaMo ₃ O ₁₀ | BaMoO ₄ + 2MoO ₃ | O ₂ | Platinum | 1 cycle for 12h at 823K and 2h at 993K and 3 cycles at 823K for 12h each. | Partially successful |
| | | O ₂ | Platinum | 3 cycles for 12h at 823K | Partially successful |
| | BaCO ₃ + MoO ₃ | Air | Platinum | 1 cycle for 4 days at 893K and 1 cycle for 2 days at 893K | Successful |
| Ba ₂ MoO ₅ | BaMoO ₄ + BaO | O ₂ | Al ₂ O ₃ | 3 cycles for 12h at 1473K | Partially successful |
| | | O ₂ | Al ₂ O ₃ | 2 cycles for 12h at 1273K | Successful |
| Ba ₃ MoO ₆ | BaMoO ₄ + BaO | O ₂ | Al ₂ O ₃ | 2 cycles for 12h at 1273K | Partially successful |
| | Ba ₂ MoO ₅ + BaO | O ₂ | Al ₂ O ₃ | 3 cycles for 12h at 1273K | Partially successful |
| Cs ₂ MoO ₄ | Cs ₂ CO ₃ + BaO | O ₂ | Al ₂ O ₃ | 2 cycles for 12h at 973K | Successful |
| BaCs ₂ (MoO ₄) ₂ | BaMoO ₄ + Cs ₂ MoO ₄ | O ₂ | Al ₂ O ₃ | 3 cycles for 24h, 14h and 24h at 1023K ^e | Successful |

^aAll mixtures were mixed and ground for 15 minutes using a mortar and pestle to ensure a homogeneous mixture.

^bAll in high-temperature furnaces. O₂: Ceradel tubular furnace, model PTF 12/50/250, air: Borel furnace, model TL1100-6.

^cAlways a 15 minute regrinding step in between cycles.

^dInitially attempted at 1073K, but this caused melting of MoO₃ (MP = 1074K [38])

^eNumber of cycles was not specified by Smith et al. [123], 3 cycles were chosen for practical reasons.

Table 3.1 shows the conditions of the solid syntheses that were performed. Only the successful syntheses will be discussed in this chapter, the partially successful syntheses are reported in Appendix A. The synthesis of Cs_2MoO_4 is not described, because of its well known synthesis method. For more information on this synthesis, see Wallez et al. [138] and the master thesis by Wouter Burik [132].

3.1 Ba-Mo-O system: investigation of the BaMoO_4 - MoO_3 pseudo-binary section

The Ba-Mo-O system includes a large number of compounds, not all of which will be discussed in this chapter. This chapter will address the $\text{BaO} - \text{MoO}_3$ pseudo-binary section, with special focus on the compositional region $0.5 \leq x(\text{MoO}_3) \leq 1.0$ for which TGDSC experiments were conducted. The successful synthesis of BaMoO_4 and $\text{BaMo}_3\text{O}_{10}$ (for the TGDSC measurements) and the partially successful synthesis of Ba_3MoO_6 will be covered, as well as a new synthesis method to successfully produce Ba_2MoO_5 , which allowed for some preliminary solution calorimetry measurements. All synthesis methods and conditions are described by table 3.1. Only the successful syntheses will be discussed, the partially successful synthesis results can be found in Appendix A. Section 3.1 is divided into the syntheses and structural characterisation of the aforementioned compounds (3.1.1), the solution calorimetry results of Ba_2MoO_5 (3.1.2) as well as the TGDSC measurement results for the $\text{BaO} - \text{MoO}_3$ pseudo-binary section (3.1.3).

3.1.1 Syntheses and structural characterisation

3.1.1.1 BaMoO_4



BaMoO_4 was successfully synthesised by means of the method described in table 3.1. It yielded a white powder that is stable under ambient atmosphere (see figure 3.1). An XRD measurement and subsequent Rietveld refinement was done to test the purity of the synthesis, which can be seen below in figure 3.2. The refined lattice parameters and atomic positions are shown in table 3.2 and 3.3.



Figure 3.1: Picture of aluminum oxide crucibles with BaMoO_4 after the last cycle in the oven

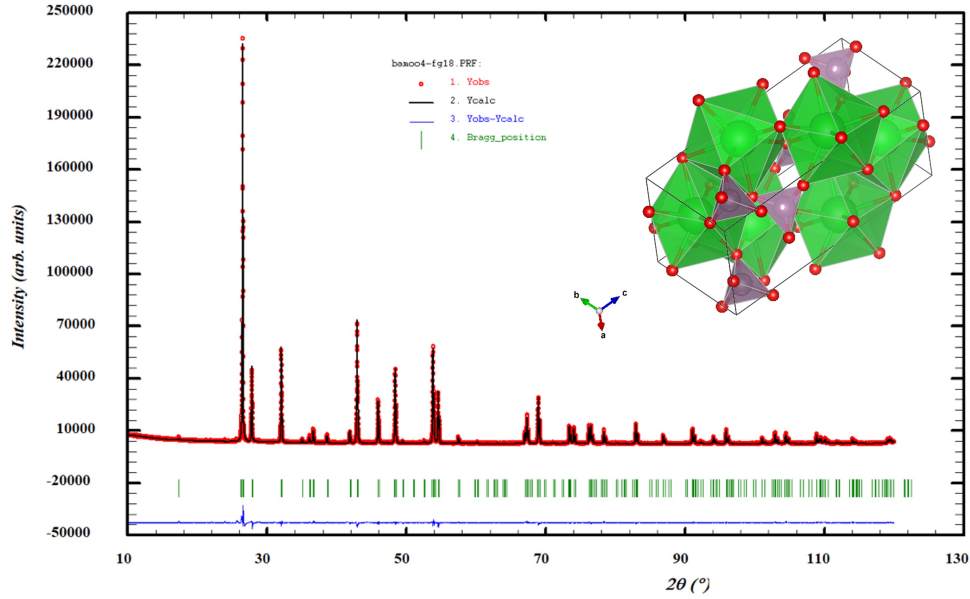


Figure 3.2: Rietveld refinement of BaMoO_4 ($\chi^2 = 6.67$). Comparison between the observed (Y_{obs} , in red) and calculated (Y_{calc} , in black) X-ray diffraction patterns. $Y_{\text{obs}} - Y_{\text{calc}}$, in blue, is the difference between the experimental and calculated intensities. The Bragg's reflection angular positions are marked in green. The BaMoO_4 unit cell sketch shows oxygen atoms in red, molybdenum polyhedra in purple and barium polyhedra in green.

Table 3.2: Refined lattice parameters of BaMoO_4

| Space group $I41/a$ (88), $\alpha = \beta = \gamma = 90^\circ$ | |
|--|--------------------------------|
| Lattice parameter | Refined value [\AA] |
| a | 5.5817(1) |
| b | 5.5817(1) |
| c | 12.8197(2) |

Table 3.3: Refined atomic positions of BaMoO_4

| Element | Wyck. | x | y | z | B |
|---------|-------|-----------|-----------|-----------|---------|
| Ba | 4b | 0 | 1/4 | 5/8 | 0.99(2) |
| Mo | 4a | 0 | 1/4 | 1/8 | 1.21(2) |
| O | 16f | 0.1054(6) | 0.0318(6) | 0.1940(2) | 1.6(1) |

3.1.1.2 $\text{BaMo}_3\text{O}_{10}$

Method 1: partially successful



Two variations of this method were attempted that were unfortunately only partially successful. The synthesis conditions of both of these methods are described in table 3.1 and the results can be found in Appendix A.1.

Method 2: successful



A second synthesis method, as described by Werner et al. [95] (table 3.1), was attempted. BaCO_3 and MoO_3 were mixed in a 1:3 ratio and ground for 15 minutes using a mortar and pestle. This mixture (200 mg) was placed into a platinum crucible and heated for four days at 893K under air. The resulting powder had a green hue and did not show any signs of crystal formation. Rietveld refinement did not show any unidentified peaks, however, the χ^2 value was still fairly high. Therefore, a second cycle was done for 2 days at 893K under air with ± 90 mg of mixture in each platinum crucible. After this cycle, the sample still had a green hue and no crystal formation (figure 3.3). The Rietveld refinement after this cycle (figure 3.4) showed a pure sample.



Figure 3.3: Picture of two platinum crucibles with $\text{BaMo}_3\text{O}_{10}$ after the second cycle in the oven

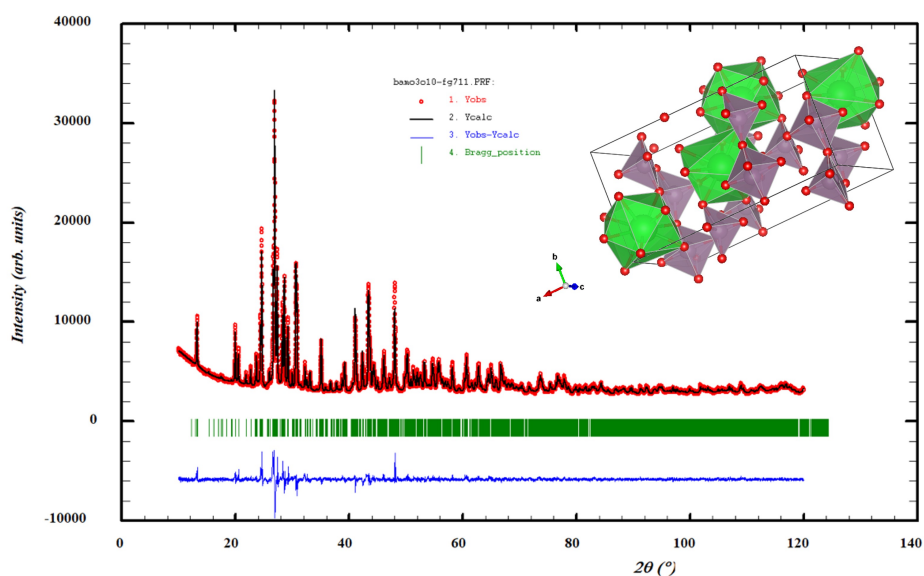


Figure 3.4: Rietveld refinement of $\text{BaMo}_3\text{O}_{10}$ after 2 cycles ($\chi^2 = 5.8$). Comparison between the observed (Y_{obs} , in red) and calculated (Y_{calc} , in black) X-ray diffraction patterns. $Y_{\text{obs}} - Y_{\text{calc}}$, in blue, is the difference between the experimental and calculated intensities. The Bragg's reflection angular positions are marked in green. The $\text{BaMo}_3\text{O}_{10}$ unit cell sketch shows oxygen atoms in red, molybdenum polyhedra in purple and barium polyhedra in green.

The refined lattice parameters and atomic positions are shown in table 3.4 and 3.5 below. It was not possible to refine the position of the oxygen atoms, a convergence could not be reached by the FullProf programme when they were selected.

Table 3.4: Refined lattice parameters of BaMo₃O₁₀

| Space group P21(4), $\alpha = \gamma = 90^\circ$ | |
|--|---------------------|
| Lattice parameter | Refined value [Å] |
| a | 14.6971(9) |
| b | 7.5712(4) |
| c | 6.9648(5) |
| β | 100.403(5) $^\circ$ |

Table 3.5: Refined (only Ba and Mo) atomic positions of BaMo₃O₁₀. Oxygen elements have no error values because they were not refined. Based on crystal structure data by Werner et al. [95].

| Label | Element | Wyck. | x | y | z |
|-------|---------|-------|-----------|----------|----------|
| Ba1 | Ba | 2a | 0.0710(6) | 0.745(4) | 0.888(1) |
| Ba2 | Ba | 2a | 0.5651(6) | 0.497(4) | 0.371(1) |
| Mo1 | Mo | 2a | 0.651(1) | 0.238(4) | 0.935(2) |
| Mo2 | Mo | 2a | 0.3836(9) | 0.238(4) | 0.060(2) |
| Mo3 | Mo | 2a | 0.850(1) | 0.507(4) | 0.577(2) |
| Mo4 | Mo | 2a | 0.1194(9) | 0.528(4) | 0.439(2) |
| Mo5 | Mo | 2a | 0.1605(7) | 0.254(4) | 0.802(1) |
| Mo6 | Mo | 2a | 0.6681(7) | 0.009(4) | 0.332(1) |
| O1 | O | 2a | 0.3650 | 0.9960 | 0.0280 |
| O2 | O | 2a | 0.6390 | 0.9990 | 0.0030 |
| O3 | O | 2a | 0.4950 | 0.2540 | 0.0030 |
| O4 | O | 2a | 0.4120 | 0.7320 | 0.3060 |
| O5 | O | 2a | 0.2360 | 0.7590 | 0.0860 |
| O6 | O | 2a | 0.3270 | 0.7460 | 0.7610 |
| O7 | O | 2a | 0.4070 | 0.2630 | 0.3100 |
| O8 | O | 2a | 0.3190 | 0.2610 | 0.7570 |
| O9 | O | 2a | 0.2410 | 0.2460 | 0.0560 |
| O10 | O | 2a | 0.1250 | 0.7580 | 0.4830 |
| O11 | O | 2a | 0.1310 | 0.2540 | 0.4920 |
| O13 | O | 2a | 0.0090 | 0.5100 | 0.5110 |
| O14 | O | 2a | 0.0900 | 0.0090 | 0.1950 |
| O15 | O | 2a | 0.2610 | 0.0120 | 0.4010 |
| O16 | O | 2a | 0.1620 | 0.0080 | 0.7330 |
| O17 | O | 2a | 0.9120 | 0.9940 | 0.8110 |
| O18 | O | 2a | 0.8200 | 0.9920 | 0.2510 |
| O19 | O | 2a | 0.7380 | 0.0140 | 0.5500 |
| O20 | O | 2a | 0.0540 | 0.2560 | 0.8780 |

3.1.1.3 Ba₂MoO₅



Method 1: Partially successful

The synthesis conditions for the first method are described in table 3.1. It was only partially successful and the results are discussed in the Appendix A.2.

Method 2: Successful

As can be seen by looking at the BaO - MoO₃ phase diagram (figure 3.5), the temperature of the previous synthesis (1473K) comes very close to the Ba₂MoO₅ peritectic line in the model at 1562K [120], which caused the compound to decompose during the synthesis. To prevent this, the temperature of the next synthesis was lowered to 1273K.

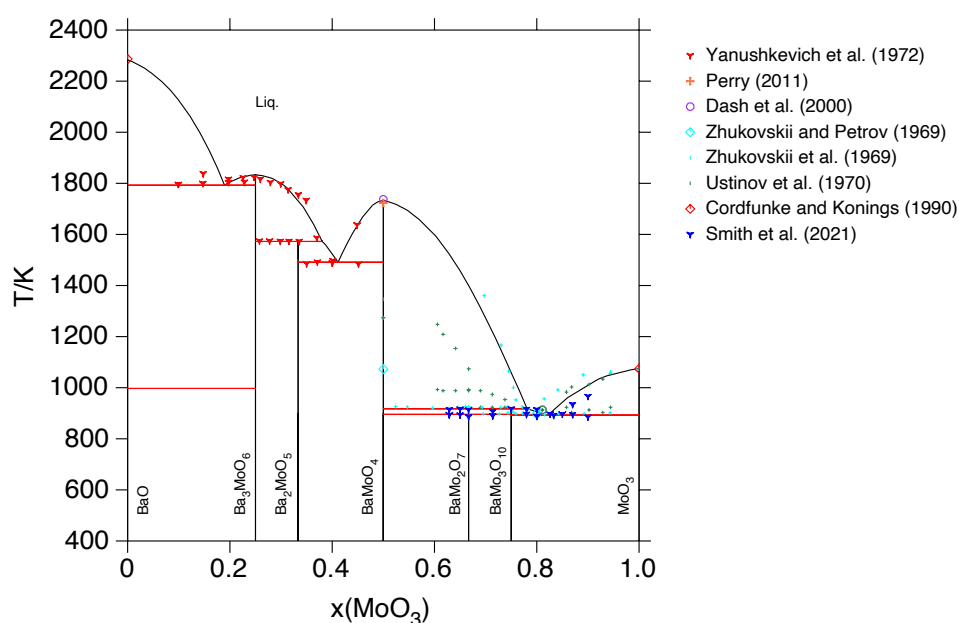


Figure 3.5: (1-x)BaO - (x)MoO₃ phase diagram

BaMoO₄ and BaO were mixed in a 1:1 ratio and ground for 15 minutes with a mortar and pestle. The mixture (300 mg) was put into a large aluminium crucible and heated under O₂ for one cycle at 1273K for 12h. The resulting powder was significantly lighter and softer than the previous synthesis with method 1 (figure 3.6):



Figure 3.6: Picture of an aluminium oxide crucible with Ba₂MoO₅ after the first cycle in the oven

Rietveld refinement showed that the purity of the sample had improved compared to the first method, even though some unidentified peaks could still be seen around 26 and 29°. A three-phase (BaMoO_4 , BaO and Ba_2MoO_5) Rietveld analysis (Appendix: figure B.5) showed a presence of $95.2 \pm 0.4\%$ Ba_2MoO_5 , $4.6 \pm 0.2\%$ BaMoO_4 and $0.2 \pm 0.1\%$ BaO (all wt%), which is a significant improvement to the previous synthesis method. To remove the small amount of BaMoO_4 , a second cycle was done at 1273K for 12h. This did not change the colour of the resulting powder (figure 3.7). XRD and subsequent Rietveld analysis showed a pure sample (figure 3.8). The refined atomic positions and lattice parameters are shown in table 3.6 and 3.7.



Figure 3.7: Picture of an aluminium oxide crucible with Ba_2MoO_5 after the second cycle in the oven

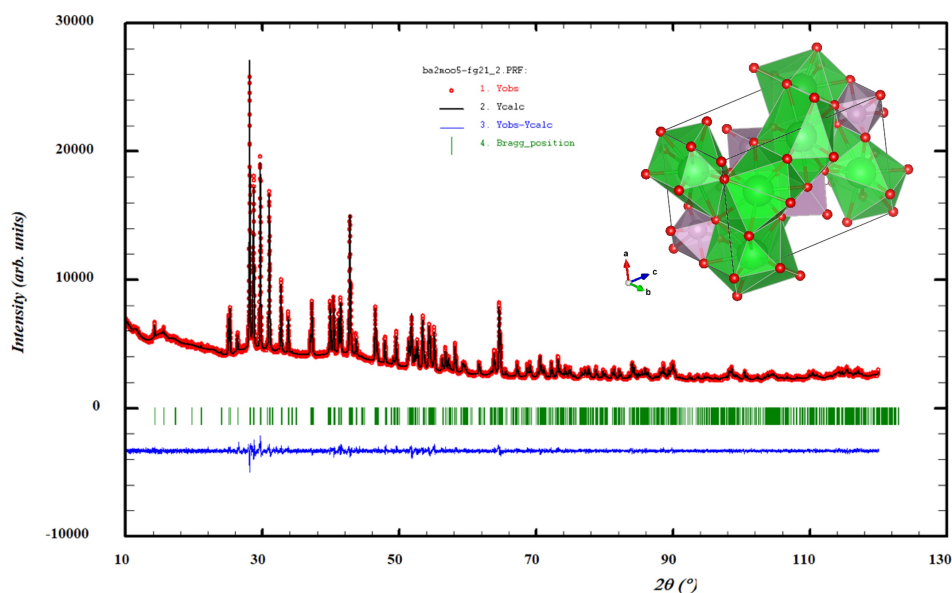


Figure 3.8: Rietveld refinement of Ba_2MoO_5 after 2 cycles ($\chi^2 = 2.14$). Comparison between the observed (Y_{obs} , in red) and calculated (Y_{calc} , in black) X-ray diffraction patterns. $Y_{\text{obs}} - Y_{\text{calc}}$, in blue, is the difference between the experimental and calculated intensities. The Bragg's reflection angular positions are marked in green. The Ba_2MoO_5 unit cell sketch shows oxygen atoms in red, molybdenum polyhedra in purple and barium polyhedra in green.

Table 3.6: Refined lattice parameters of Ba₂MoO₅

| Space group Pnma (62), $\alpha = \beta = \gamma = 90^\circ$ | |
|---|-------------------|
| Lattice parameter | Refined value [Å] |
| a | 7.4105(4) |
| b | 5.7615(3) |
| c | 11.3843(6) |

Table 3.7: Refined atomic positions of Ba₂MoO₅

| Label | Element | Wyck. | x | y | z | B |
|-------|---------|-------|-----------|----------|------------|---------|
| Ba1 | Ba | 4c | 0.6853(2) | 1/4 | 0.0833(1) | 0.29(4) |
| Ba2 | Ba | 4c | 0.9802(1) | 1/4 | 0.78952(9) | 0.28(4) |
| Mo | Mo | 4c | 0.6833(3) | 1/4 | 0.4315(2) | 0.42(5) |
| O1 | O | 4a | 0 | 0 | 0 | 2.3(3) |
| O2 | O | 4c | 0.538(1) | 1/4 | 0.2953(8) | 0.8(3) |
| O3 | O | 4c | 0.778(1) | 1/4 | 0.594(1) | 3/5 |
| O4 | O | 8d | 0.318(1) | 0.008(1) | 0.1122(6) | 3/5 |

3.1.1.4 Ba₃MoO₆

The synthesis of this compound has not been tried before, although Maikel Rutten [111] suggested one cycle at 1473K for 4h under oxygen flow in his thesis. Considering the success of the Ba₂MoO₅ synthesis, two methods were attempted with two cycles at 1273K for 12h under O₂ flow. Synthesis conditions for both methods are included in table 3.1.

Method 1: Partially successful



BaMoO₄ and BaO were mixed in a 1:2 ratio and ground for 15 minutes with a mortar and pestle. The mixture (300 mg) was put into a large aluminium oxide crucible and heated under O₂ for 12h at 1273K. When it came out of the oven, the powder had a yellow/brown colour (figure 3.9). It also contained some hard black spots, which appeared to be a contamination. They were removed as much as possible before grinding.

Figure 3.9: Picture of aluminium oxide crucible with Ba₃MoO₆ after the first cycle in the oven

Phase analysis was done using Powdercell, but it was not possible to match one or multiple phase(s) to the unidentified peaks. It would be logical to have unreacted BaMoO₄ and/or BaO present, but that was not the case. Powdercell showed some possible BaMo₃O₁₀ in the mixture, but it only matched some of the missing peaks. The following compounds were tested: BaMoO₄, BaO, BaMo₃O₁₀, Ba₂MoO₅, Al₂(MoO₄)₃, Al₂O₃ (because of the Al₂O₃ crucible), MoO₂ and MoO₃.

A second cycle was done to see if the amount of unidentified peaks would decrease to make a Rietveld refinement possible. The mixture was heated at 1273K for 12h under an O₂ atmosphere. The colour of the powder was a little darker than after the first cycle as can be seen below (figure 3.10).

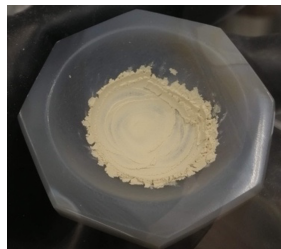


Figure 3.10: Picture of mortar with Ba₃MoO₆ after the second cycle in the oven

There were still too many unidentified peaks for a regular Rietveld refinement. Therefore, a Le Bail fit was tried with Ba₃MoO₆ and multiple different phases (Ba₂MoO₅, BaMo₃O₁₀, BaMoO₄ and/ or BaO). Lattice parameters and atomic positions for Ba₃MoO₆ were taken from Pearson's crystal database and published by Sabatier et al. [103]. This type of refinement uses a constant scale factor and does not optimise atomic positions. As a result, the programme identifies the presence of an extra phase, but does not specify how much of it is included in the mixture. This is because the intensity of the peaks is no longer refined (which gives the percentage of each phase during a regular refinement), only their position. The Le Bail refinement showed that the sample contained (an unknown amount) of Ba₂MoO₅ and BaMo₃O₁₀ (figure 3.11). Since this synthesis method was only partially successful, a second method was tried using different starting reagents Ba₂MoO₅ and BaO.

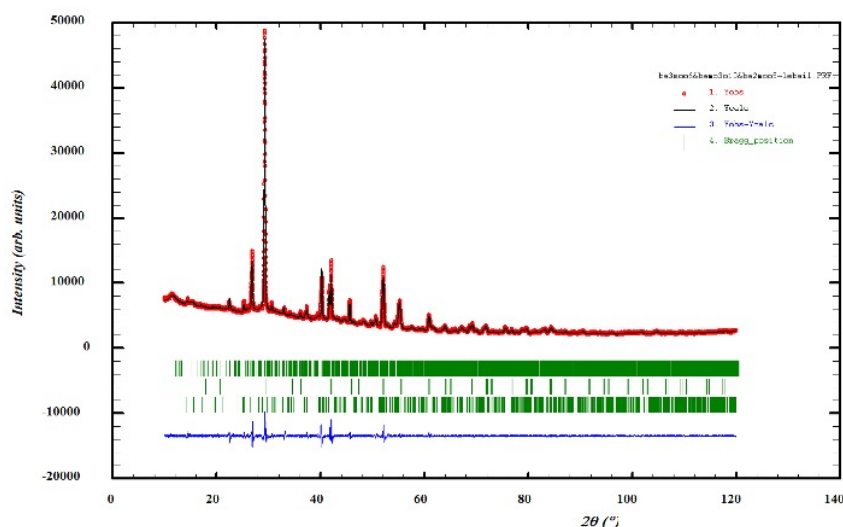


Figure 3.11: Le Bail refinement of Ba₃MoO₆ after two cycles with Ba₃MoO₆, Ba₂MoO₅ and BaMo₃O₁₀ ($\chi^2 = 4.36$). Comparison between the observed (Y_{obs} , in red) and calculated (Y_{calc} , in black) X-ray diffraction patterns. $Y_{obs} - Y_{calc}$, in blue, is the difference between the experimental and calculated intensities. The Bragg's reflection angular positions are marked in green for each phase.

Method 2: Partially successful



Ba_2MoO_5 and BaO were mixed in a 1:1 ratio and were ground for 15 minutes with a mortar and pestle. The mixture (150 mg) was added to a large aluminium oxide crucible and heated under O_2 at 1273K for 12h. The colour of the powder (figure 3.12a) looked much the same as after the first cycle of the previous method. It also contained the same black contamination spots that were removed as much as possible. The powder was easily removable from the crucible.

A regular Rietveld refinement was attempted, but was not possible due to extra phases that were present in the sample. Therefore a second cycle was done (at 1273K for 12h under O_2) to see if the purity of the sample could be improved. The colour of the resulting powder did not seem to have changed (there were no black spots this time, figure 3.12b). However, the sample was very sticky and hard to remove from the crucible.

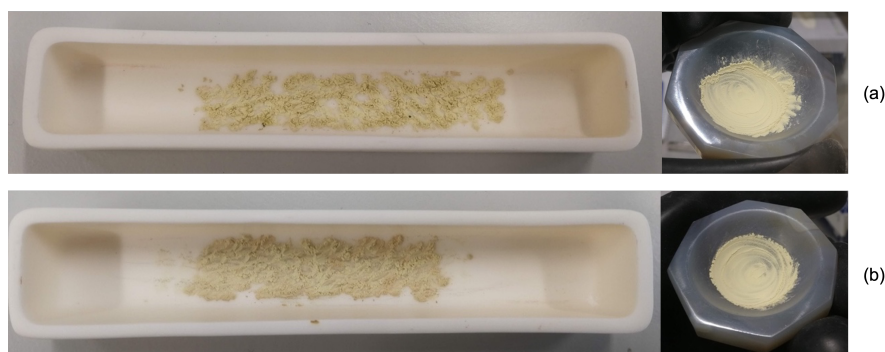


Figure 3.12: Picture of an aluminium oxide crucible with Ba_3MoO_6 after (a) the first cycle and (b) the second cycle in the oven

After this cycle, the regular Rietveld refinement was still not possible, too many unidentified phases were still present. When the XRD pattern of this sample was compared to the sample pattern from the first method, it showed that they were identical (figure 3.13). This is interesting considering that both methods used different sets of reagents. It is likely that Ba_3MoO_6 was formed with equal success by both reaction pathways, but that it decomposed during the synthesis into the same set and ratio of compounds, resulting in identical XRD patterns. Le Bail refinements showed the same results as for the first method, that the sample contained unknown amounts of Ba_2MoO_5 and $\text{BaMo}_3\text{O}_{10}$. The refinement is shown in figure 3.14 below.

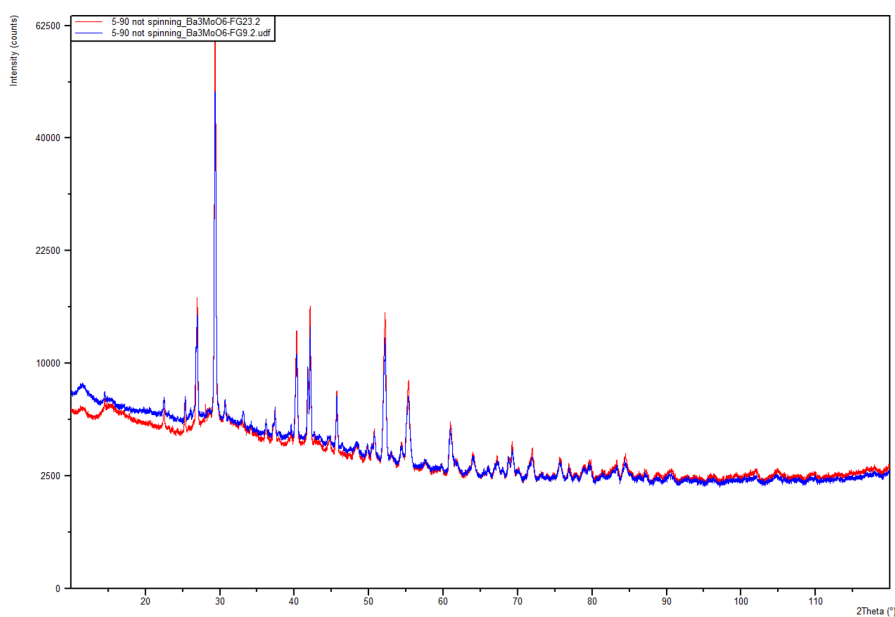


Figure 3.13: Comparison between the XRD patterns of both Ba_3MoO_6 synthesis methods. The first method in blue and the second method in red. Intensity [counts] on the y-axis and 2θ [°] on the x-axis.

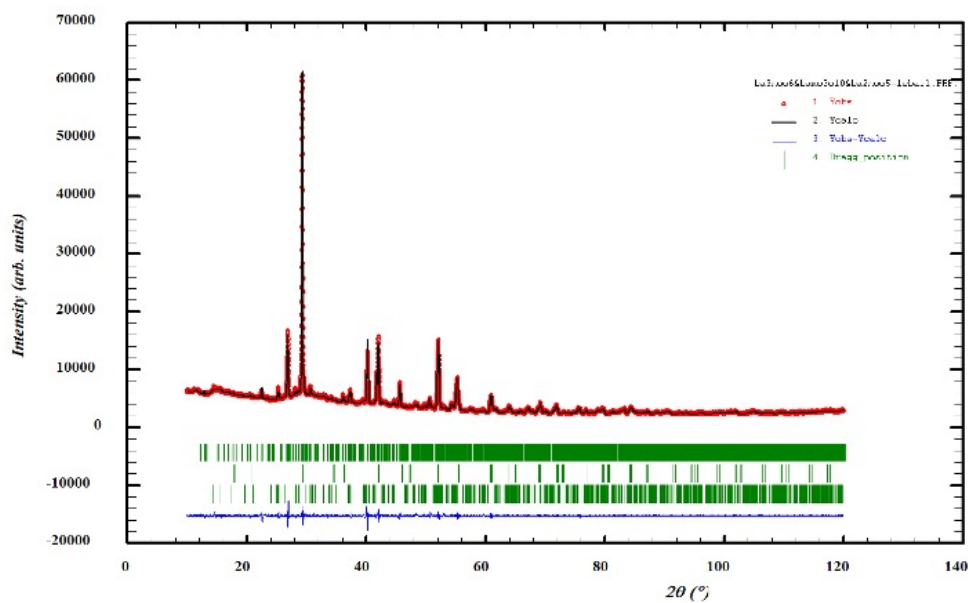


Figure 3.14: Le Bail refinement of Ba_3MoO_6 after two cycles with Ba_3MoO_6 , Ba_2MoO_5 and $\text{BaMo}_3\text{O}_{10}$ ($\chi^2 = 3.61$). Comparison between the observed (Y_{obs} , in red) and calculated (Y_{calc} , in black) X-ray diffraction patterns. $Y_{\text{obs}} - Y_{\text{calc}}$, in blue, is the difference between the experimental and calculated intensities. The Bragg's reflection angular positions are marked in green for each phase.

In order to synthesise a pure Ba₃MoO₆ sample, a method needs to be found to prevent its (probable) decomposition during the synthesis. It appears to be a similar problem to the first Ba₂MoO₅ synthesis method, where the Rietveld refinements showed the compound to decompose, giving a lower percentage of Ba₂MoO₅ after the second cycle than the first. When the synthesis temperature was decreased by 200 degrees, the decomposition stopped, resulting in a pure product.

The same approach is recommended for the synthesis of Ba₃MoO₆, despite the BaO – MoO₃ phase diagram indicating that Ba₃MoO₆ is stable at the current synthesis temperature (1273K). The synthesis temperature should be reduced to 1173 or 1073K with an XRD and Rietveld refinement after each cycle. Since the formation of Ba₃MoO₆ may take longer at a lower temperature, a third cycle might be necessary.

3.1.2 Thermodynamic property measurements on Ba-Mo-O compounds

3.1.2.1 Solution calorimetry measurements with Ba₂MoO₅

Now that Ba₂MoO₅ had been synthesised successfully, its thermodynamic properties could be investigated. There was only enough time to conduct a solution calorimetry experiment to determine its standard enthalpy of formation. The theory behind solution calorimetry is explained in chapter 2.4. All calorimetric data is reported in table 3.8. The following reaction scheme was followed (the concentration of HNO₃ was 2M):

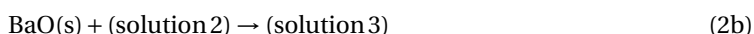
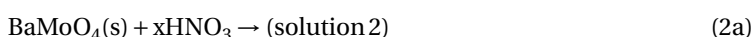
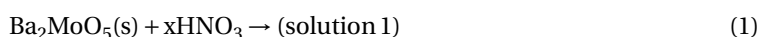


Table 3.8: Calorimetric data for the dissolution of Ba₂MoO₅, BaMoO₄ and BaO in 2 M HNO₃ at 298.15K

| No. | Sample mass m [mg] | Temperature change ΔT [mk] | Energy equivalent of the calorimeter Cp [J/K] | Temp. change associated with the dissolution Q [J] | Molar enthalpy of reaction Δ _r H ^o _m (298.15 K) [kJ/mol] |
|--------------------------------------|-----------------------|-------------------------------|--|---|--|
| Ba₂MoO₅ | | | | | |
| 1 | 30.34 ± 0.08 | 150.745 ± 0.30 | 111.297 ± 0.22 | -16.78 ± -0.05 | -249.18 ± -1.0 |
| 2 | 30.12 ± 0.08 | 142.348 ± 0.28 | 113.171 ± 0.23 | -16.11 ± -0.05 | -240.29 ± -0.48 |
| 3 | 30.20 ± 0.08 | 140.333 ± 0.28 | 112.942 ± 0.23 | -15.85 ± -0.05 | -236.49 ± -0.47 |
| 4 | 30.30 ± 0.08 | 145.669 ± 0.29 | 113.199 ± 0.23 | -16.49 ± -0.05 | -245.22 ± -0.49 |
| 5 | 30.27 ± 0.08 | 148.608 ± 0.30 | 111.812 ± 0.22 | -16.62 ± -0.05 | -247.35 ± -0.49 |
| BaMoO₄ | | | | | |
| 1 | 20.07 ± 0.40 | 14.528 ± 0.04 | 111.973 ± 0.34 | -1.63 ± -0.01 | -24.10 ± -0.10 |
| BaO | | | | | |
| 1 | 10.32 ± 0.03 | 168.692 ± 0.30 | 111.407 ± 0.20 | -18.79 ± -0.05 | -279.22 ± -0.56 |

The weights of dissolved materials were selected so that solution 1 and solution 3 had the same final concentration. The heat of formation of Ba₂MoO₅ was calculated using the thermodynamic cycle shown in table 3.9, as well as the known standard enthalpy of formations Δ_fH^o_m(298.15K, BaMoO₄) = -(1546.1 ± 1.7) kJ/mol [120] and Δ_fH^o_m(298.15K, BaO) = -(548.0 ± 2.0) kJ/mol [44].

The standard enthalpy of formation reaction (6) in table 3.9 was found by doing the calculation: (6) = (2a) + (2b) + (3) + (4) – (1). Due to time constraints, the solution calorimetry experiments with BaMoO₄

(2a.1) and BaO (2b.1) could only be done once, hence giving a result that is not statistically significant. It should be noted that a previously determined enthalpy of formation for BaMoO₄ by Smith et al. [123] and for BaO by Kauric et al. [65] both gave lower values of $-(34.37 \pm 0.34)$ kJ/mol (2a.2) and $-(284.19 \pm 0.17)$ kJ/mol (2b.2). Both values were measured in 2M HNO₃, just like the measurements from this work. Since those experiments were done multiple times, they are more reliable than the result from this thesis. These values and the enthalpy of formation that was calculated with them (6.2) are listed in grey in table 3.9.

Table 3.9: Thermodynamic cycle used to determine the standard heat of formation of Ba₂MoO₅

| Nr. | Reaction | $\Delta_r H_m^\circ(298.15\text{K})$ [kJ/mol] | Reference |
|--------|--|---|------------------------|
| (1) | Ba ₂ MoO ₅ (cr) + (sln) → Ba ₂ MoO ₅ (sln) | $-(243.71 \pm 10.46)$ | This work ^a |
| (2a.1) | BaMoO ₄ (cr) + (sln) → BaMoO ₄ (sln) | $-(24.10 \pm 0.10)$ | This work ^a |
| (2a.2) | | $-(34.37 \pm 0.34)$ | [123] |
| (2b.1) | BaO(cr) + BaMoO ₄ (sln) → BaO(sln) + BaMoO ₄ (sln) | $-(279.22 \pm 0.56)$ | This work ^a |
| (2b.2) | | $-(284.19 \pm 0.17)$ | [65] |
| (3) | Ba(cr) + Mo(cr) + 2O ₂ (g) → BaMoO ₄ (cr) | $-(1546.1 \pm 1.7)$ | [120] |
| (4) | Ba(cr) + ½O ₂ (g) → BaO(cr) | $-(548.0 \pm 2.0)^b$ | [44] |
| (6.1) | 2Ba(cr) + Mo(cr) + 2½O ₂ (g) → Ba ₂ MoO ₅ (cr) | $-(2153.71 \pm 14.82)$ | This work ^c |
| (6.2) | | $-(2168.95 \pm 14.67)$ | This work ^d |

^aValue calculated using the $\Delta_r H_m^\circ$ data in table 3.8

^bmeasured with 1M HCl instead of 2M HNO₃

^cCalculated with (2a.1) and (2b.1)

^dCalculated with (2a.2) and (2b.2)

Calculations give two results for the standard enthalpy of formation of Ba₂MoO₅. Using (2a.1) and (2b.1):

$$\Delta_f H_m^\circ(298.15\text{K}, \text{Ba}_2\text{MoO}_5) = -(2153.7 \pm 14.8)\text{kJ/mol} \quad (6.1)$$

and using (2a.2) and (2b.2):

$$\Delta_f H_m^\circ(298.15\text{K}, \text{Ba}_2\text{MoO}_5) = -(2169.0 \pm 14.7)\text{kJ/mol} \quad (6.2)$$

Considering that the previously calculated $\Delta_r H_m^\circ$ for BaMoO₄ and BaO are more reliable, (6.2) = $\Delta_f H_m^\circ(298.15\text{K}, \text{Ba}_2\text{MoO}_5) = -(2169.0 \pm 14.7)$ kJ/mol probably comes closest to the correct value. The solution calorimetry experiments with BaMoO₄ (2a) and BaO (2b) should be repeated in the future to obtain statistically relevant values. This will allow for the calculation of a reliable standard enthalpy of formation of Ba₂MoO₅.

3.1.3 Phase diagram investigations by DSC

The current BaO - MoO₃ phase diagram (as introduced in chapter 1.2) is shown in figure 3.15 below. The area of focus for this thesis is the region between ($0.5 \leq x \leq 1$), in an effort to confirm the position of the eutectic equilibrium (where BaMo₃O₁₀ + MoO₃ = liq.). Knowing the position of the eutectic equilibrium is very useful during modelling, because it provides guidance for the shape and position of the liquidus lines. Data points were obtained with TGDSC measurements of the relevant compositions. The methodology behind this measurement technique was explained in chapter 2.3.

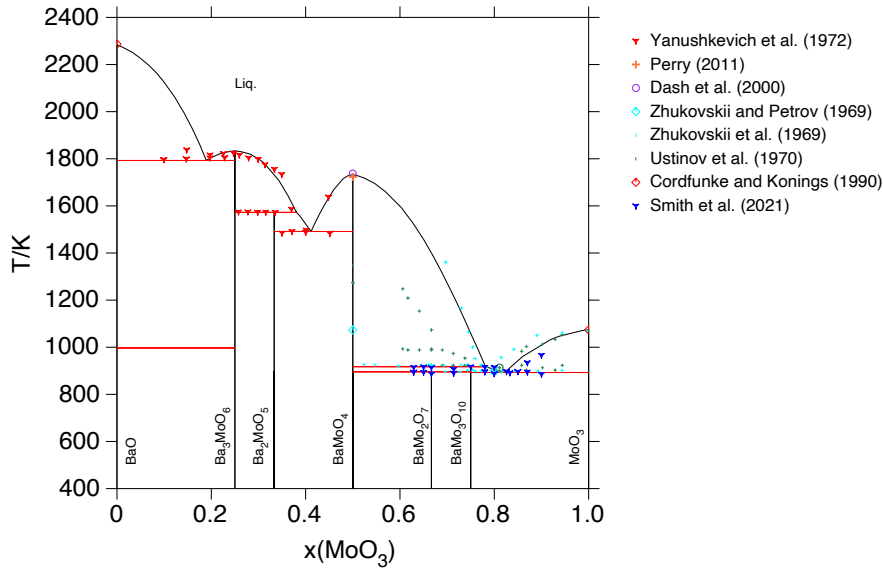


Figure 3.15: Current BaO - MoO₃ phase diagram. Data points by Yankuskevich et al. [130], Perry [98], Dash et al. [96], Zhukovskii et al. [137], Ustinov et al. [89], Cordfunke and Konings [38] and Smith et al. [120]

3.1.3.1 TGDSC Method

Synthesised compounds BaMoO₄ and BaMo₃O₁₀ as well as MoO₃ (Alfa Aesar, 99.99%) were mixed in different ratios to obtain a good range of compositions (BaMoO₄ : BaMo₃O₁₀ mixtures for 0.50 ≤ x ≤ 0.75 and BaMo₃O₁₀ : MoO₃ mixtures for 0.75 ≤ x ≤ 1.0) (table 3.10). BaMo₂O₇ was not used, because it has not yet been successfully synthesised. It is disputed whether this compound even exists in a stable form, since it could not be identified by XRD analysis during previous BaO - MoO₃ DSC measurements by Maikel Rutten [111]. BN powder was used for these measurements, because it was found that Al₂O₃ reacted with MoO₃ and resulted in the formation of Al₂(MoO₄)₃ upon melting.

Table 3.10: Molar ratios of the compounds used to mix the compositions that were measured

| x(MoO ₃) | Molar ratio | | |
|----------------------|--------------------|-----------------------------------|------------------|
| | BaMoO ₄ | BaMo ₃ O ₁₀ | MoO ₃ |
| 0.50 | 1 | | |
| 0.545 | 0.9 | 0.1 | |
| 0.60 | 0.75 | 0.25 | |
| 0.625 | 0.333 | 0.667 | |
| 0.667 | 0.5 | 0.5 | |
| 0.75 | | 1 | |
| 0.772 | | 0.72 | 0.28 |
| 0.792 | | 0.55 | 0.45 |
| 0.80 | | 0.5 | 0.5 |
| 0.82 | | 0.39 | 0.61 |
| 0.832 | | 0.34 | 0.66 |
| 0.845 | | 0.29 | 0.71 |

When the set temperature exceeded 1008K during TGDSC measurements, green crystallised powder was found on the outside of the crucible. This powder was most likely MoO_3 (which has the same shade of green), that evaporated and re-crystallised on the outside of the crucible. MoO_3 is quite volatile with a low melting point of 1068K, which probably caused a small amount of MoO_3 to evaporate. Because of this temperature limitation, it was impossible to detect the liquidus line outside of approximately $0.78 \leq x \leq 0.85$ during these measurements.

3.1.3.2 Results and outlying data point discussion

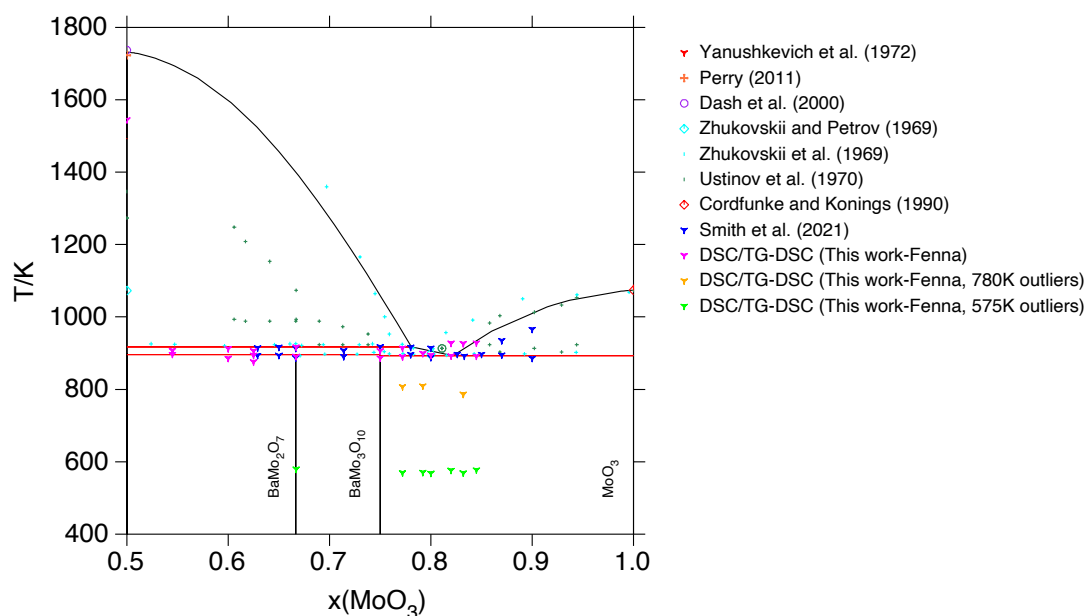


Figure 3.16: BaMoO_4 - MoO_3 phase diagram with all TGDSC results collected in this work (pink symbols), showing two sets of outlying peaks at $\pm 575\text{K}$ (in green) and $\pm 780\text{K}$ (in orange)

Figure 3.16 shows the BaMoO_4 - MoO_3 phase diagram with the collected TGDSC results. It is clear that not all data points follow the lines of the phase diagram model. These outlying peaks are discussed in the Appendix (C.1). In summary, it seems likely that the $\pm 575\text{K}$ and $\pm 780\text{K}$ data points are due to a contamination in BN and MoO_3 respectively. It is unclear why the $\pm 780\text{K}$ events were not detected during all $\text{BaMo}_3\text{O}_{10} : \text{MoO}_3$ TGDSC measurements, or why drying the BN powder made its outlying peaks more noticeable. It is recommended to buy new MoO_3 and BN and to test it with a DSC measurement. Because the current MoO_3 and BN powders have probably been used for some time, contamination from a dirty spatula or crucible is not inconceivable.

3.1.3.3 Measurement of the eutectic equilibrium in the region $0.5 \leq x(\text{MoO}_3) \leq 1.0$

Since probable causes for both outlying sets of data points have been determined, they can be removed from the final phase diagram. The result is shown in figure 3.17. Most results are in line with the model, especially the compositions including BaMoO_4 . However, some results within the area surrounding the eutectic equilibrium are not. Figure 3.18 shows a clearer picture.

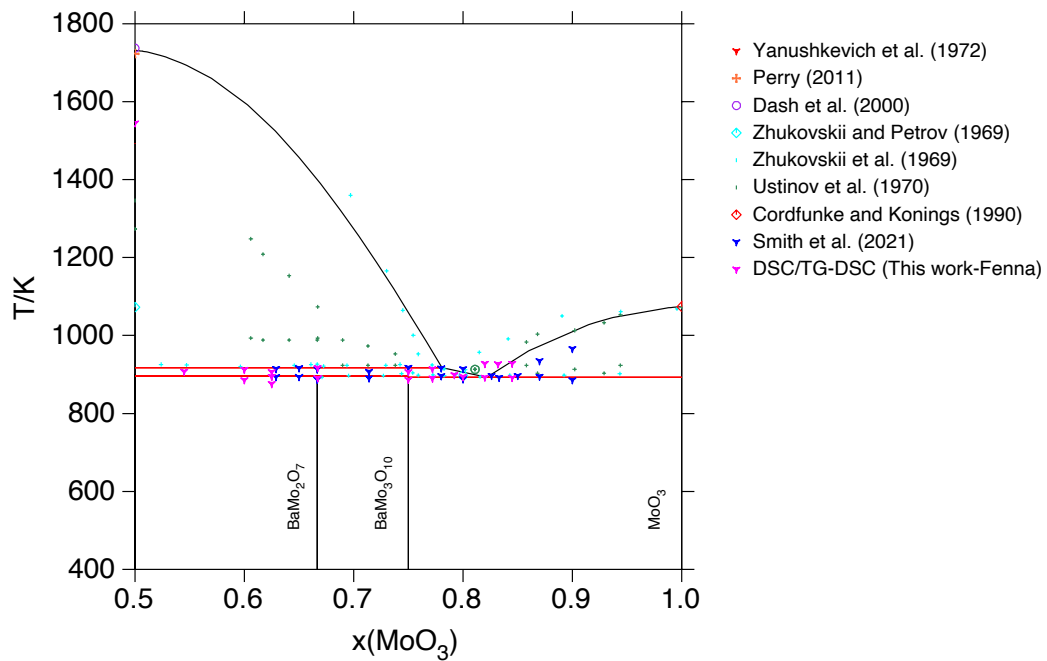


Figure 3.17: $(1-x)\text{BaMoO}_4 - (x)\text{MoO}_3$ phase diagram with final DSC results

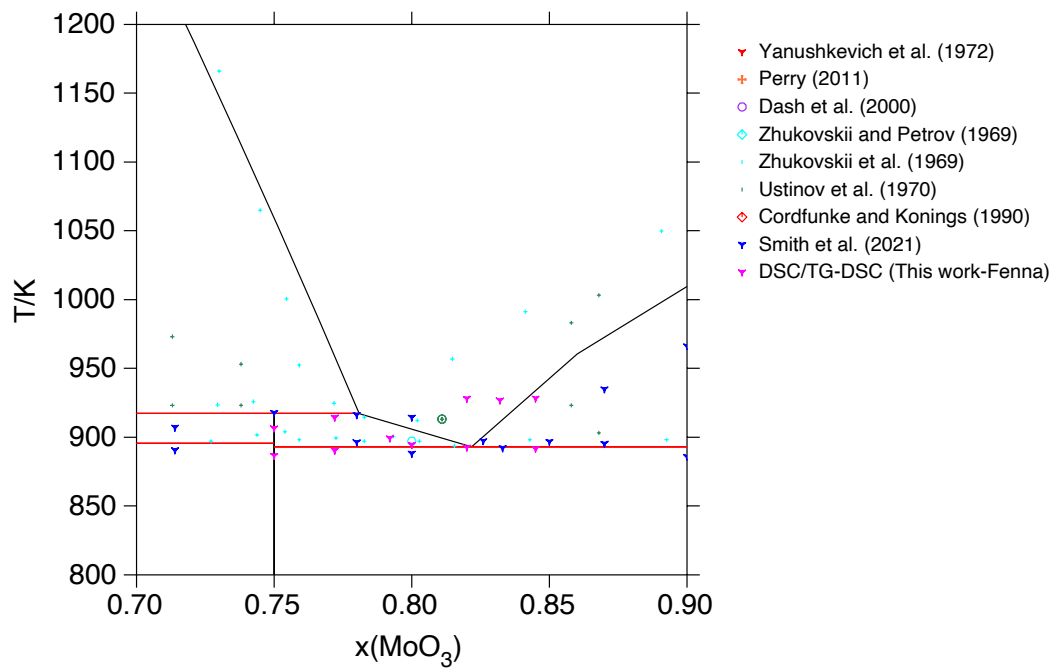


Figure 3.18: Zoomed section in the $\text{BaMoO}_4 - \text{MoO}_3$ phase diagram with obtained TGDSC results

The blue data points by Smith et al. [123] indicate that the eutectic equilibrium is located between $0.80 \leq x(\text{MoO}_3) \leq 0.85$. According to the data from this thesis, the eutectic point appears to be between $x(\text{MoO}_3) = 0.792$ and 0.80 , because both measurements only showed one thermal event. To see if this is the case, the TGDSC heating cycles of the $x(\text{MoO}_3) = 0.772, 0.792, 0.80, 0.82$ and 0.845 measurements will be analysed below.

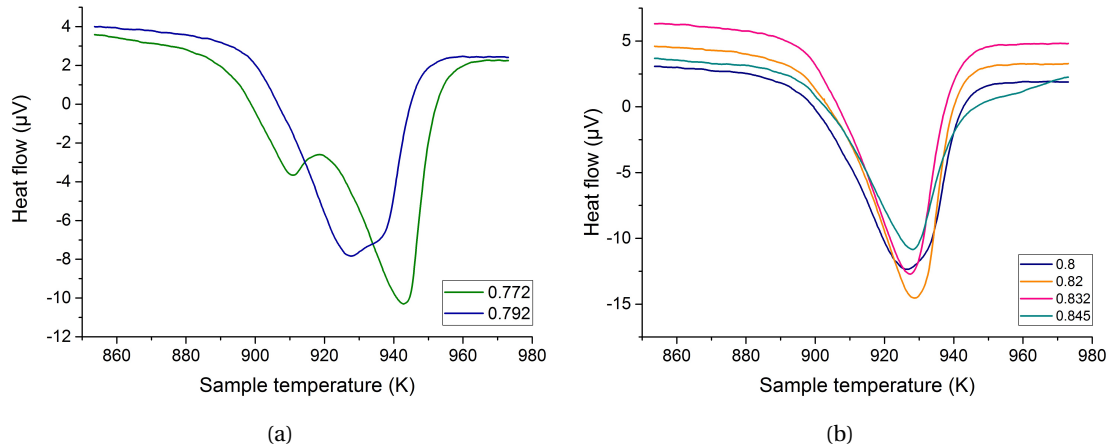


Figure 3.19: TGDSC heating cycle of (a) $x(\text{MoO}_3) = 0.772$ and 0.792 and (b) $x(\text{MoO}_3) = 0.80, 0.82, 0.832$ and 0.845 vs. the sample temperature [K]

Figure 3.19a depicts one heating cycle of the $x(\text{MoO}_3) = 0.772$ and 0.792 TGDSC measurements. The 0.772 measurement clearly shows two events that have slightly overlapping peaks. The first peak's onset temperature was used as the eutectic line data point, while the second peak's peak-max. temperature was taken as the liquidus line data point (the reason for this is explained in chapter 2.3). These peaks are perfectly in line with the current phase diagram model. The tip of the 0.792 peak clearly shows that two peaks that have overlapped. This indicates that the eutectic and liquidus lines are close together, implying that the eutectic equilibrium is close to this composition (because that would only show one solid peak). This would mean a divergence from the original eutectic equilibrium position at approximately $x(\text{MoO}_3) = 0.82$ according to the existing model.

Figure 3.19b shows one heating cycle of the $x(\text{MoO}_3) = 0.80, 0.82, 0.832$ and 0.845 TGSC measurements. The 0.80 measurement shows one solid peak. This could mean the discovery of the eutectic equilibrium, were it not for the $0.82, 0.832$ and 0.845 measurements, which demonstrate that these compositions also have only one peak in their heating cycle.

The $x(\text{MoO}_3) = 0.82$ cycle shows a small shoulder on the left side of the peak (it is difficult to see in the figure, but it is apparent during analysis). A shoulder represents a second overlapping peak, depicting two events that occur at very similar temperatures. The onset temperature of the shoulder was considered the eutectic event, whereas the peak max. of the large peak was considered the liquidus event. The $x(\text{MoO}_3) = 0.832$ measurement only showed one event, no shoulder could be detected. The peak max. temperature of the single heating event was taken to be the liquidus data point. The $x(\text{MoO}_3) = 0.845$ event is broader than the other events in figure 3.19b, especially on the right side. Technically this right shoulder would constitute the liquidus event and should be recorded with the peak max. temperature, however this temperature is impossible to detect because the shape of that peak is obscured. Therefore it was left out of the analysis. The onset temperature of the left shoulder

was considered the eutectic and the peak max. temperature was considered the liquidus event. When comparing the last three measurements in this figure, it seems that the presumed liquidus events of $x(\text{MoO}_3) = 0.82, 0.832$ and 0.845 all occur at approximately the same temperature (figure 3.20). This is unexpected and no satisfying explanation has been found as of yet.

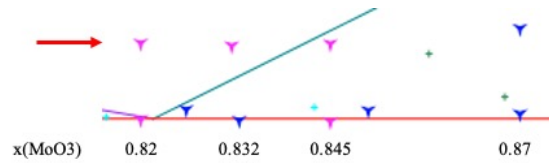


Figure 3.20: Comparing the temperature of the $x(\text{MoO}_3) = 0.82, 0.832, 0.845$ and 0.87 last events

Concluding from this analysis, the eutectic equilibrium in the $\text{BaMoO}_4 - \text{MoO}_3$ phase diagram is most likely in the range between $x(\text{MoO}_3) = 0.792$ and 0.80 . More measurements at higher values of $x(\text{MoO}_3)$ and at a higher temperature are needed to corroborate the position of the liquidus line in this area. More measurements also need to be done around $0.82 \leq x(\text{MoO}_3) \leq 0.845$ to determine how many events occur there and what they represent, preferably at a higher temperature than 1008K to ensure that the liquidus events are recorded. Measurements at a higher temperature could be done using an encased DSC crucible to prevent volatile MoO_3 from escaping. The collected TGDSC data is summarised in table 3.11 below.

Table 3.11: Equilibrium data collected by TGDSC of compositions $x(\text{MoO}_3)$ in the $\text{BaMoO}_4 - \text{MoO}_3$ pseudo-binary phase diagram. Outlying peaks shown in figure 3.16 are excluded. Post-XRD observed phases are in order of significance. (U.I. = unidentified impurities that could not be matched to the phases described below.)

| $x(\text{MoO}_3)$ | T_{eq} [K] | Equilibrium | Equilibrium reaction | Post-XRD |
|-------------------|---------------------|-------------|--|---|
| 0.545 | 896.76 ± 10 | Peritectoid | $\text{BaMoO}_4 + \text{BaMo}_2\text{O}_7 \rightarrow \text{BaMo}_3\text{O}_{10} + \text{BaMoO}_4$ | $\text{BaMoO}_4, \text{BaMo}_3\text{O}_{10}$ |
| | 907.9 ± 10 | Peritectic | $\text{BaMoO}_4 + \text{BaMo}_3\text{O}_{10} \rightarrow \text{BaMoO}_4 + \text{liq.}^1$ | |
| 0.60 | 885.97 ± 10 | Peritectoid | $\text{BaMoO}_4 + \text{BaMo}_2\text{O}_7 \rightarrow \text{BaMo}_3\text{O}_{10} + \text{BaMoO}_4$ | $\text{BaMoO}_4, \text{BaMo}_3\text{O}_{10}$ |
| | 912.92 ± 10 | Peritectic | $\text{BaMoO}_4 + \text{BaMo}_3\text{O}_{10} \rightarrow \text{BaMoO}_4 + \text{liq.}^1$ | |
| 0.625 | 894.49 ± 10 | Peritectoid | $\text{BaMoO}_4 + \text{BaMo}_2\text{O}_7 \rightarrow \text{BaMo}_3\text{O}_{10} + \text{BaMoO}_4$ | $\text{BaMoO}_4, \text{BaMo}_3\text{O}_{10}$ |
| | 906.91 ± 10 | Peritectic | $\text{BaMoO}_4 + \text{BaMo}_3\text{O}_{10} \rightarrow \text{BaMoO}_4 + \text{liq.}^1$ | |
| 0.667 | 890.86 ± 10 | Peritectoid | $\text{BaMo}_2\text{O}_7 \rightarrow \text{BaMo}_3\text{O}_{10} + \text{BaMoO}_4$ | $\text{BaMoO}_4, \text{BaMo}_3\text{O}_{10}$ |
| | 917.62 ± 10 | Peritectic | $\text{BaMoO}_4 + \text{BaMo}_3\text{O}_{10} \rightarrow \text{BaMoO}_4 + \text{liq.}^1$ | |
| 0.75 | 886.72 ± 5 | Peritectoid | Unknown | $\text{BaMo}_3\text{O}_{10}, \text{BaMoO}_4, \text{MoO}_2$ |
| | 906.63 ± 5 | Peritectic | $\text{BaMo}_3\text{O}_{10} \rightarrow \text{BaMoO}_4 + \text{liq.}^1$ | |
| 0.772 | 890.58 ± 10 | Peritectoid | $\text{BaMo}_3\text{O}_{10} + \text{MoO}_3 \rightarrow \text{BaMo}_3\text{O}_{10} + \text{liq.}^2$ | $\text{BaMo}_3\text{O}_{10}, \text{MoO}_3$ |
| | 914.52 ± 10 | Peritectic | $\text{BaMo}_3\text{O}_{10} + \text{liq.} \rightarrow \text{BaMoO}_4 + \text{liq.}^1$ | |
| 0.792 | 899.49 ± 10 | Eutectic | $\text{BaMo}_3\text{O}_{10} + \text{MoO}_3 \rightarrow \text{liq.}^4$ | $\text{BaMo}_3\text{O}_{10}, \text{MoO}_3, \text{U.I.}^a$ |
| 0.80 | 894.65 ± 10 | Eutectic | $\text{BaMo}_3\text{O}_{10} + \text{MoO}_3 \rightarrow \text{liq.}^4$ | $\text{U.I.}^a, \text{BaMoO}_4, \text{BaMo}_3\text{O}_{10}$ |
| 0.82 | 892.72 ± 10 | Eutectic | $\text{BaMo}_3\text{O}_{10} + \text{MoO}_3 \rightarrow \text{MoO}_3 + \text{liq.}^3$ | $\text{MoO}_3, \text{BaMo}_3\text{O}_{10}$ |
| | 928.15 ± 10 | Liquidus | $\text{MoO}_3 + \text{liq.}^3 \rightarrow \text{liq.}^4$ | |
| 0.832 | 926.92 ± 10 | Liquidus | $\text{MoO}_3 + \text{liq.}^3 \rightarrow \text{liq.}^4$ | $\text{MoO}_3, \text{BaMo}_3\text{O}_{10}$ |
| 0.845 | 891.8 ± 10 | Eutectic | $\text{BaMo}_3\text{O}_{10} + \text{MoO}_3 \rightarrow \text{MoO}_3 + \text{liq.}^3$ | $\text{U.I.}^a, \text{MoO}_3, \text{BaMo}_3\text{O}_{10}$ |
| | 928.32 ± 10 | Liquidus | $\text{MoO}_3 + \text{liq.}^3 \rightarrow \text{liq.}^4$ | |

^aAll seem to contain the same phase. These do not fit: $\text{BaMoO}_4, \text{BaMoO}_3, \text{Al}_2(\text{MoO}_4)_3, \text{Al}_2\text{O}_3, \text{Ba}_2\text{MoO}_5, \text{Ba}_3\text{MoO}_6, \text{Ba}_3\text{Mo}_{10}\text{O}_{28}, \text{BaCs}_2(\text{MoO}_4)_2, \text{Cs}_2\text{MoO}_4, \text{BaMo}_4\text{O}_{10} \cdot 2\text{H}_2\text{O}, \text{Ba}, \text{BaO}, \text{Mo}, \text{Mo}_4\text{O}_{11}, \text{Mo}_8\text{O}_{23}, \text{Mo}_9\text{O}_{26}, \text{Mo}_{17}\text{O}_{47}$ and MoO_2 .

3.2 Ba-Cs-Mo-O system: investigation of the BaMoO₄ - Cs₂MoO₄ pseudo-binary section

Since the successful synthesis of BaCs₂(MoO₄)₂ by Nathan de Zoete [27], the BaMoO₄ - Cs₂MoO₄ pseudo-binary section can be further explored and modelled using the CALPHAD method. The replication of the BaCs₂(MoO₄)₂ synthesis will be discussed, as well as the TG/DTG measurement and modelling results of the (1-x)BaMoO₄ - (x)Cs₂MoO₄ phase diagram.

3.2.1 BaCs₂(MoO₄)₂ synthesis and structural characterisation



BaCs₂(MoO₄)₂ was successfully synthesised by means of the method described in table 3.1. It resulted in a white powder with a slight yellow hue (figure 3.21) that is stable in an Ar atmosphere. XRD and subsequent Rietveld analysis (figure 3.22) showed that the sample was pure. The refined lattice parameters and atomic positions are shown in table 3.12 and 3.13.



Figure 3.21: Picture of an aluminum oxide crucible with BaCs₂(MoO₄)₂ after the last cycle in the oven

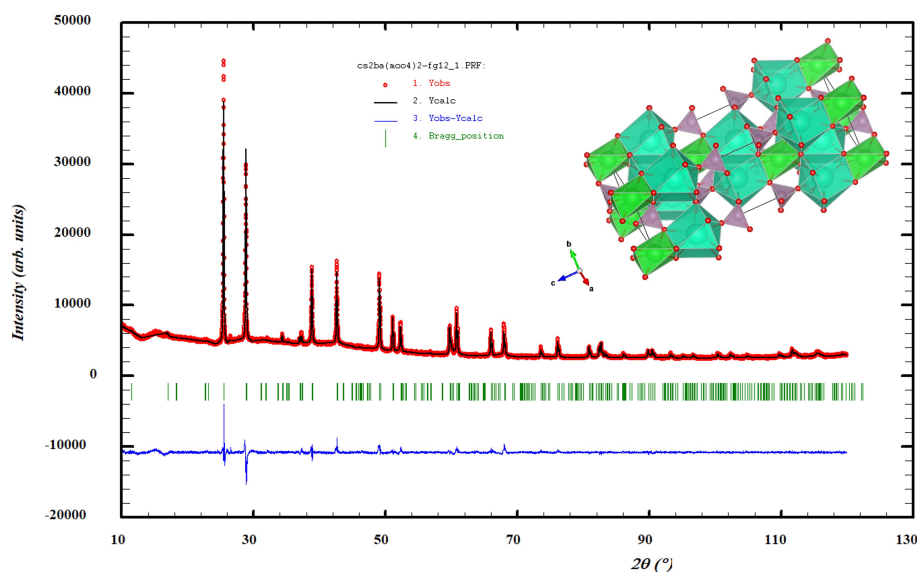


Figure 3.22: Rietveld refinement of BaCs₂(MoO₄)₂ ($\chi^2 = 4.77$). Comparison between the observed (Y_{obs} , in red) and calculated (Y_{calc} , in black) X-ray diffraction patterns. $Y_{\text{obs}} - Y_{\text{calc}}$, in blue, is the difference between the experimental and calculated intensities. The Bragg's reflection angular positions are marked in green. The BaCs₂(MoO₄)₂ unit cell sketch shows oxygen atoms in red, molybdenum polyhedra in purple, barium polyhedra in green and caesium polyhedra in turquoise.

Table 3.12: Refined lattice parameters of $\text{BaCs}_2(\text{MoO}_4)_2$

| Space group $R\bar{3}m$ (166), $\alpha = \beta = 90^\circ$, $\gamma = 120^\circ$ | |
|---|--------------------------------|
| Lattice parameter | Refined value [\AA] |
| a | 6.1842(2) |
| b | 6.1842(2) |
| c | 23.074(1) |

Table 3.13: Refined atomic positions of $\text{BaCs}_2(\text{MoO}_4)_2$

| Label | Element | Wyck. | x | y | z |
|-------|---------|-------|----------|----------|-----------|
| O1 | O | 18h | 0.498(8) | 0.502(8) | 0.250(4) |
| Cs | Cs | 6c | 0 | 0 | 0.2006(0) |
| O2 | O | 6c | 0 | 0 | 0.317(7) |
| Mo | Mo | 6c | 0 | 0 | 0.3979(0) |
| Ba | Ba | 3a | 0 | 0 | 0 |

3.2.2 Phase diagram investigations by DSC

The current BaMoO_4 - Cs_2MoO_4 phase diagram (as introduced in chapter 1.3) is shown in figure 3.23 below. To create a CALPHAD model of this sketch, experiments are needed with a wider range of compositions, specifically to confirm the position of the eutectic equilibrium. Knowing the position of the eutectic equilibrium is very useful during modelling, because it provides guidance for the shape and position of the liquidus lines. Measurements were done with by means of TG/DSC. The methodology behind this measurement technique was explained in chapter 2.3.

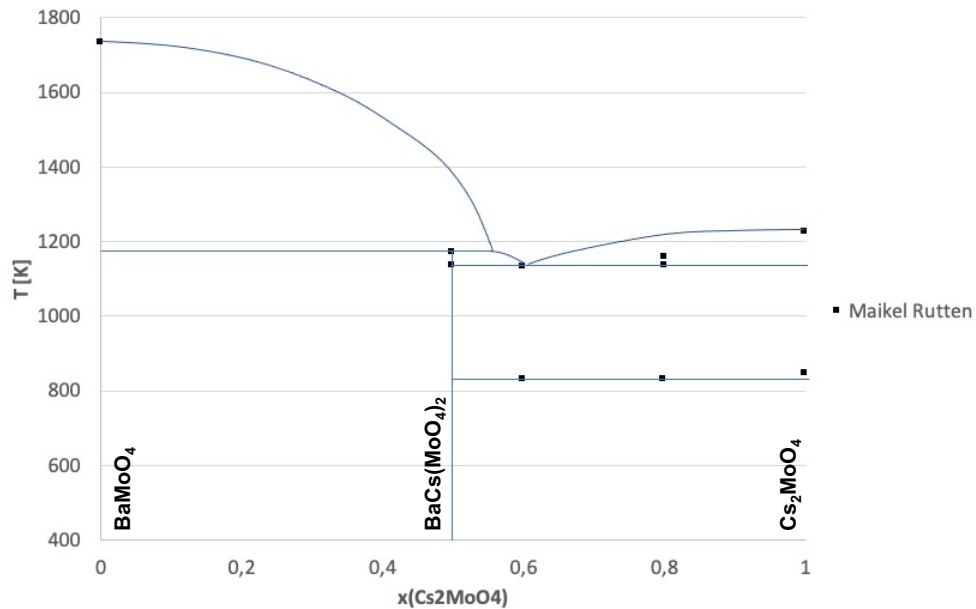


Figure 3.23: Original sketch of the $(1-x)\text{BaMoO}_4$ - $(x)\text{Cs}_2\text{MoO}_4$ phase diagram [111]. These experiments were only done with BaMoO_4 and Cs_2MoO_4 compositions, $\text{BaCs}_2(\text{MoO}_4)_2$ was not used.

Synthesised compounds BaMoO_4 , Cs_2MoO_4 and $\text{BaCs}_2(\text{MoO}_4)_2$ were mixed in different ratios to obtain a good range of compositions ($\text{BaMoO}_4 : \text{BaCs}_2(\text{MoO}_4)_2$ mixtures for $0 \leq x \leq 0.50$ and $\text{BaCs}_2(\text{MoO}_4)_2 : \text{Cs}_2\text{MoO}_4$ mixtures for $0.50 \leq x \leq 1.0$) (table 3.14). Al_2O_3 powder was used to avoid a reaction between the sample and the crucible upon melting. All of the collected data can be found in table 3.15.

Table 3.14: Molar ratios of the compounds used to mix the compositions that were measured

| $x(\text{Cs}_2\text{MoO}_4)$ | Molar ratio | | |
|------------------------------|------------------|---------------------------------|---------------------------|
| | BaMoO_4 | $\text{BaCs}_2(\text{MoO}_4)_2$ | Cs_2MoO_4 |
| 0.333 | 0.5 | 0.5 | |
| 0.50 | | 1 | |
| 0.562 | | 0.78 | 0.22 |
| 0.623 | | 0.605 | 0.395 |
| 0.699 | | 0.43 | 0.57 |
| 0.752 | | 0.33 | 0.67 |
| 0.80 | | 0.25 | 0.75 |
| 0.851 | | 0.175 | 0.825 |
| 0.889 | | 0.125 | 0.875 |
| 0.909 | | 0.1 | 0.9 |
| 0.930 | | 0.075 | 0.925 |
| 0.952 | | 0.05 | 0.95 |
| 0.976 | | 0.025 | 0.975 |
| 1.0 | | | 1 |

3.2.2.1 Decomposition of $\text{BaCs}_2(\text{MoO}_4)_2$ during TGDSC measurements

The first two measurements with $x(\text{Cs}_2\text{MoO}_4) = 0.333$ and 0.50 compositions were done for 4 cycles at a heating rate of $10\text{K}/\text{min}$ and cooling rates of $20, 10, 8$ and $5\text{K}/\text{min}$. The results are shown in figure 3.24 below.

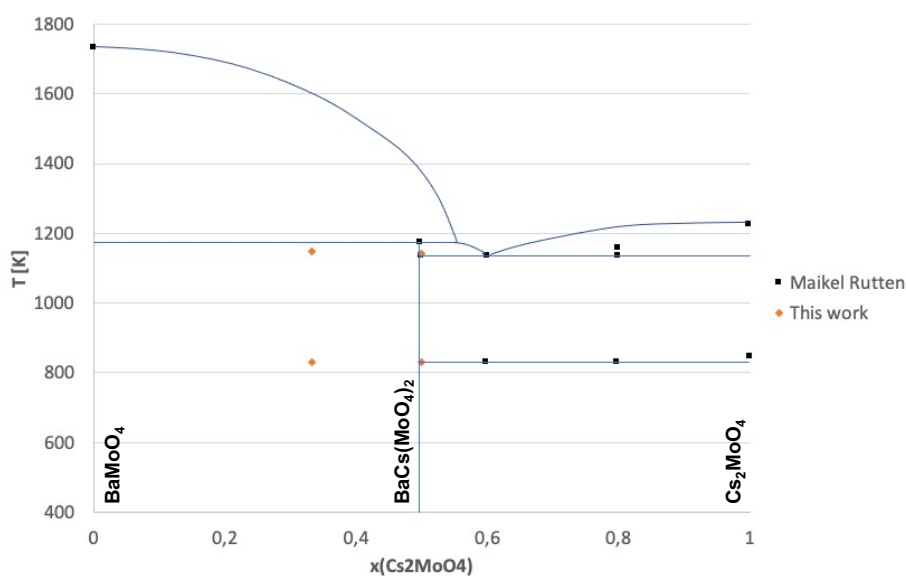


Figure 3.24: First two TGDSC measurements (orange) at $x(\text{Cs}_2\text{MoO}_4) = 0.333$ and 0.50

Both second events occur at approximately the expected temperature, but the first events are unexpected and perfectly coincide with the polymorphic transition temperature of $\alpha\text{Cs}_2\text{MoO}_4 \rightarrow \beta\text{Cs}_2\text{MoO}_4$ in $0.5 \leq x \leq 1$. Considering that these first events only occur after the first TGDSC cycle, it is likely that $\text{BaCs}_2(\text{MoO}_4)_2$ dissociates during the heating cycle and does not have enough time to fully combine during the cooling cycle that follows. This is unsurprising considering the lengthy reaction time of the $\text{BaCs}_2(\text{MoO}_4)_2$ synthesis (62h). The first event during the 2nd, 3rd and 4th heating cycles is then created by the crystal phase transition of the Cs_2MoO_4 that is present in the sample due to the dissociation of $\text{BaCs}_2(\text{MoO}_4)_2$. This hypothesis was confirmed by analysis of the XRD patterns of these samples, showing BaMoO_4 , Cs_2MoO_4 and only a small amount of $\text{BaCs}_2(\text{MoO}_4)_2$ (table 3.15).

Since only the first cycle gives reliable results, it was decided to perform only 1 cycle measurements for the compositions in this phase diagram. Although the results would not be statistically significant, they would provide a preliminary outline of the $(1-x)\text{BaMoO}_4 - (x)\text{Cs}_2\text{MoO}_4$ phase diagram that could be modelled in ThermoCalc using the CALPHAD method. In the future, complementary experiments are needed to elaborate on these preliminary results, either by performing 4 cycle measurements with very slow cooling rates or with four 1 cycle measurements to provide statistically significant data.

3.2.2.2 Outlying data point discussion

After the first half of the measurements were completed, a CALPHAD model was made based on the results. In contrast to Maikel Rutten [111], who assumed a eutectic point at $x(\text{Cs}_2\text{MoO}_4) = 0.6$, this model placed the eutectic point in the area $0.85 \leq x(\text{Cs}_2\text{MoO}_4) \leq 0.95$. Based on this new information, the second half of the measurements were done in that area to determine the location of the eutectic equilibrium. Results of both the first and second sets of measurements can be seen in figure 3.25. The optimisation of this model will be addressed later. The green symbols show outlying data points that are discussed in the Appendix (C.2).

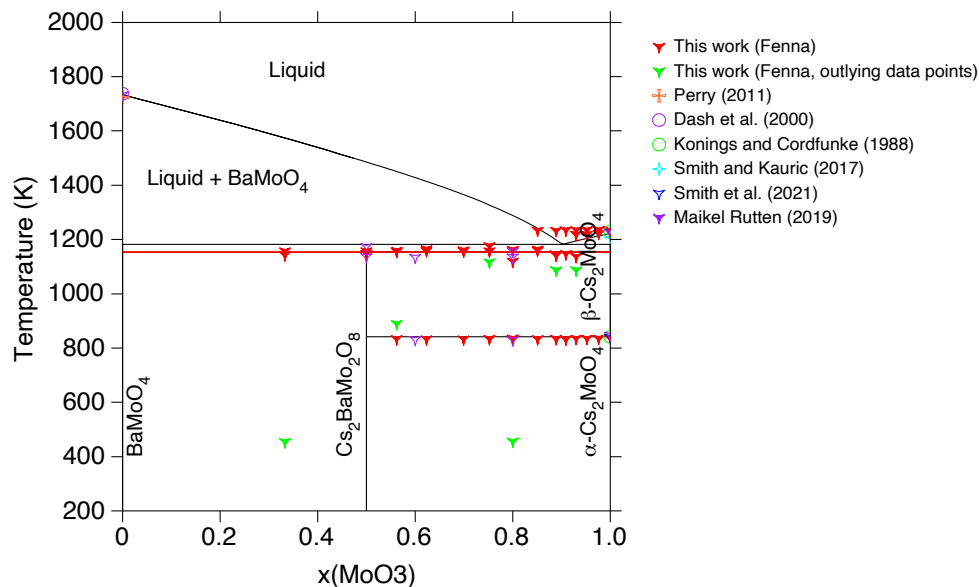


Figure 3.25: Initial CALPHAD model with all TGDSC results and outlying data points in green. Data points by Perry [98], Dash et al. [26], Konings and Cordfunke [38] and Smith and Kauric [118], Smith et al. [121] and M. Rutten [111]

The conclusion of this discussion is that the $\pm 455\text{K}$ peaks are quite clearly caused by water contained in the Al_2O_3 powder, since they disappear after the powder was dried. The remaining outlying peaks might have occurred due to a combination of some of the observations listed in the Appendix, namely that first cycle measurements are often unusual and are normally not included in the final data analysis, that there are inconsistent TGDSC patterns for repeated measurements with the same composition and that weight loss was detected for some compositions with a higher amount of Cs_2MoO_4 (possibly due to the melting of Cs_2MoO_4). Traces of Cs_2O were found in the samples after XRD analysis, but this amount was considered too small to have an impact on the TGDSC measurements. Multiple 1-cycle measurements of the same compositions could provide clarity and statistically significant data, possibly with a capped DSC crucible to prevent some of the weight loss at higher $x(\text{Cs}_2\text{MoO}_4)$ values. It is strongly recommended to find a method to achieve a 4 cycle measurement, because this would eliminate first cycle noise and would give statistically significant results.

3.2.2.3 Measurement of the eutectic equilibrium

The discussion on weight loss due to the melting of Cs_2MoO_4 is also relevant for the determination of the eutectic equilibrium. As was said above, the initial model of the $\text{BaMoO}_4 - \text{Cs}_2\text{MoO}_4$ phase diagram in figure 3.25 considers the eutectic equilibrium to be in the area $0.85 \leq x \leq 0.95$. This area is quite complex to investigate since the eutectic and liquidus lines are very close to each other and close to the melting temperature of Cs_2MoO_4 . The thermal events of a TGDSC measurement in this area will most likely overlap, making it extremely challenging to determine the temperature at which individual events occur.

Evaluating the data points in this area does not reveal a clear eutectic equilibrium. From $x = 0.852$ onward, all last events occur at approximately the same temperature, creating a straight line where a liquidus line would be expected (figure 3.26). Analysis of these TGDSC measurements shows that their last events overlap with the melting peak of pure Cs_2MoO_4 (figure 3.27 shows an example with $x(\text{MoO}_3) = 0.976$). In that case, the last events of $x(\text{Cs}_2\text{MoO}_4) = 0.909, 0.952$ and 0.976 could be disregarded, meaning that these measurements are only left with one event, which could technically represent the eutectic equilibrium.

Because of the expected overlapping liquidus, eutectic and Cs_2MoO_4 melting peaks in this area, it is impossible to tell which of these three compositions comes closest to the eutectic point position. It can probably be concluded however, that it is located somewhere in the area $0.909 \leq x \leq 0.976$.

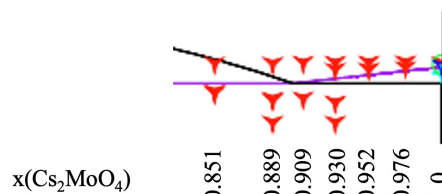


Figure 3.26: Enlarged section of the phase diagram in the $0.851 \leq x(\text{Cs}_2\text{MoO}_4) \leq 1.0$ region

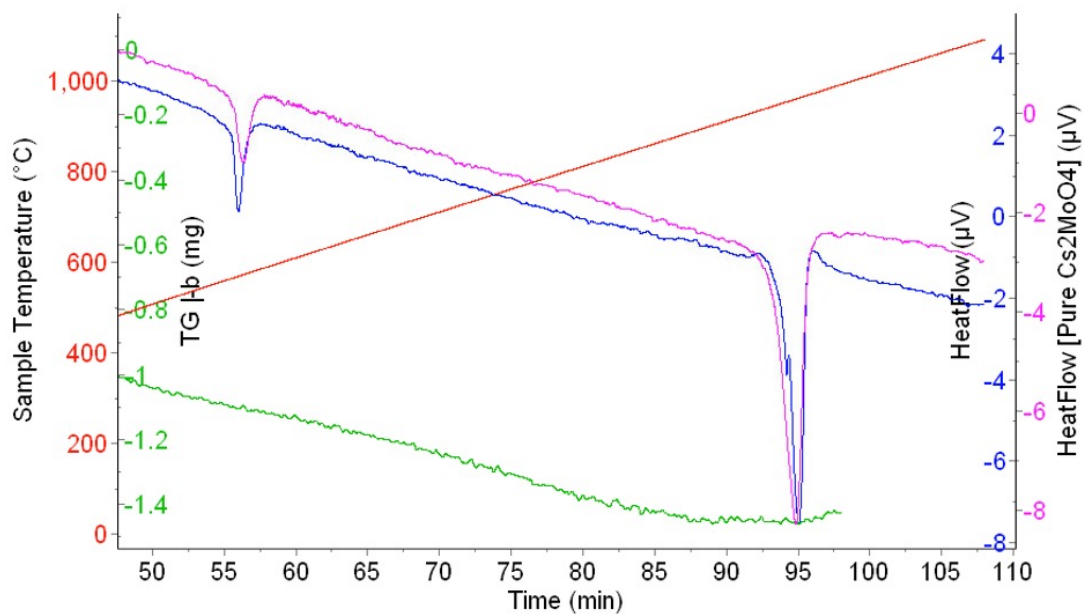


Figure 3.27: Comparison between the collected TGDSC data for pure Cs_2MoO_4 (in purple) and the $x(\text{Cs}_2\text{MoO}_4) = 0.976$ composition (in blue). Change in sample weight in green and the sample temperature in red.

Table 3.15: Equilibrium data collected by TGDSC of compositions $x(\text{Cs}_2\text{MoO}_4)$ in the $\text{BaMoO}_4 - \text{Cs}_2\text{MoO}_4$ pseudo-binary phase diagram. The $\pm 455\text{K}$ outlying peaks shown in figure 3.25 are excluded. Post-XRD observed phases are in order of significance.

| $x(\text{Cs}_2\text{MoO}_4)$ | T_{eq} [K] | Equilibrium | Equilibrium reaction | Post-XRD |
|------------------------------|---------------------|-----------------------|--|---|
| 0.333 | 1143.11 ± 10 | Peritectoid | $\text{BaCs}_2(\text{MoO}_4)_2 \rightarrow \beta\text{Cs}_2\text{MoO}_4 + \text{BaMoO}_4$ | $\text{BaMoO}_4, \text{Cs}_2\text{MoO}_4$ |
| | 1156.95 ± 10 | Eutectic | $\beta\text{Cs}_2\text{MoO}_4 + \text{BaMoO}_4 \rightarrow \text{liq.}^1$ | |
| 0.50 | 1148.73 ± 5 | Peritectoid | $\text{BaCs}_2(\text{MoO}_4)_2 \rightarrow \beta\text{Cs}_2\text{MoO}_4 + \text{BaMoO}_4$ | $\text{BaCs}_2(\text{MoO}_4)_2,$ $\text{BaMoO}_4, \text{Cs}_2\text{MoO}_4$ |
| | 1157.79 ± 5 | Eutectic | $\beta\text{Cs}_2\text{MoO}_4 + \text{BaMoO}_4 \rightarrow \text{liq.}^1$ | |
| 0.562 | 833.63 ± 10 | Polymorphism | $\alpha\text{Cs}_2\text{MoO}_4 \rightarrow \beta\text{Cs}_2\text{MoO}_4$ | $\text{BaMoO}_4, \text{Cs}_2\text{MoO}_4,$ $\text{BaCs}_2(\text{MoO}_4)_2$ |
| | 889.42 ± 10 | Unknown | Unknown | |
| | 1155.35 ± 10 | Peritectoid | $\text{BaCs}_2(\text{MoO}_4)_2 \rightarrow \beta\text{Cs}_2\text{MoO}_4 + \text{BaMoO}_4$ | |
| | 1158.97 ± 10 | Eutectic | $\beta\text{Cs}_2\text{MoO}_4 + \text{BaMoO}_4 \rightarrow \text{liq.}^1$ | |
| 0.623 | 833.13 ± 10 | Polymorphism | $\alpha\text{Cs}_2\text{MoO}_4 \rightarrow \beta\text{Cs}_2\text{MoO}_4$ | $\text{BaMoO}_4, \text{Cs}_2\text{MoO}_4,$ $\text{BaCs}_2(\text{MoO}_4)_2$ |
| | 1158.16 ± 10 | Peritectoid | $\beta\text{Cs}_2\text{MoO}_4 + \text{BaCs}_2(\text{MoO}_4)_2 \rightarrow \beta\text{Cs}_2\text{MoO}_4 + \text{BaMoO}_4$ | |
| | 1164.57 ± 10 | Eutectic | $\beta\text{Cs}_2\text{MoO}_4 + \text{BaMoO}_4 \rightarrow \text{BaMoO}_4 + \text{liq.}^1$ | |
| 0.699 | 832.72 ± 10 | Polymorphism | $\alpha\text{Cs}_2\text{MoO}_4 \rightarrow \beta\text{Cs}_2\text{MoO}_4$ | $\text{BaMoO}_4, \text{Cs}_2\text{MoO}_4,$ Cs_2O |
| | 1157.03 ± 10 | Peritectoid | $\text{BaCs}_2(\text{MoO}_4)_2 \rightarrow \beta\text{Cs}_2\text{MoO}_4 + \text{BaMoO}_4$ | |
| | 1160.72 ± 10 | Eutectic | $\beta\text{Cs}_2\text{MoO}_4 + \text{BaMoO}_4 \rightarrow \text{liq.}^1$ | |
| 0.752 | 833.97 ± 10 | Polymorphism | $\alpha\text{Cs}_2\text{MoO}_4 \rightarrow \beta\text{Cs}_2\text{MoO}_4$ | $\text{Cs}_2\text{MoO}_4,$ $\text{BaCs}_2(\text{MoO}_4)_2,$ BaMoO_4 |
| | 1116.17 ± 10 | Unknown | Unknown | |
| | 1156.66 ± 10 | Peritectoid | $\text{BaCs}_2(\text{MoO}_4)_2 \rightarrow \beta\text{Cs}_2\text{MoO}_4 + \text{BaMoO}_4$ | |
| | 1162.06 ± 10 | Eutectic | $\beta\text{Cs}_2\text{MoO}_4 + \text{BaMoO}_4 \rightarrow \text{liq.}^1$ | |
| 0.80 | 835.16 ± 10 | Polymorphism | $\alpha\text{Cs}_2\text{MoO}_4 \rightarrow \beta\text{Cs}_2\text{MoO}_4$ | $\text{Cs}_2\text{MoO}_4, \text{BaMoO}_4,$ Cs_2O |
| | 1119.22 ± 10 | Peritectoid | $\text{BaCs}_2(\text{MoO}_4)_2 \rightarrow \beta\text{Cs}_2\text{MoO}_4 + \text{BaMoO}_4$ | |
| | 1162.24 ± 10 | Eutectic | $\beta\text{Cs}_2\text{MoO}_4 + \text{BaMoO}_4 \rightarrow \text{liq.}^1$ | |
| 0.851 | 833.16 ± 10 | Polymorphism | $\alpha\text{Cs}_2\text{MoO}_4 \rightarrow \beta\text{Cs}_2\text{MoO}_4$ | $\text{Cs}_2\text{MoO}_4, \text{BaMoO}_4,$ $\text{Cs}_2\text{O}, \text{BaCs}_2(\text{MoO}_4)_2$ |
| | 1160.11 ± 10 | Peritectoid | $\text{BaCs}_2(\text{MoO}_4)_2 \rightarrow \beta\text{Cs}_2\text{MoO}_4 + \text{BaMoO}_4$ | |
| | 1163.41 ± 10 | Eutectic | $\beta\text{Cs}_2\text{MoO}_4 + \text{BaMoO}_4 \rightarrow \text{liq.}^1$ | |
| | 1233.01 ± 10 | Liquidus ^b | $\text{BaMoO}_4 + \text{liq} \rightarrow \text{liq.}^3$ | |
| 0.889 | 833.99 ± 10 | Polymorphism | $\alpha\text{Cs}_2\text{MoO}_4 \rightarrow \beta\text{Cs}_2\text{MoO}_4$ | $\text{BaMoO}_4,$ $\text{BaCs}_2(\text{MoO}_4)_2,$ $\text{Cs}_2\text{O}, \text{Cs}_2\text{MoO}_4$ |
| | 1087.16 ± 10 | Unknown | Unknown | |
| | 1142.19 ± 10 | Peritectoid | $\text{BaCs}_2(\text{MoO}_4)_2 \rightarrow \beta\text{Cs}_2\text{MoO}_4 + \text{BaMoO}_4$ | |
| | 1145.49 ± 10 | Eutectic | $\beta\text{Cs}_2\text{MoO}_4 + \text{BaMoO}_4 \rightarrow \text{liq.}^1$ | |
| 0.909 | 1232.38 ± 10 | Liquidus ^b | $\text{BaMoO}_4 + \text{liq} \rightarrow \text{liq.}^3$ | |
| | 832.76 ± 10 | Polymorphism | $\alpha\text{Cs}_2\text{MoO}_4 \rightarrow \beta\text{Cs}_2\text{MoO}_4$ | $\text{Cs}_2\text{MoO}_4,$ $\text{BaCs}_2(\text{MoO}_4)_2, \text{Cs}_2\text{O}$ |
| | 1144.76 ± 10 | Eutectic | $\beta\text{Cs}_2\text{MoO}_4 + \text{BaMoO}_4 \rightarrow \text{liq.}^3$ | |
| | 1234.77 ± 10 | Liquidus ^b | $\beta\text{Cs}_2\text{MoO}_4 + \text{liq} \rightarrow \text{liq.}^3$ | |
| 0.930 | 834.89 ± 10 | Polymorphism | $\alpha\text{Cs}_2\text{MoO}_4 \rightarrow \beta\text{Cs}_2\text{MoO}_4$ | |
| | 1086.96 ± 10 | Unknown | Unknown | |
| | 1136.73 ± 10 | Peritectoid | $\text{BaCs}_2(\text{MoO}_4)_2 \rightarrow \beta\text{Cs}_2\text{MoO}_4 + \text{BaMoO}_4$ | |
| | 1217.95 ± 10 | Unknown | Unknown | |
| | 1234.79 ± 10 | Liquidus ^b | $\beta\text{Cs}_2\text{MoO}_4 + \text{liq} \rightarrow \text{liq.}^3$ | |
| 0.952 | 835.06 ± 10 | Polymorphism | $\alpha\text{Cs}_2\text{MoO}_4 \rightarrow \beta\text{Cs}_2\text{MoO}_4$ | $\text{Cs}_2\text{MoO}_4, \text{Cs}_2\text{O}$ |
| | 1218.35 ± 10 | Unknown | Unknown | |
| | 1235.14 ± 10 | Liquidus ^b | $\beta\text{Cs}_2\text{MoO}_4 + \text{liq} \rightarrow \text{liq.}^3$ | |
| 0.976 | 835.69 ± 10 | Polymorphism | $\alpha\text{Cs}_2\text{MoO}_4 \rightarrow \beta\text{Cs}_2\text{MoO}_4$ | Bad XRD ^d |
| | 1222.00 ± 10 | Unknown | Unknown | |
| | 1235.73 ± 10 | Liquidus ^b | $\beta\text{Cs}_2\text{MoO}_4 + \text{liq} \rightarrow \text{liq.}^3$ | |
| 1.0 | 836.01 ± 5 | Polymorphism | $\alpha\text{Cs}_2\text{MoO}_4 \rightarrow \beta\text{Cs}_2\text{MoO}_4$ | Cs_2MoO_4 |
| | 1233.46 ± 5 | Liquidus | $\beta\text{Cs}_2\text{MoO}_4 + \text{liq} \rightarrow \text{liq.}^3$ | |

^dThe XRD patterns of compositions $x(\text{MoO}_3) = 0.930$ and 0.976 showed very little definition, making it impossible to match individual peaks to compound XRD patterns in PowderCell. Unfortunately there was no time to redo the XRD measurements, but the DSC samples have been stored under Ar atmosphere if this information is required for future study.

^bUnclear, could also be congruent melting of $\beta\text{Cs}_2\text{MoO}_4$

3.2.3 BaMoO₄ - Cs₂MoO₄ CALPHAD Model

With the new TGDSC measurements on the BaMoO₄ - Cs₂MoO₄ system, a thermodynamic model of the pseudo-binary phase diagram was made and optimised using the CALPHAD method. The theory behind this method is explained in section 2.6.

3.2.3.1 CALPHAD model

Thermodynamic functions

For the solid phase, Gibbs energy functions of BaMoO₄, Cs₂MoO₄ and BaCs₂(MoO₄)₂ at temperature T and in their state ψ are written as follows:

$$G^\psi(T) - \sum_i n_i^\psi \circ H_i^{SER}(298.15K) = a + bT + cT \cdot \ln T + \sum d_n T^n \quad (3.8)$$

where n is an integer and i is a pure element. The 'a', 'b' and 'c' terms represent the enthalpy, entropy and heat capacity functions, respectively. The first two are optimised during modelling. The functions for BaMoO₄ and Cs₂MoO₄ were taken from two papers by Smith et al., [120] and [121], respectively, and are reported in table 3.18. The Gibbs energy function of BaCs₂(MoO₄)₂ (also in table 3.18) was based on the standard enthalpy of formation ($\Delta_f H_m^\circ$ (BaCs₂(MoO₄)₂, cr, 298.15K) = - (3066.6 ± 3.1) kJ/mol) and standard entropy (S_m° (Cs₂Ba(MoO₄)₂, cr, 298.15K) = 381.2 ± 11.8 J/(K mol)) determined by Smith et al. [123] as well as the heat capacity functions of BaMoO₄ and Cs₂MoO₄. These heat capacity functions were combined using the Neumann-Kopp approximation (Appendix D), since no experimental data is available. This gives the calculated Gibbs energy function for BaCs₂(MoO₄)₂:

$$G^{\text{BaCs}_2(\text{MoO}_4)_2} [\text{J/mol}] = 298.15 - 3143399.04432646 + 1145.36339T - 217.6657 \cdot T \ln T - 0.1137012T^2 + 1.1719 \cdot 10^{-5}T^3 + 360152.95T^{-1} \quad (3.9)$$

The liquid was described with the ionic two-sublattice model, with Ba²⁺, Cs⁺ and Mo⁴⁺ cations on the first sublattice and MoO₄²⁻, O²⁻ anions, charged vacancies (Va^{Q-}) and CsO₂, MoO₃ and O neutral species on the second sublattice:

$$(\text{Ba}^{2+}, \text{Cs}^+, \text{Mo}^{4+})_P (\text{MoO}_4^{2-}, \text{O}^{2-}, \text{Va}^{Q-}, \text{CsO}_2, \text{MoO}_3, \text{O})_Q \quad (3.10)$$

where, P and Q are equal to the average charge of the opposite sublattice in accordance with the previously described equations 2.49 and 2.50 in section 2.6:

$$Q = 2y_{\text{Ba}^{2+}} + y_{\text{Cs}^+} + 4y_{\text{Mo}^{4+}} \quad (3.11)$$

$$P = 2y_{\text{MoO}_4^{2-}} + 2y_{\text{O}^{2-}} + Qy_{\text{Va}^{Q-}} \quad (3.12)$$

Filling in equation 2.51 from section 2.6 then gives the Gibbs energy of the liquid phase as follows:

$$\begin{aligned} G^{\text{liquid}} = & y_{\text{Ba}^{2+}} y_{\text{MoO}_4^{2-}} \circ G_{(\text{Ba}^{2+})_2(\text{MoO}_4^{2-})_2} + y_{\text{Ba}^{2+}} y_{\text{O}^{2-}} \circ G_{(\text{Ba}^{2+})_2(\text{O}^{2-})_2} + Q y_{\text{Ba}^{2+}} y_{\text{Va}^{Q-}} \circ G_{(\text{Ba}^{2+})_2(\text{Va}^{Q-})_2} \\ & + y_{\text{Cs}^+} y_{\text{MoO}_4^{2-}} \circ G_{(\text{Cs}^+)_2(\text{MoO}_4^{2-})_1} + y_{\text{Cs}^+} y_{\text{O}^{2-}} \circ G_{(\text{Cs}^+)_2(\text{O}^{2-})_1} + Q y_{\text{Cs}^+} y_{\text{Va}^{Q-}} \circ G_{(\text{Cs}^+)_1(\text{Va}^{Q-})_1} \\ & + y_{\text{Mo}^{4+}} y_{\text{MoO}_4^{2-}} \circ G_{(\text{Mo}^{4+})_2(\text{MoO}_4^{2-})_4} + y_{\text{Mo}^{4+}} y_{\text{O}^{2-}} \circ G_{(\text{Mo}^{4+})_2(\text{O}^{2-})_4} + Q y_{\text{Mo}^{4+}} y_{\text{Va}^{Q-}} \circ G_{(\text{Mo}^{4+})_4(\text{Va}^{Q-})_4} \\ & + Q y_{\text{CsO}_2} \circ G_{\text{CsO}_2} + Q y_{\text{MoO}_3} \circ G_{\text{MoO}_3} + Q y_{\text{O}} \circ G_{\text{O}} \\ & + RT \left[P \left(y_{\text{Ba}^{2+}} \ln y_{\text{Ba}^{2+}} + y_{\text{Cs}^+} \ln y_{\text{Cs}^+} + y_{\text{Mo}^{4+}} \ln y_{\text{Mo}^{4+}} \right) + Q \left(y_{\text{MoO}_4^{2-}} \ln y_{\text{MoO}_4^{2-}} + y_{\text{O}^{2-}} \ln y_{\text{O}^{2-}} \right. \right. \\ & \left. \left. + y_{\text{Va}^{Q-}} \ln y_{\text{Va}^{Q-}} + y_{\text{CsO}_2} \ln y_{\text{CsO}_2} + y_{\text{MoO}_3} \ln y_{\text{MoO}_3} + y_{\text{O}} \ln y_{\text{O}} \right) \right] + G_{\text{tern}}^{\text{excess}} + G_{\text{quat}}^{\text{excess}} \end{aligned} \quad (3.13)$$

where the Gibbs reference terms ($^{\circ}\text{G}$) correspond to $\text{BaMoO}_4(\text{l})$ (times two), $\text{BaO}(\text{l})$ (times two), barium metal, Cs_2MoO_4 , $\text{Cs}_2\text{O}(\text{l})$, caesium metal, Mo_6O_{16} , MoO_2 (times two), molybdenum metal, $\text{CsO}_2(\text{l})$, $\text{MoO}_3(\text{l})$ and pure oxygen, respectively. $G_{\text{tern}}^{\text{excess}}$ represents the interaction term of the ternary sub-systems Ba-Mo-O and Cs-Mo-O and $G_{\text{quat}}^{\text{excess}}$ represents the interaction term of the quaternary system Ba-Cs-Mo-O. For the sake of clarity, the large amount of optimised interaction parameters within $G_{\text{tern}}^{\text{excess}}$ are not reported. They can be found in two papers published by Smith et al. (Ba-Mo-O [120] and Cs-Mo-O [121]). $G_{\text{quat}}^{\text{excess}}$ is given by filling in equation 2.52 in section 2.6:

$$G_{\text{quat}}^{\text{excess}} = Y_{\text{Ba}^{2+}} Y_{\text{Cs}^+} Y_{\text{MoO}_4^{2-}} L_{(\text{Ba}^{2+}, \text{Cs}^+)_P (\text{MoO}_4^{2-})_Q}^0 \quad (3.14)$$

To model the quaternary liquid phase, the interaction parameter (L^0) is optimised. It can be found in table 3.18.

Two CALPHAD models

The model shown in figure 3.29 depicts the phase diagram with the best fit to the experimental data points. The polymorphic transition of $\alpha\text{Cs}_2\text{MoO}_4$ to $\beta\text{Cs}_2\text{MoO}_4$ at 839.4K is within the uncertainty margin of the value determined by Smith et al.: $839 \pm 5\text{K}$ [121] and the eutectic line at 1184K seems to fit the experimental data well (table 3.17). Shifting the position of the peritectic $\text{BaCs}_2(\text{MoO}_4)_2$ decomposition line is done by optimising the solid Gibbs energy function of the quaternary compound (table 3.18), which changes its standard enthalpy of formation ($\Delta_f H_m^{\circ}$) and standard entropy (S_m°) in the model. These optimised values have to stay within the uncertainty margins of the experimentally determined values by Smith et al. [123] in table 3.16.

Unfortunately, when the original $\Delta_f H_m^{\circ}$ value was used, it was too high for the model to find $\text{BaCs}_2(\text{MoO}_4)_2$ stable enough to appear in the phase diagram. $\text{BaCs}_2(\text{MoO}_4)_2$ only became stable after the $\Delta_f H_m^{\circ}$ value was decreased by approximately 8 kJ/mol outside of the uncertainty margins set by Smith et al. [123], even whilst simultaneously increasing S_m° to the highest possible value to stabilise $\text{BaCs}_2(\text{MoO}_4)_2$. These values resulted in a model that has a bad fit to the experimental phase diagram data, but with $\Delta_f H_m^{\circ}$ and S_m° as close as possible to the uncertainty margin (figure 3.28). Further decreasing $\Delta_f H_m^{\circ}$ resulted in a model with a good fit to the experimental phase diagram data points (figure 3.29), but with both the standard enthalpy of formation and standard entropy values outside the uncertainty margin in table 3.16. Equilibrium temperatures calculated from this model are reported in table 3.17.

Table 3.16: Standard enthalpy of formation and standard entropy for the two CALPHAD models as well as the experimental values determined by Smith et al. [123]

| | Figure 3.29 | Figure 3.28 | Literature [123] |
|---------------------------------|-------------|-------------|-----------------------|
| $\Delta_f H_m^{\circ}$ [kJ/mol] | -3082.3 | -3077.6 | $-(3066.6 \pm 3.1)^a$ |
| S_m° [J/(K mol)] | 393.2 | 393.2 | 381.2 ± 11.8 |

^aThis value and its uncertainty were calculated based on the standard enthalpy of formation of Cs_2MoO_4 [-1514.25 ± 0.72] kJ/mol, [10, 38, 56, 119, 123]. It was later found that this uncertainty is underestimated and that the $\Delta_f H_m^{\circ}$ uncertainty is probably more in the range of $\pm 5\text{-}6$ kJ/mol.

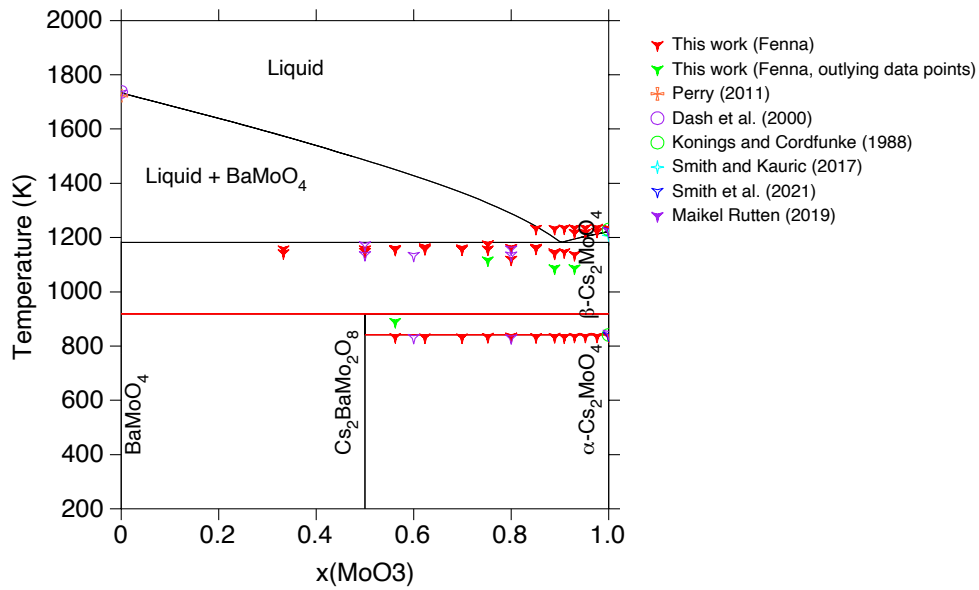


Figure 3.28: New $(1-x)\text{BaMoO}_4 - (x)\text{Cs}_2\text{MoO}_4$ CALPHAD model with a bad fit but with $\Delta_f H_m^\circ$ and S_m° values closest to the uncertainty margin. Data points by Perry [98], Dash et al. [26], Konings and Cordfunke [38] and Smith and Kauric [118], Smith et al. [121] and M. Rutten [111]

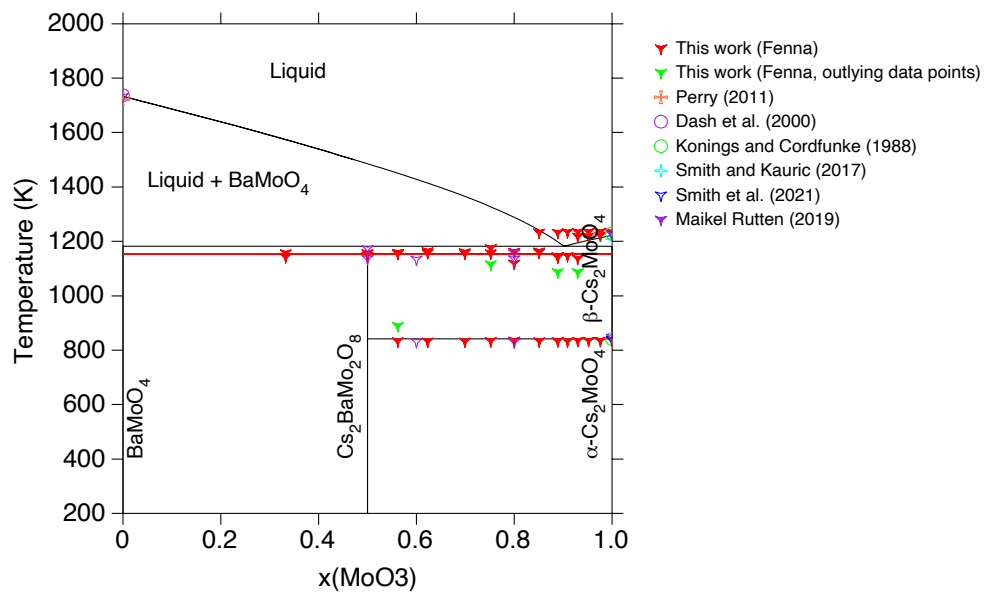


Figure 3.29: New $(1-x)\text{BaMoO}_4 - (x)\text{Cs}_2\text{MoO}_4$ CALPHAD model with a good fit. Data points by Perry [98], Dash et al. [26], Konings and Cordfunke [38] and Smith and Kauric [118], Smith et al. [121] and M. Rutten [111]

Table 3.17: Key equilibria calculated from the best-fit CALPHAD model (figure 3.29) in the BaMoO₄ – Cs₂MoO₄ pseudo-binary section.

| Invariant equilibrium | Equilibrium type | CALPHAD method | | Exp. data | | |
|--|-----------------------|--------------------------------------|------|--------------------------------------|---------------------------|--------------------|
| | | x(Cs ₂ MoO ₄) | T/K | x(Cs ₂ MoO ₄) | T/K | Ref. |
| BaCs ₂ (MoO ₄) ₂ → β Cs ₂ MoO ₄ + BaMoO ₄ | Peritectoid | 0.5 | 1153 | 0.333 | 1148.73 ± 5 ^a | This work |
| α Cs ₂ MoO ₄ → β Cs ₂ MoO ₄ | Polymorphism | 0.623 | 841 | 1.0 | 839 ± 5 ^a | Smith et al. [134] |
| β Cs ₂ MoO ₄ + BaMoO ₄ → liq. ³ | Eutectic ^b | 0.909 | 1182 | 0.909 | 1144.76 ± 10 ^a | This work |
| β Cs ₂ MoO ₄ → liq. ³ | Congruent melting | 1.0 | 1223 | 1.0 | 1226 ± 5 | Smith et al. [134] |

^aonly 1st cycle results, no statistical significance

^bpossibly

Table 3.18: Summary of the thermodynamic data for compounds used during CALPHAD modelling of the BaMoO₄ - Cs₂MoO₄ pseudo-binary section.

| Phase | Gibbs energy/ (J mol ⁻¹) | Ref. |
|------------------|--|-------------------------------------|
| Liquid | $L_{(Ba^{2+},Cs^+)P(MoO_4^2-)Q}^0 = -5000$ | This work |
| Solid | | |
| (Figure 3.28) | $G_{BaCs_2(MoO_4)_2} = CS2BAMO2O8\# - 11000 - 12T$ | This work |
| (Figure 3.29) | $G_{BaCs_2(MoO_4)_2} = CS2BAMO2O8\# - 15700 - 12T$ | This work |
| Functions | $G_{BaCs_2(MoO_4)_2} = -3143399.04432646 + 1145.36339T - 217.6657T \cdot \ln(T)$ $- 0.1137012T^2 + 1.1719 \cdot 10^5 T^3 + 360152.95T^{-1}$ $G_{BaMoO_4} = -1586142.5 + 670.3498T - 121.7475T \cdot \ln(T)$ $- 0.01959T^2 + 312416.95T^{-1}$ $G_{Cs_2MoO_4} = -1554486.3 + 448.47296T - 95.9182T \cdot \ln(T)$ $- 0.0941112T^2 + 1.1719E-05T^3 + 47736T^{-1}$ | [123] [120] [121] |

3.3 Sr-Mo-O system: investigation of the SrMoO₄ - MoO₃ pseudo-binary section

Data on the SrMoO₄ - MoO₃ pseudo binary section has been published by Zhukovski et al. [130], the Perry handbook [98] and Cordfunke and Konings [38]. This chapter will elaborate on previously unpublished work that has been done by the RPNM research group at the TU Delft. The compounds that were used for these measurements were bought, therefore no synthesis methods will be discussed.

3.3.1 Phase diagram investigations by DSC

The current SrO - MoO₃ phase diagram (as introduced in chapter 1.4) is shown in figure 3.30 below. The main objective for this phase diagram was to confirm the position of the eutectic equilibrium in the area 0.75 ≤ x(MoO₃) ≤ 0.85. Measurements were done with a TGDSC and the methodology behind this measurement technique was explained in chapter 2.3. SrMoO₄ (Alfa Aesar, 99%) and MoO₃ (Alfa Aesar, 99.99%) were mixed in different ratios to obtain four different compositions in the eutectic

equilibrium area at $x(\text{MoO}_3) = 0.769, 0.781, 0.806$ and 0.820 (table 3.19). BN powder was used for these measurements.

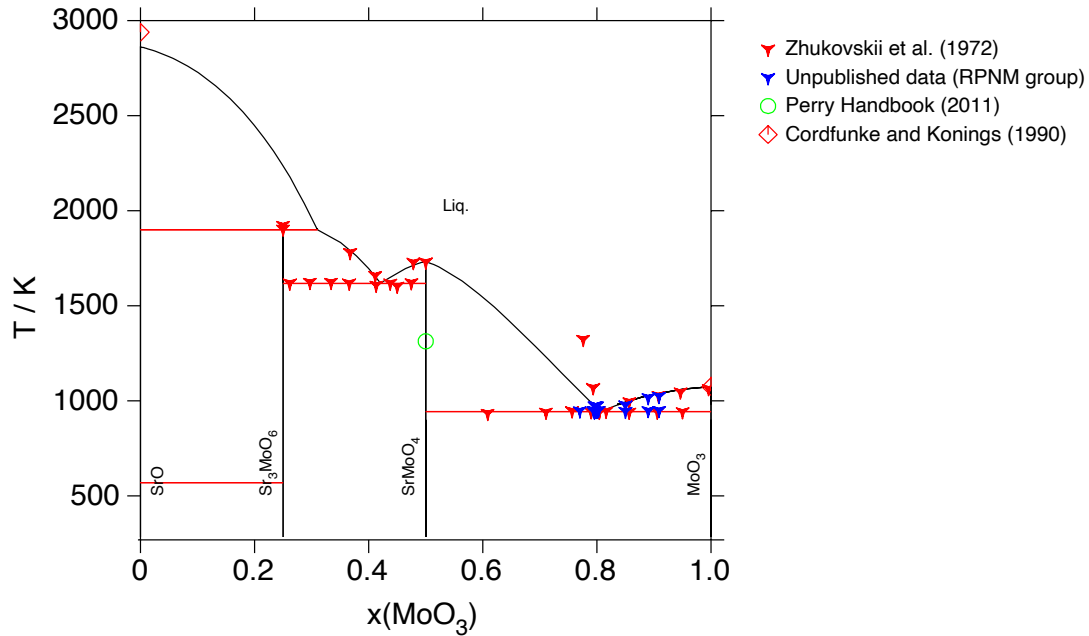


Figure 3.30: Current SrO - MoO₃ phase diagram. Data points by Zhukovski et al. [130], the Perry handbook [98], Cordfunke and Konings [38] and unpublished data by the RPNM research group.

Table 3.19: Molar ratios of the compounds used to mix the compositions that were measured

| $x(\text{MoO}_3)$ | Molar ratio | |
|-------------------|------------------|----------------|
| | SrMoO_4 | MoO_3 |
| 0.50 | 1 | |
| 0.769 | 0.30 | 0.70 |
| 0.781 | 0.28 | 0.72 |
| 0.806 | 0.24 | 0.76 |
| 0.820 | 0.22 | 0.78 |
| 1.0 | | 1 |

This set of experiments had the same limitation as the BaO - MoO₃ measurements, where MoO₃ was found to evaporate above 1008K. Unfortunately, this temperature limitation would make it impossible to see the liquidus line for some of the measurements, but the expectation was that the liquidus would still be visible around the eutectic equilibrium and that its position could therefore be determined. The results are shown below in figure 3.31. It only shows the SrMoO₄ - MoO₃ area, between $0.50 \leq x(\text{MoO}_3) \leq 1.0$, of the phase diagram to display the individual data points more clearly.

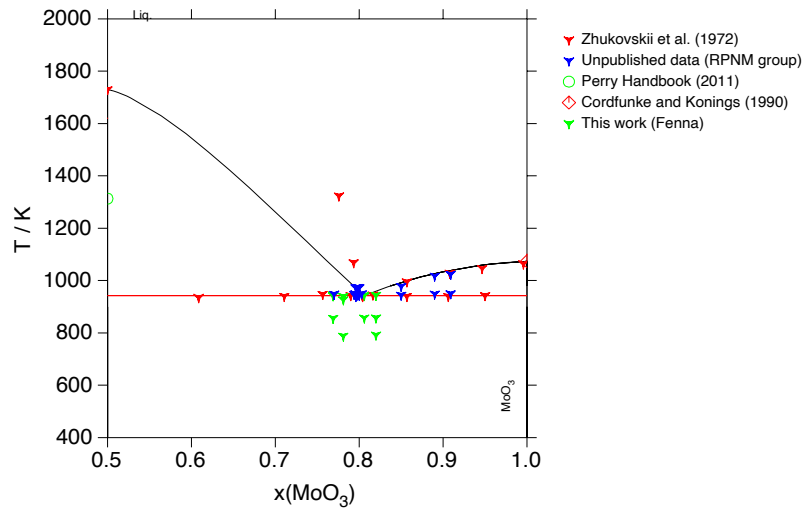


Figure 3.31: SrMoO_4 - MoO_3 phase diagram with TGDSC measurement results

3.3.1.1 Outlying data point discussion

It is clear that not all data points follow the lines of the phase diagram model. These outlying points are discussed in the Appendix (C.3). In summation, the $\pm 790\text{K}$ events were likely caused by a contamination in SrMoO_4 and/ or MoO_3 . The cause of the outlying points at $\pm 850\text{K}$ remains unclear. It is recommended to repeat the measurements with newly bought MoO_3 , SrMoO_4 and BN to see whether the outlying peaks occur again.

3.3.1.2 Measurement of the eutectic equilibrium in the region $0.5 \leq x(\text{MoO}_3) \leq 1.0$

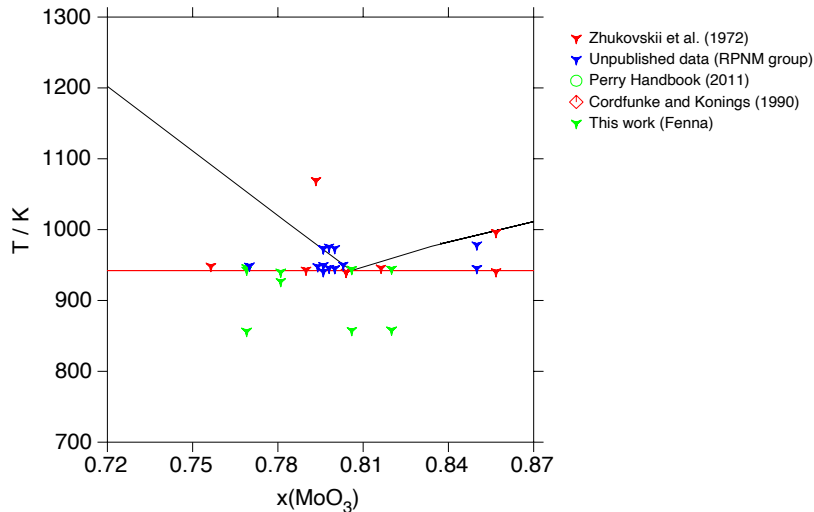


Figure 3.32: Zoomed section in the SrO - MoO_3 phase diagram with TGDSC results obtained in this work

Figure 3.32 gives the final result for the SrO - MoO₃ phase diagram. The $\pm 790\text{K}$ outlying data points were removed from the model, because a likely cause for them was determined. Since no explanation has been found for the remaining outlying events, they were not removed. To determine the position of the eutectic equilibrium, one heating cycle of each measurement was compared in figure 3.33.

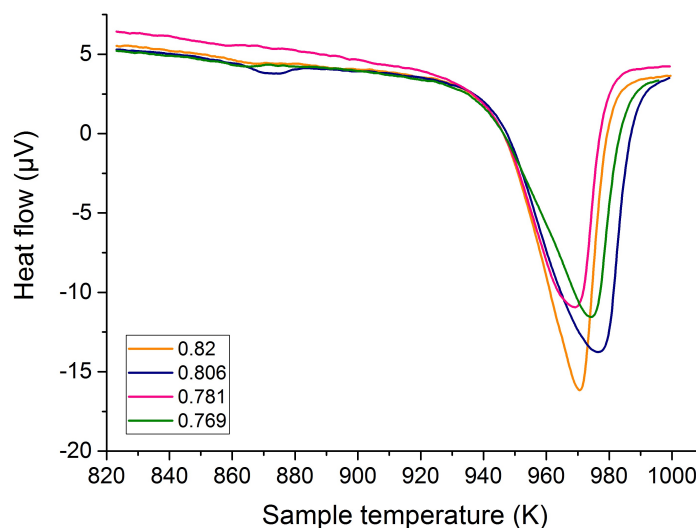


Figure 3.33: TGDSC heating cycles of $x(\text{MoO}_3) = 0.769$ (cyan), 0.781 (pink), 0.806 (blue) and 0.82 (orange) as well as the sample temperature [K] (black) vs. time [s]

The heating cycle of $x(\text{MoO}_3) = 0.769$ shows a slight shoulder on the left side of the peak (difficult to see in the figure, but apparent during analysis). According to the model, the liquidus line is predicted to be positioned approximately 110K higher than the eutectic line at this composition, so it is unclear which event the shoulder represents. The XRD pattern of this TGDSC measurement did not show any contaminations (see table 3.20).

The shoulder is still visible at $x(\text{MoO}_3) = 0.781$. The liquidus and eutectic lines at this composition are approximately 80K apart in the model. Even if it is taken into consideration that this liquidus line is modelled on a limited amount of experimental data points (which could lead to some uncertainty), it seems unlikely that the 4K difference between the shoulder and the main heating peak could represent the eutectic and liquidus events at this composition. The expected temperature of the liquidus event at 1017K is also too high to be recorded within the temperature limitation of 1008K. Therefore, the liquidus line in the model would have to change significantly if the event was actually recorded during this measurement.

No shoulder was detected in the $x(\text{MoO}_3) = 0.806$ peak. The slight bump around 870K in the heating cycle represents the $\pm 855\text{K}$ outlying peak that was discussed during the previous segment. It is clearly very small compared to the main peak. This composition is situated at the predicted eutectic position by the model in figure 3.32. The $x(\text{MoO}_3) = 0.82$ measurement also shows no shoulder. The liquidus event at this composition is expected to occur at approximately 963K, which may or may not be visible within the temperature limitation of 1008K.

It is possible that no shoulders are visible for both compositions, because the eutectic equilibrium is positioned at $x(\text{MoO}_3) = 0.806$ and the liquidus event at $x(\text{MoO}_3) = 0.82$ is not visible. For now, it is

concluded that the eutectic equilibrium is positioned between 0.806 and 0.82, with the recommendation to do measurements at a higher temperature (maybe with an encased DSC crucible to prevent the evaporation of MoO_3) to get a better idea of the position of the liquidus line (most importantly in the area $0.720 \leq x(\text{MoO}_3) \leq 0.806$). These measurements should be done with newly bought MoO_3 , SrMoO_4 and BN to exclude any interference with possible contaminants in those powders.

Table 3.20: Equilibrium data collected by TGDSC of compositions $x(\text{MoO}_3)$ in the $\text{SrMoO}_4 - \text{MoO}_3$ pseudo-binary phase diagram. Only the peaks shown in figure 3.32 are included. Post-XRD observed phases are in order of significance.

| $x(\text{MoO}_3)$ | T_{eq} | Equilibrium | Equilibrium reaction | Post-XRD |
|-------------------|-----------------|-------------|--|--------------------------------|
| 0.50 | 799.37 ± 5 | Unknown | Unknown | SrMoO_4 |
| 0.769 | 856.52 ± 10 | Unknown | Unknown | $\text{MoO}_3, \text{SrMoO}_4$ |
| | 942.82 ± 10 | Unknown | Unknown | |
| | 946.55 ± 10 | Eutectic | $\text{SrMoO}_4 + \text{MoO}_3 \rightarrow \text{SrMoO}_4 + \text{liq.}^1$ | |
| 0.781 | 940.08 ± 10 | Eutectic | $\text{SrMoO}_4 + \text{MoO}_3 \rightarrow \text{SrMoO}_4 + \text{liq.}^1$ | $\text{MoO}_3, \text{SrMoO}_4$ |
| 0.806 | 943.96 ± 10 | Eutectic | $\text{SrMoO}_4 + \text{MoO}_3 \rightarrow \text{liq.}^3$ | $\text{MoO}_3, \text{SrMoO}_4$ |
| 0.82 | 858.32 ± 10 | Unknown | Unknown | $\text{MoO}_3, \text{SrMoO}_4$ |
| | 944.44 ± 10 | Eutectic | $\text{SrMoO}_4 + \text{MoO}_3 \rightarrow \text{MoO}_3 + \text{liq.}^2$ | |

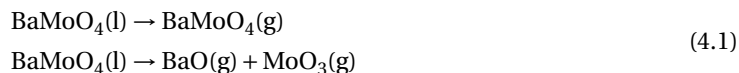
Chapter 4

Vapour pressure studies: results and discussion

Vapour pressure studies were performed on BaMoO₄ using Knudsen Effusion Mass Spectrometry (KEMS). The theory behind this measurement technique is reported in chapter 2.5. This chapter will discuss previously published vapour pressure results and how the findings of the experiment in this work differ significantly from them. Appearance energies of ionic species are determined by means of the intensity vs. eV data, which are matched to documented ionisation energies in order to find the parent molecules of the detected ions. Partial pressure functions of all gaseous components are calculated according to two possible scenarios. Finally, the results of two TGDSC experiments with BaMoO₄(s) (under O₂ and Ar atmosphere) are discussed, to shed more light on the composition of the BaMoO₄ sample during a KEMS measurement.

4.1 Literature study results

Two BaMoO₄ vapour pressure studies, by Pupp et al. [101] and Kazenas et al. [125, 140], have been found in the literature. Pupp et al. investigated three mixtures: liquid BaMoO₄, BaMoO₄ + MoO₃ and BaMoO₄ + BaO in a temperature range of 1800-2200K in a molybdenum Knudsen cell at 75eV. The enthalpy of vaporisation of liquid BaMoO₄ at 2000K was reported to be (3493.6 ± 21) kJ/mol. Relative intensities of detected ions were given (table 4.1), but the total vapour pressure over the BaMoO₄ sample was not calculated. The authors found that the vapour phase during the experiment consisted mainly of molecular BaMoO₄ and that congruent vaporisation seemed to be the most prominent reaction, according to the following reactions:



The most prominent ionic species were found to be BaMoO₄⁺, BaO⁺ and MoO₃⁺ (figure 4.1). These ions were considered to originate from ionisation reactions with gaseous species BaMoO₄(g), BaO(g) and MoO₃(g) respectively. BaMoO₃⁺ was found to originate from a fragmentation reaction with BaMoO₄(g). These conclusions were based on the comparison between the appearance energies of the ions and their reported ionisation energies. Also, no high mass species were detected which could have created BaMoO₄⁺ by means of a fragmentation reaction [101].

Kazenas et al. [125, 140] investigated the sublimation of BaMoO_4 in a molybdenum Knudsen Cell in a temperature range of 1640 – 1770K and at 70eV. This paper also reported the relative intensities of detected ionised species (table 4.1). In contrast to Pupp et al. [101], $\text{BaMoO}_3^+(g)$ was recorded as the second-to-highest intensity after $\text{BaMoO}_4^+(g)$. Also, $\text{BaO}^+(g)$ and $\text{Ba}^+(g)$ had significantly lower intensities. Both papers did agree on the congruent sublimation/vaporisation of BaMoO_4 , but Kazenas et al. gave a higher weight to the gas-phase dissociation reaction of $\text{BaMoO}_3(g)$ (equation 4.2).

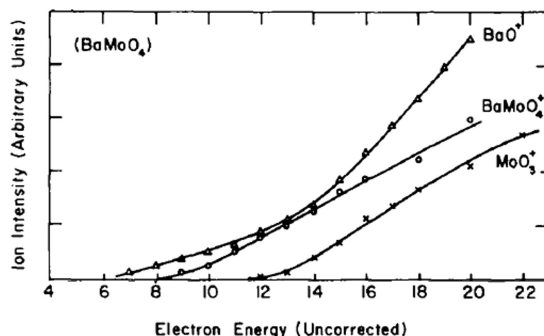
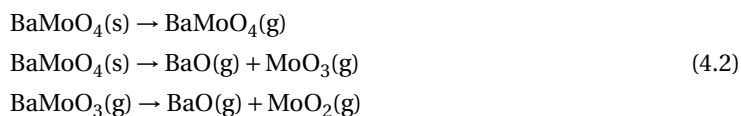


Figure 4.1: The ion intensity in arbitrary units of BaO^+ , BaMoO_4^+ and MoO_3^+ vs. electron energy in eV [101]



The paper calculated the enthalpy of formation of BaMoO_4 : $\Delta_f H_m^\circ(\text{BaMoO}_4, g) = 1066 \pm 42 \text{ kJ/mol}$ and the partial pressure of BaMoO_4 was found to be:

$$\log p(\text{BaMoO}_4), \text{atm} = -17858/T + 4.38 \tag{4.3}$$

4.2 Experimental results

4.2.1 Method

The KEMS measurements of BaMoO_4 were performed at JRC Karlsruhe. The Knudsen cell consisted of tungsten metal, which is unreactive towards BaMoO_4 . It was heated under high vacuum ($\pm 10^{-6}$ mbar) by a high temperature furnace made from tungsten coil. The high-vacuum condition is important to exclude any unrelated gaseous species from the experiment and to make sure the evaporated molecules from the sample do not collide with them. The sample was heated up to 2400K at a constant heating rate of 10K/min. The molecular beam from the orifice of the Knudsen cell was ionised by means of electron bombardment with an energy of 32.85 eV. To obtain intensity vs. eV data, the temperature of the sample was kept constant at two intervals, 1886K and 2192K, during which time the energy of the electron bombarding cross beam (in eV) was varied and the intensity of the resulting ions was detected. This data allowed for the determination of appearance energies of the detected ions, as will be discussed below. Silver was used to calibrate the KEMS apparatus and the complete BaMoO_4 sample was vaporised during the experiment.

4.2.2 Relative ion intensities

The relative ion intensities found by Pupp et al. [101] and Kazenas et al. [125, 140] are shown in table 4.1, together with the results from this work. It is clear that all results are quite different. The intensities of Kazenas et al. are almost the reverse of results by this work, with Ba^+ having the highest, and BaMoO_4^+ almost the lowest intensity. This suggests a significant influence of fragmentation reactions, in contrast to Pupp et al. and Kazenas et al., who both found congruent vaporisation to be dominant.

However, even though both detected BaMoO_4^+ with the highest intensity, the intensity of BaMoO_3^+ differed significantly between both studies. Both found that BaMoO_3^+ was produced by a fragmentation reaction from $\text{BaMoO}_4(\text{g})$, but the detected intensity of BaMoO_3^+ is significantly higher for Kazenas et al. than for Pupp et al.

Table 4.1: Relative ion intensities reported by Pupp et al. [101] and Kazenas et al. [125,140] compared to detected ion species in this work in order of decreasing intensity

| This work at 32 eV and 1950 K | Pupp et al. at 75 eV and 1950 K [101] | | Kazenas et al. at 70 eV and 1740 K [125, 140] | | |
|-------------------------------|---------------------------------------|--------------------|---|--------------------|--------------------|
| Ion species | Ion species | Relative intensity | Parent gaseous species | Ion species | Relative intensity |
| Ba^+ | BaMoO_4^+ | 100 | BaMoO_4 | BaMoO_4^+ | 100 |
| BaO^+ | MoO_3^+ | 64.7 | MoO_3 | BaMoO_3^+ | 74.3 |
| MoO_2^+ | BaO^+ | 59.2 | BaO/BaMoO_4 | MoO_3^+ | 65 |
| MoO^+ | MoO_2^+ | 47.5 | | MoO_2^+ | 34 |
| MoO_3^+ | Ba^+ | 33 | | BaO^+ | 27 |
| Mo^+ | BaMoO_3^+ | 26.7 | BaMoO_4 | Ba^+ | 6 |
| BaMoO_4^+ | MoO^+ | 11.2 | | | |
| BaMoO_3^+ | | | | | |
| BaMoO_2^+ | | | | | |

It is difficult to compare the three sets of results, because they were obtained under different conditions (different ionisation energies, Knudsen cell material (W vs. Mo) and temperature ranges). It is not possible to determine the effect of these varying conditions on the intensities of the detected ions. It is however interesting, that the higher ionisation energies used by the two studies did not cause as many fragmentation reactions as the lower ionisation energy in this work, because fragmentation reactions require more energy than more simple ionisation reactions. The next data analysis step is to find the parent species of the ions that were detected. This is done by determining the appearance energies of the ions during the experiment. This topic will be discussed in the section below.

4.2.3 Determination of appearance energies and parent molecules

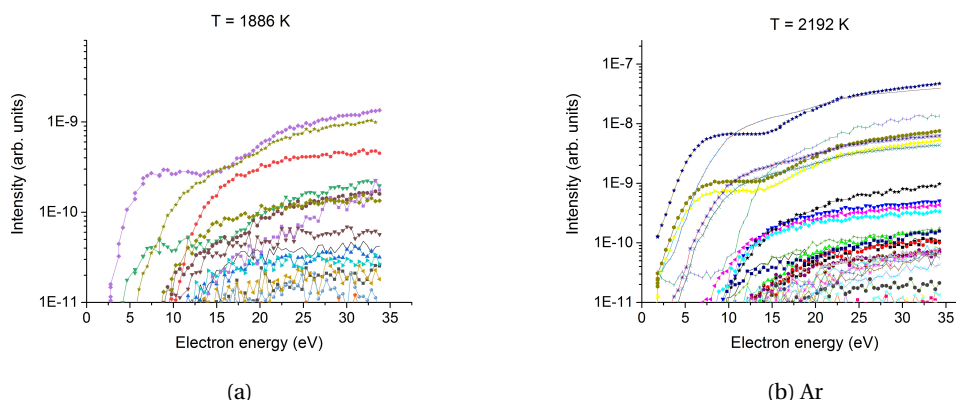


Figure 4.2: Intensity in arbitrary units of all detected ionic species vs. electron energy in eV at temperature intervals 1886K (a) and 2192K (b)

Figure 4.2 shows the intensity of all detected gaseous ionic species vs. the energy of the electron bombarding cross beam in eV at two constant temperatures, 1886 and 2192K. These graphs include all measured isotopes (too many to show in a legend). Only data of the species consisting of the most abundant isotopes were analysed going forward. The influence of the lesser abundant isotopes is accounted for in the partial pressure calculations (as explained in section 2.5). It is clear that the detected intensities of the ions are higher at 2192K than at 1886K, which results in cleaner curves with less noise. Because of this, only the 2192K graphs were used to determine the appearance energies of the detected ions. The graphs of the most dominant ionic species (and with the most abundant isotopes) at 2192K are depicted in figure 4.3.

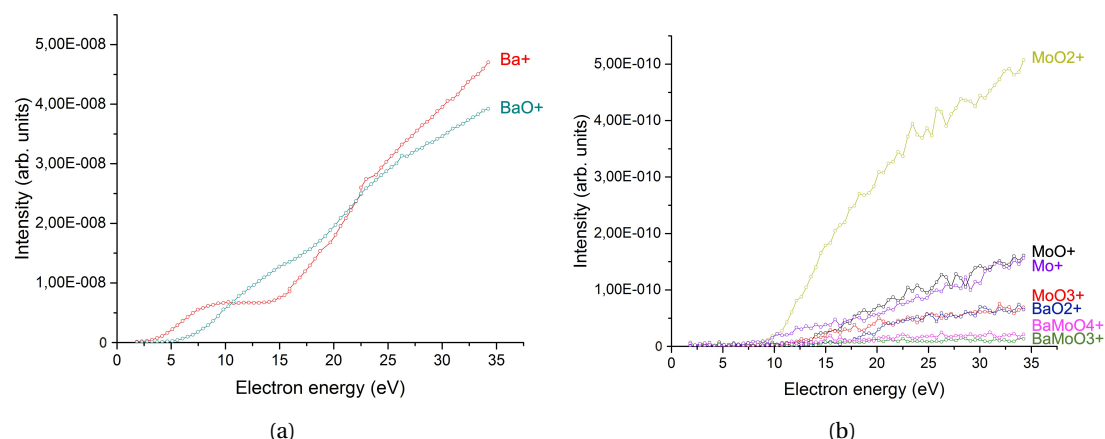


Figure 4.3: Intensity in arbitrary units of the most prominent detected ionic species Ba^+ , BaO^+ , MoO_2^+ , MoO^+ , MoO_3^+ , BaO_2^+ , BaMoO_4^+ and BaMoO_3^+ vs. ionisation energy in eV

The appearance energy (AE) of a detected ion is determined by finding the x-coordinate of the intercept between the first slope and the x-axis (illustration in figure 4.4, AE1). The area where the slope > 0 indicates an increase in the intensity of the ion, meaning that the electron beam provides enough energy to ionise the gaseous parent molecule. Therefore, the appearance energy (e.g. the ionisation energy) is found at the start of this slope. When the slope decreases again to equal 0 (such is the case for Ba^+ in figure 4.4), the ionisation is complete. The second slope in figure 4.4 represents the addition of new Ba^+ ions that are produced by means of a different reaction. The appearance energy of this second event is determined by finding the x-coordinate of the intercept between the slope and baseline where the slope is equal to 0 (illustration in figure 4.4, AE2). The ratio between both events is determined by drawing a vertical line at 32.85eV (the ionisation energy of the KEMS measurement) and comparing the relative intensities there. This ratio is important when calculating the partial pressure of the gaseous parent molecules (explained in section 2.5). Not all ions are produced by two reactions. In this work, only

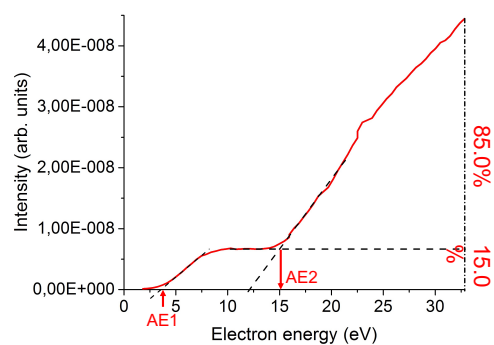


Figure 4.4: Illustration of the method with which the appearance energies of detected ions have been determined with the Ba^+ intensity vs. eV graph.

Ba⁺ and BaO⁺ visibly depicted two events (figure 4.3a).

By comparing the experimental appearance energies to documented ionisation energies, the parent molecule of each ion and each event can be determined. Extensive literature research was performed to find documented ionisation energies, but some had to be estimated or calculated with reported dissociation and ionisation energies due to a lack of experimental research. The results of this analysis are shown in table 4.2.

Table 4.2: Ionisation and appearance energies determined at 2192K in comparison with literature data

| Process | Potential /eV (this work) | Potential /eV (literature) | Reference |
|---|------------------------------|-----------------------------------|---|
| Ba(g) + e ⁻ → Ba ⁺ | 3.4 ± 0.1 | 5.21 5.21 5.211 | [63] [100] [34] |
| BaMoO ₃ (g) + e ⁻ → Ba ⁺ + ... | 15.3 ± 0.9 | 15.9 – 16.7 | Estimated ^a in this work from the data of [73, 125] [7, 63, 70, 100, 101, 127] |
| BaMoO ₄ (g) + e ⁻ → Ba ⁺ + ... | 15.3 ± 0.9 | 16.6 – 17.0 | Estimated ^b in this work from the data of [73, 125] [7, 63, 70, 81, 100, 101, 127] |
| BaO(g) + e ⁻ → BaO ⁺ | 6.3 ± 0.7 | 6.91 6.8 ± 0.02 6.89 ± 0.03 | [81] [86] [70] |
| BaMoO ₃ (g) + e ⁻ → BaO ⁺ + MoO ₂ (g) | 17.2 ± 0.7 | 11.7 – 12.7 | Estimated ^c in this work from the data of [36, 70] [73, 101, 125] |
| BaMoO ₄ (g) + e ⁻ → BaO ⁺ + MoO ₃ (g) | 17.2 ± 0.7 | 12.4-12.9 | Estimated ^d in this work from the data of [73, 125] [70, 81, 86, 125] |
| MoO ₂ (g) + e ⁻ → MoO ₂ ⁺ | 9.8 ± 0.5 | 9.33 | [71] |
| MoO ₃ (g) + e ⁻ → MoO ₃ ⁺ | 9.2 ± 1.1 | 9.68 | [12] |
| MoO ₂ (g) + e ⁻ → MoO ⁺ + ½O ₂ (g) | 11.7 ± 1.3 | 13.7 – 14.2 | Estimated ^e in this work from the data of [75, 115] [28, 82, 117] |
| Mo(g) + e ⁻ → Mo ⁺ | 7.6 ± 1.0 | 7.09 7.099 7.1 7.099 | [105] [80] [32] [34] |

^aData estimated from the reported dissociation energies for BaMoO₃(g) = BaO(g) + MoO₂(g), BaO(g) = Ba(g) + 1/2O₂(g), and ionisation energy of Ba(g)

^bData estimated from the reported dissociation energies for BaMoO₄(g) = BaO(g) + MoO₃(g), BaO(g) = Ba(g) + 1/2O₂(g), and ionisation energy of Ba(g).

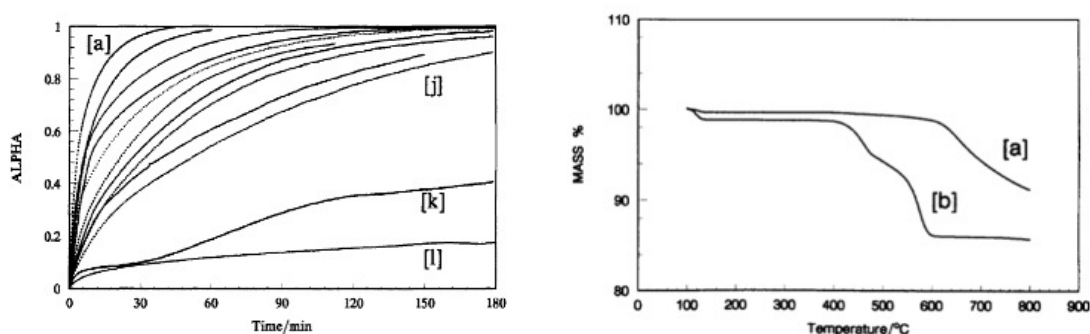
^cData estimated from the reported dissociation energy for BaMoO₃(g) = BaO(g) + MoO₂(g) and ionisation energy of BaO(g).

^dData estimated from the reported dissociation energy for BaMoO₄(g) = BaO(g) + MoO₃(g), and ionisation energy of BaO(g).

^eData estimated from the reported dissociation energy for MoO₂(g) = MoO(g) + 1/2O₂(g), and ionisation energy of MoO(g).

The appearance energies of some ions corresponded well to the found literature data. From table 4.2 it is apparent that Mo^+ , MoO_2^+ and MoO_3^+ are produced by an ionisation reaction from $\text{Mo}(\text{g})$, $\text{MoO}_2(\text{g})$ and $\text{MoO}_3(\text{g})$ respectively. The appearance energy of MoO^+ (11.7 ± 1.3) eV was too high to match the ionisation energy of the reaction $\text{MoO}(\text{g}) + \text{e}^- \rightarrow \text{MoO}^+$ ($7.44 - 8$ eV [28, 46, 82, 117]), and is considered to be formed by the fragmentation reaction with $\text{MoO}_2(\text{g})$ as is shown in the table. This means that $\text{MoO}(\text{g})$ is not formed during the vaporisation of $\text{BaMoO}_4(\text{s})$.

The first events of Ba^+ and BaO^+ seem to occur by an ionisation reaction from $\text{Ba}(\text{g})$ and $\text{BaO}(\text{g})$, respectively. Their second events however, cannot be clearly ascribed to any fragmentation reaction. $\text{BaO}(\text{g}) + \text{e}^- \rightarrow \text{Ba}^+ + \frac{1}{2}\text{O}_2$ ($11.01 - 11.04$ eV [34, 36, 63, 70, 92, 100, 124])¹ is too low for the second event of Ba^+ ($\text{AE} = 15.3 \pm 0.9$), but fragmentation from $\text{BaMoO}_4(\text{g})$ or $\text{BaMoO}_3(\text{g})$ is possible for both the second events of Ba^+ and BaO^+ . It seems illogical for both ions to originate from the same parent molecule, so during analysis it is assumed that they originate from $\text{BaMoO}_4(\text{g})$ or $\text{BaMoO}_3(\text{g})$. Neither ion can originate from $\text{BaO}_2(\text{g})$, because it has been shown to decompose at temperatures above 823K (figure 4.5, [131]), which is below the temperature of these recorded intensities at 2192K (and also below 1886K for that matter).

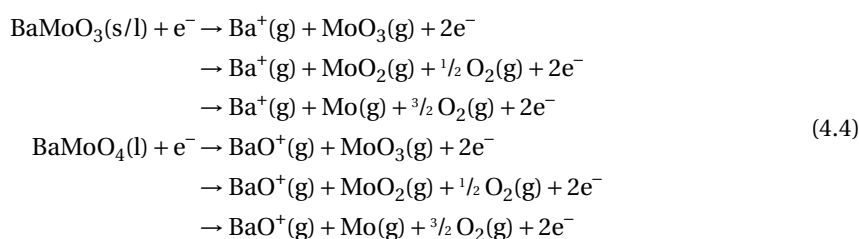


(a) Isothermal decomposition of BaO_2 in N_2 : [a] 610, [b] 600, [c] 590, [d] 570, [e] 550, [f] 530, [g] 520, [h], 510, [j] 500, [k] 495, and [l] 490 °C [131] (b) Mass loss of BaO_2 [a] and SrO_2 [b] when heated with $10^\circ\text{C}/\text{min}$ in N_2 [131]

Figure 4.5

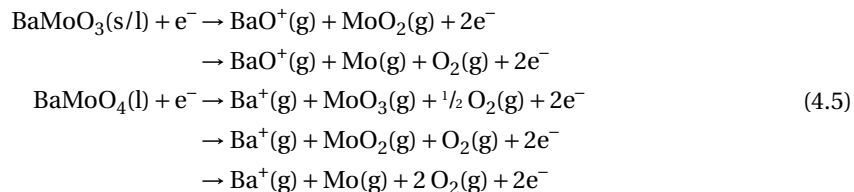
Based on the data in table 4.2, it seems most logical that the second events with Ba^+ and BaO^+ originate from a fragmentation reaction with $\text{BaMoO}_3(\text{g})$ and $\text{BaMoO}_4(\text{g})$ respectively, but the appearance/ionisation energy discrepancies are too high for a definitive conclusion. Possible reactions for the second events of Ba^+ and BaO^+ can be formulated as follows:

Scenario 1:



¹calculated from the dissociation reaction $\text{BaO}(\text{g}) \rightarrow \text{Ba}(\text{g}) + \frac{1}{2}\text{O}_2(\text{g})$ and the ionisation energy of $\text{Ba}(\text{g})$

or Scenario 2:



BaMoO₄ has a melting point of 1734K according to Smith et al. [120], so it melts during the experiment, that is why BaMoO₄(l) is used. Due to lack of thermodynamic data on BaMoO₃, it is not known whether the compound would melt within the temperature range of this experiment. Therefore, the phase of BaMoO₃ is written to be solid or liquid. Both of these scenarios will be used during the partial pressure calculations.

A small amount of BaO₂⁺ ions were also detected (AE = 16.28 ± 3.01 eV), but no ionisation energy values were found in the literature, and therefore it is not included in table 4.2. Since BaO₂⁺ cannot originate from BaO₂(g), it could have been formed by a fragmentation reaction with either BaMoO₄(g) or BaMoO₃(g). Because the intensity of BaO₂⁺ is so low, it does not have a great impact on the partial pressure of either BaMoO₃(g) or BaMoO₄(g), so for now the assumption is made that its parent molecule is BaMoO₄(g).

It is interesting to note the reported appearance energies of the detected ions by Pupp et al. [101]: BaMoO₄⁺ = 9.8 eV, BaMoO₃⁺ = 14.2 eV, MoO₃⁺ = 12.6 eV and BaO⁺ = 6.7eV (all ± 0.5 eV). No second event with BaO⁺ was detected. The appearance energy for BaO⁺ matches the results of this work reasonably well, but MoO₃⁺ does not, even though Pupp et al. do report that it is formed by the ionisation reaction from MoO₃(g). The found literature value for this reaction is 9.68 eV [12], which comes closer to the experimental appearance energy in table 4.2, than to the appearance energy found by Pupp et al.

4.3 Partial pressure calculations

Cross-sections and H_i values of all relevant molecules were calculated according to the equations in section 2.5. They are presented in table 4.3.

Table 4.3: Calculated cross sections and H_i values for each dominant gaseous compound

| Molecule (g) | Cross section [Å] | H _i |
|--------------------|-------------------|----------------|
| Ba | 17.14 | 15684.07 |
| BaO | 4.83 | 55662.87 |
| Mo | 6.80 | 39562.61 |
| MoO ₂ | 3.53 | 76161.95 |
| MoO ₃ | 3.81 | 70564.75 |
| BaMoO ₄ | 12.55 | 21422.44 |
| BaMoO ₃ | 9.58 | 28063.85 |

Using the values in table 4.3 and the equations discussed in section 2.5, the partial pressure of each gaseous molecule was calculated as a function of temperature, according to the two scenarios presented by equations 4.4 and 4.5. The first scenario assumes that the second Ba⁺ and BaO⁺ events originate from BaMoO₃(g) and BaMoO₄(g) respectively and the second scenario assumes the opposite. BaO₂⁺ was assumed to originate from BaMoO₄(g) for both scenarios.

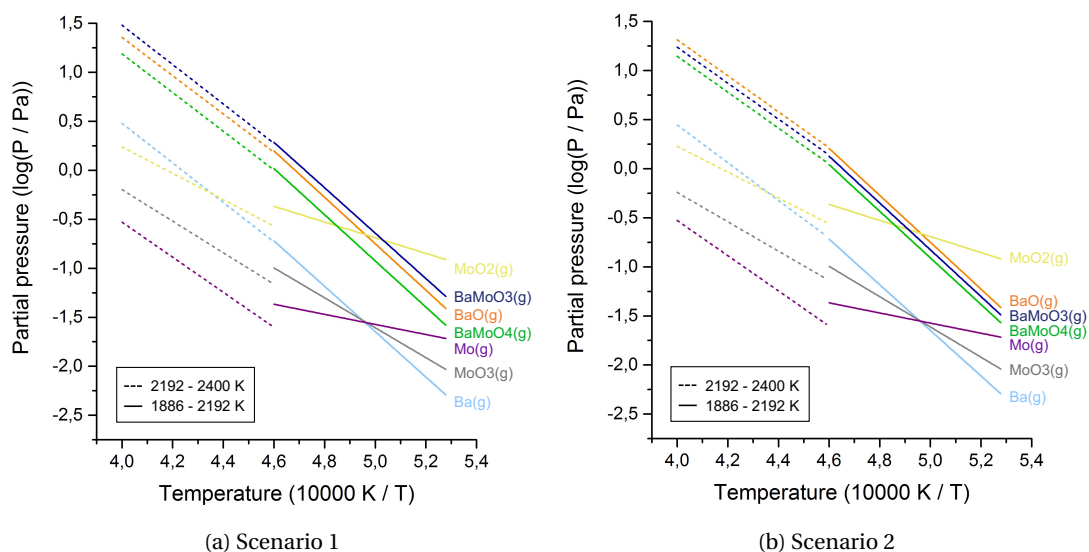


Figure 4.6: Partial pressures of all dominant gaseous compounds as a function of temperature, calculated with temperature intervals 1886 - 2192K (solid lines) and 2192 - 2400K (dashed lines). Scenario 1 as described by equation 4.4 (a) and scenario 2 as described by equation 4.5 (b)

Partial pressure functions according to both scenarios are shown in figure 4.6. Strangely, some of the results vary depending on the temperature interval that was used to calculate them. The results with the solid lines were calculated in the temperature range between the first and second intensity vs. eV measurement (1886 – 2192 K) and the results with the dashed lines come from after the second intensity vs. eV measurement (2192 – 2400 K). The slopes of all compounds remained somewhat constant (except Mo(g) and MoO₃(g)), but some lines jump up or down as they cross 2192K. It is not clear what caused these discontinuities. The melting of the sample should not affect the partial pressure calculations, because the melting point of BaMoO₄ at 1734K [120] is lower than the first temperature interval at 1886K. Sometimes, to avoid this discontinuation in the partial pressures, a second KEMS measurement is done where the sample is heated continuously at a constant value of eV (so without two intervals at a constant temperature). This way, the intensity curves (and after calculation the partial pressure curves) are not interrupted and are hence continuous. It is recommended to also perform such a measurement at a later time.

BaMoO₃(g) and BaMoO₄(g) are the only partial pressure functions that change between the two scenarios, all other partial pressure functions remain the same. In both scenarios, the partial pressure of BaMoO₃(g) is higher than BaMoO₄(g), only the difference between them is larger in scenario 1. The large presence of BaMoO₃(g) vapour above BaMoO₄(s), suggests the possibility of a partial reduction by the sample during the measurement, resulting in the reaction: $\text{BaMoO}_4(\text{s}) \rightarrow \text{BaMoO}_3(\text{g}) + 1/2 \text{O}_2(\text{g})$. In both scenarios, the partial pressure of BaO(g) is very high, suggesting a high influence of dissociation reactions by either BaMoO₄(g) or BaMoO₃(g). The partial pressures of MoO₂(g) and Ba(g) are in the same range, which suggests that they are produced by the same reaction. MoO₃(g) and Mo(g) both have the lowest partial pressures, approximately twice as low as BaMoO₄(g), BaMoO₃(g) and BaO(g).

Theoretical vapour compositions above pure BaMoO₄ and BaMoO₃ were calculated in a temperature range of 1820 - 2500K, to compare them to the experimental partial pressures in figure 4.6. This was

done using the thermodynamic model of the Ba-Mo-O system by Smith et al. [120] and the thermodynamic function for $\text{BaMoO}_4(\text{g})$ from the SGTE database (Scientific Group Thermodata Europe). The results can be seen in figure 4.7. Gaseous BaMoO_3 is not included, because of the lack of thermodynamic data on this compound.

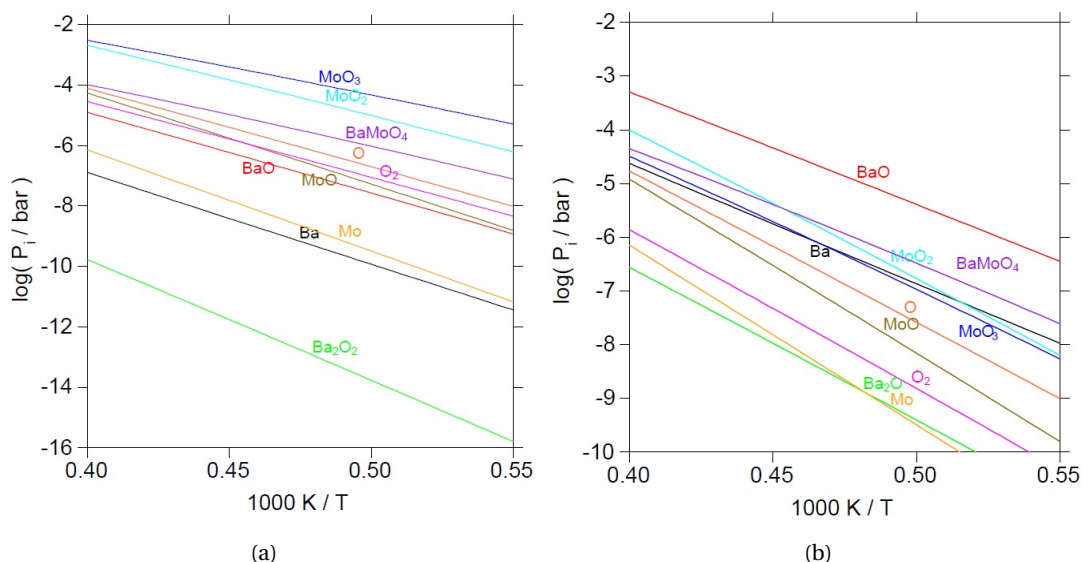
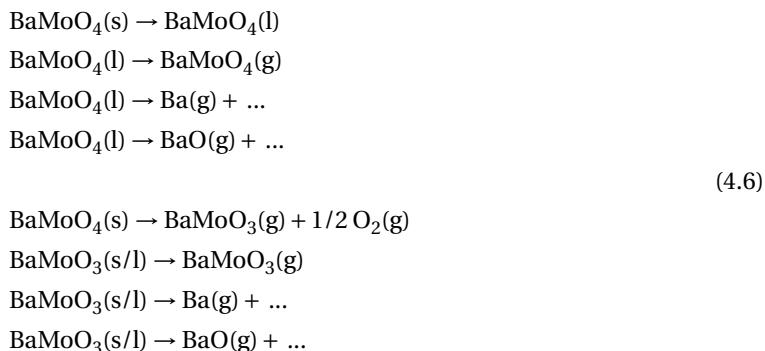


Figure 4.7: Calculated vapour composition in the temperature range 1820 - 2500 K above (a) pure BaMoO_4 and (b) pure BaMoO_3 using the thermodynamic model of Smith et al. [120]

Looking at both the experimental and theoretical models, the vapour composition above $\text{BaMoO}_3(\text{l})$ seems to represent the scenarios in figure 4.6 better than the vapour composition above $\text{BaMoO}_4(\text{l})$. According to the models in figure 4.7, the vapour above $\text{BaMoO}_4(\text{l})$ consists predominantly of $\text{MoO}_3(\text{g})$, $\text{MoO}_2(\text{g})$, $\text{BaMoO}_4(\text{g})$ and $\text{Mo}(\text{g})$ and the vapour above $\text{BaMoO}_3(\text{l})$ consists predominantly of $\text{BaO}(\text{g})$, $\text{MoO}_2(\text{g})$, $\text{BaMoO}_4(\text{g})$, $\text{MoO}_3(\text{g})$ and $\text{Ba}(\text{g})$. The latter composition matches the experimental results the most, mostly because of the predominance of $\text{BaO}(\text{g})$ and the lower partial pressures of MoO_3 and MoO_2 . This comparison supports a potential reduction of the BaMoO_4 sample during the KEMS measurement.

4.4 Reaction pathways

There are a variety of reaction pathways with which the gaseous species in figure 4.6 could have been created. These equations sum up all possibilities. The three dots represent all possibilities with $\text{MoO}_3(\text{g})$, $\text{MoO}_2(\text{g})$, $\text{Mo}(\text{g})$ and the corresponding amount of O_2 that have been covered by equations 4.4 and 4.5. Due to lacking thermodynamic knowledge of BaMoO_3 , it is not known whether this compound would melt under the conditions of the KEMS measurement (like the $\text{BaMoO}_4(\text{s})$ sample does), therefore it is depicted with a possible solid or liquid phase.



Knowing the composition of the KEMS sample after the measurement would have been very helpful to determine which of these reactions took place. Unfortunately it was not possible to do XRD analysis after the KEMS experiment, because all of the sample had evaporated. Therefore, it is not possible to determine which of these reactions occurred during the experiment. Since a KEMS apparatus is not present in the TU Delft facilities to do a repeat experiment, a TGDSC measurement was done with pure $\text{BaMoO}_4(\text{s})$ under both argon and oxygen up to 1673K (the highest possible temperature on the machine) to see if the sample had reduced.

4.5 TGDSC experiment BaMoO_4

Pure BaMoO_4 was tested in both an oxygen and argon atmosphere up to 1673K in one cycle with a heating rate of 10K/min and a cooling rate of 20K/min (more cycles were not possible due to time constraints). An oxygen atmosphere is an oxidising environment and argon is reducing, because it removes the presence of any oxidising agents. These two experiments should show the behaviour of $\text{BaMoO}_4(\text{s})$ in an oxidising and reducing environment and whether or not the sample reduces to BaMoO_3 .

Looking at the $\text{BaMoO}_4 - \text{MoO}_3$ phase diagram in figure 3.17, no events are expected to occur. However, both TGDSC measurements show a large peak at corrected onset temperatures of $1548.97 \pm 5 \text{ K}$ (Ar) and $1539.92 \pm 5 \text{ K}$ (O_2) (onset instead of peak-maximum temperatures, because they are significantly lower than the melting point (liquidus) of BaMoO_4 at 1734K [120]). These temperatures differ somewhat, but they were only recorded during one cycle. Multiple cycles would give temperatures with better statistical significance. The measurements are shown in figures 4.8 and 4.9. The event was not detected during the $\text{BaMoO}_4 - \text{MoO}_3$ pseudo binary section investigation, because the temperature limit of those measurements was 1008K. It is therefore unlikely to have had any effect on them.

Figure 4.8a and 4.8b show the heat flow of both measurements, as well as the sample temperature and the absolute weight loss of the sample. The weight loss curve of each measurement was corrected against the weight loss curve of a blank measurement with an empty TGDSC crucible, done under the same conditions as the BaMoO_4 measurements. Details on the weight change of the sample during the measurements is recorded in table 4.4. The weight of the sample under argon remained relatively constant over the whole cycle, but the weight of the O_2 sample first increased (heating cycle), then decreased significantly (cooling cycle). It is not unusual for the weight of the sample to fluctuate somewhat during a TGDSC cycle, but this amount of mass loss/ gain is significant. Weight loss can be associated with evaporation or reduction and weight gain with oxidation and of the sample. BaMoO_4

is not volatile and melts at 1743K [120], so evaporation seems unlikely. Oxidation is not possible, because the oxidation state of Mo_6^+ cannot be higher than what it is in BaMoO_4 . Reduction would be more logical, considering the results of the KEMS measurement, but this is not supported by the weight gain of the sample.

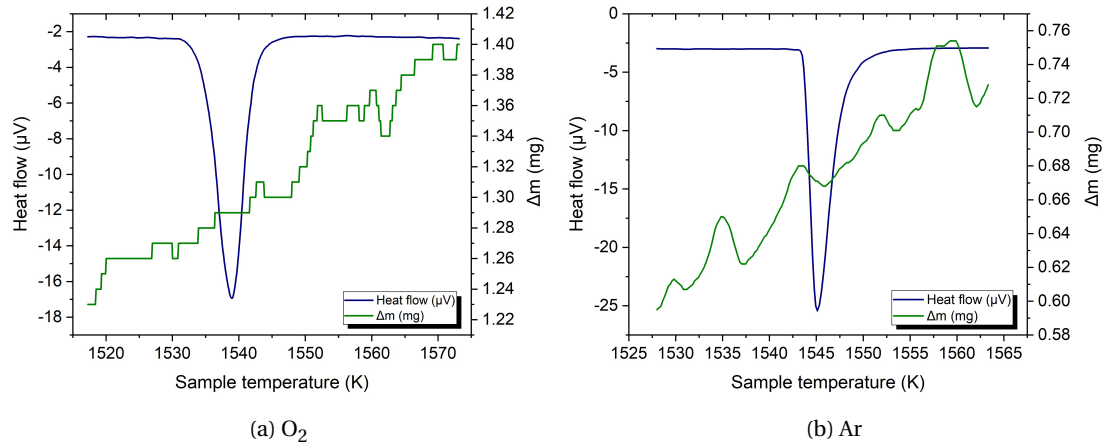


Figure 4.8: TGDSC measurement of $\text{BaMoO}_4(\text{s})$ with the sample temperature [K] and Δm [mg], which is equal to the sample mass curve minus the blank measurement mass curve in O_2 (a) and Ar (b) atmosphere.

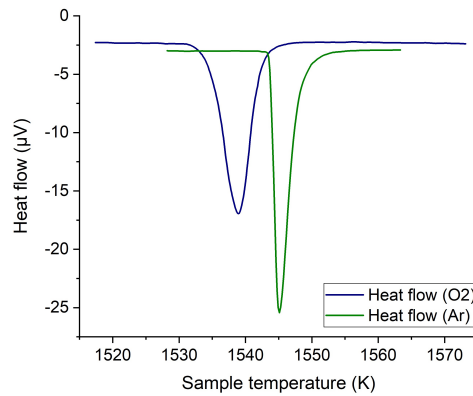


Figure 4.9: Both BaMoO_4 TGDSC measurements together with the sample temperature [K]

Table 4.4: Details on the weight change of the BaMoO_4 sample during both TGDSC measurements

| | Original sample mass (mg) | Heating cycle | | Cooling cycle | |
|--------------|---------------------------|-----------------------------|----------------|-----------------------------|----------------|
| | | Δm (%) ^a | Remaining (mg) | Δm (%) ^a | Remaining (mg) |
| O_2 | 67.01 | 2.61 | 68.76 | -9.83 | 60.42 |
| Ar | 62.05 | 1.81 | 63.17 | 0.48 | 62.35 |

^aCompared to the original sample mass

To see if the phases within either sample had changed, both of them were analysed via XRD and a subsequent Rietveld refinement. The results can be seen in figures 4.10a (O₂) and 4.10b (Ar). There are no unidentified peaks, which means that both samples contained only one phase after the TGDSC measurements: BaMoO₄. This result matches the paper by Pupp et al. [101], which also concluded that the sample only contained BaMoO₄ after XRD analysis. However, it does not explain the weight gain/ loss during the measurement, nor does it clarify the reason behind the second events of ionic species Ba⁺ and BaO⁺. It also does not show that the sample had (partially) reduced to BaMoO₃(s).

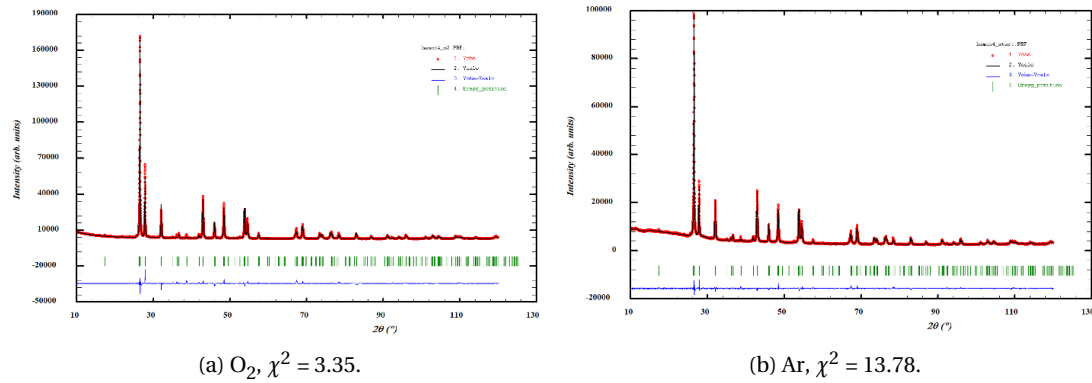


Figure 4.10: Rietveld analyses of the BaMoO₄ TGDSC measurement under O₂ (a) and Ar (b) atmospheres. Comparison between the observed (Y_{obs} , in red) and calculated (Y_{calc} , in black) X-ray diffraction patterns. $Y_{obs} - Y_{calc}$, in blue, is the difference between the experimental and calculated intensities. The Bragg's reflection angular positions are marked in green for each phase.

To see how likely a reduction of the BaMoO₄ sample would be during the KEMS experiment, some examples were found in literature. A study by Nassif et al. [88] investigated the reduction of BaMoO₄ and found that it reduces above 1193K in an environment of H₂/N₂ (5% / 95%) (figure 4.11) according to the following reaction when the sample was heated at 1423K for 12h:

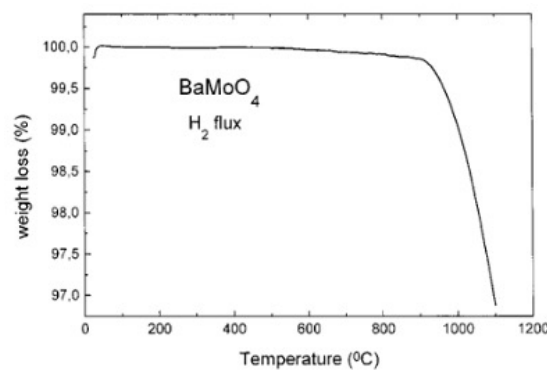
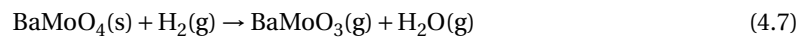


Figure 4.11: Weight loss curve during the reduction reaction of BaMoO₄(s) under H₂ as a function of temperature [°C] [88]

Xu et al. [139] also reduced BaMoO₄ via reaction (4.7), under a pure H₂ flow at 1173K for 3h, producing pure BaMoO₃. The reduction reaction by Nassif et al. [88] corresponded to a weight loss of 5.38%, which matches the stoichiometry of the reaction:

$$\frac{M_{\text{O}}}{M_{\text{BaMoO}_4}} = \frac{16.0 \text{ g/mol}}{297.3 \text{ g/mol}} = 5.38\% \quad (4.8)$$

It is clear that it is possible for BaMoO₄ to reduce at a temperature within the temperature range of the KEMS and TGDSC measurements (which were up to 2400K and 1673K respectively). Both examples from literature had a reducing agent present (H₂), which was also the case for the KEMS and the Ar TGDSC measurement. KEMS was performed under high-vacuum conditions, removing the influence of any interfering gaseous molecules (therefore also removing oxidising agents, which means that it is a reducing environment). From this it can be concluded that (partial) reduction of the BaMoO₄(s) sample was possible during the KEMS and Ar TGDSC measurement, but not likely during the O₂ TGDSC measurement.

It is recommended to perform additional measurements to determine what exactly happens to the BaMoO₄ sample during a KEMS experiment. Firstly, a repeat KEMS measurement should be done (up to the same temperature), but not all of the sample should be evaporated so that it can be quenched and analysed via XRD. Knowing the composition of the sample after the measurement would help to further interpret the appearance energy data. Also, a high-temperature XRD measurement under vacuum could shed more light onto the changes that the sample undergoes while it is heated. A repeat TGDSC measurement with more cycles would show if the event occurred during multiple cycles and would give a statistically relevant event temperature. It would also show the development of the weight curve over multiple cycles. A second KEMS measurement is also recommended where the sample is heated continuously (without the two constant temperature intervals) to produce continuous partial pressure curves.

Conclusion

A literature study into the ternary Ba-Sr-O system revealed that Ba and Sr, being chemically alike, are miscible into each other's oxide crystal lattices. The binary BaO – SrO system thus exhibits mutual solubility, although a miscibility gap is also present in the solid region. It was also shown that nonstoichiometric compounds Ba_xSr_yO can be formed. Three reported thermodynamic models were found of the binary BaO - SrO system, as well as accompanying thermodynamic functions and parameters. Peroxides in the binary Ba-O and Sr-O systems were reported to also present in the form of nonstoichiometric molecules BaO_{2-x} and SrO_{2-x} respectively. The binary Ba-Sr system does not form any compounds due to the mutual miscibility of Ba and Sr.

Syntheses of $BaMoO_4$, $BaMo_3O_{10}$, Ba_2MoO_5 and $BaCs_2(MoO_4)_2$ were successfully completed and the synthesis of Ba_3MoO_6 was only partially successful. The novel synthesis of Ba_2MoO_5 allowed for solution calorimetry measurements to be performed, leading to the determination of its standard enthalpy of formation: $\Delta_f H^\circ_m(298.15K, Ba_2MoO_5) = -(2169.0 \pm 14.7) \text{ kJ/mol}$.

TGDSC measurements in the $BaMoO_4 - MoO_3$ and $SrMoO_4 - MoO_3$ pseudo-binary systems were performed, but impeded by a temperature restriction caused by the evaporation of MoO_3 above 1008K. This limited the visibility of the liquidus line and only caused some ($BaMoO_4 - MoO_3$) or, unexpectedly, none ($SrMoO_4 - MoO_3$) liquidus events to be detected. This made it difficult to confirm the position of all invariant equilibria, in particular the eutectic equilibria. For both systems, the likely position of the eutectic equilibrium is similar to where the CALPHAD models had optimised them, between $0.792 \leq x(MoO_3) \leq 0.80$ for $BaMoO_4 - MoO_3$ and between $0.806 \leq x(MoO_3) \leq 0.82$ for $SrMoO_4 - MoO_3$.

A new CALPHAD model was developed of the $BaMoO_4 - Cs_2MoO_4$ pseudo-binary system based on TGDSC measurements with the novel quaternary $BaCs_2(MoO_4)_2$ compound. During these measurements it was found that the decomposition of $BaCs_2(MoO_4)_2$ during the first cycle was not reversed after cooling, and that hence only first-cycle results could be used (which led to data that is not statistically relevant). Due to outlying data points and possibly the visible melting peak of Cs_2MoO_4 at high content of $x(Cs_2MoO_4)$, no clear invariant equilibria could be formulated. It is likely that a eutectic equilibrium occurs in the region between $0.909 \leq x(Cs_2MoO_4) \leq 0.976$. The optimised standard entropy and standard enthalpy of formation of the quaternary compound in the CALPHAD model with the best fit to phase diagram data, deviate from the uncertainty margins set in literature. The CALPHAD model based on values within these margins fits the experimental phase diagram data points poorly.

A literature study into vapour pressure studies of $BaMoO_4$ presented two separate papers that had performed KEMS measurements. These studies reported different outcomes with regard to relative ion intensities, but both reported congruent vaporisation of the $BaMoO_4$ sample. The KEMS measurement data analysed in this thesis on the other hand, showed extensive fragmentation of the ions

and only a small amount of congruent vaporisation. The gaseous parent species of most ions could be allocated, however the second-event appearance energies of both Ba^+ and BaO^+ did not match ionisation energies found in literature. Two scenarios were considered during partial pressure calculations, in which Ba^+ and BaO^+ came from $\text{BaMoO}_3(\text{g})$ and $\text{BaMoO}_4(\text{g})$, respectively, for scenario 1, and vice versa for scenario 2. For both scenarios, the partial pressure of $\text{BaMoO}_3(\text{g})$ was higher than $\text{BaMoO}_4(\text{g})$. The partial pressure of BaMoO_3 was lower than the (unchanged) partial pressure of $\text{BaO}(\text{g})$ for scenario 2, whereas the partial pressure of $\text{BaMoO}_4(\text{g})$ was lower than that of $\text{BaO}(\text{g})$ for both scenarios. The high partial pressure of $\text{BaO}(\text{g})$ suggests a high influence of dissociation reactions by either $\text{BaMoO}_4(\text{g})$ or $\text{BaMoO}_3(\text{g})$. Due to the large presence of $\text{BaMoO}_3(\text{g})$, it is possible that the BaMoO_4 sample partially reduced to BaMoO_3 during the measurement. Without knowing the final composition of the KEMS sample, it is not possible to determine conclusively which scenario is true, and unfortunately that sample evaporated completely.

To test the behaviour of BaMoO_4 at high temperature conditions, TGDSC studies were done with pure BaMoO_4 under O_2 and Ar, for 1 cycle up to 1673K. Both measurements showed an unexpected (and previously unrecorded) event that has unexplained weight gain that was checked against blank measurements. XRD analysis of both samples after TGDSC showed pure BaMoO_4 . The results of these TGDSC measurements should be disregarded, since they are unprecedented and unexplained, and since the measurements could not be repeated to check their validity.

Recommendations

Chapter 1 - Literature review

Vapour pressure studies (by means of KEMS measurements) on the $(1-x)\text{BaO} + x\text{SrO}$ system would clarify the volatility and relative intensities of the Sr^{2+} and Ba^{2+} ions.

Chapter 3 - Experimental, results and discussion

It is recommended to try a lower temperature of 1173 or 1073K for the synthesis of Ba_3MoO_6 , with an XRD and Rietveld analysis after each cycle. Due to the lower temperature more than 2 cycles could be needed to complete the synthesis.

In order to calculate a statistically relevant value for the standard enthalpy of formation of Ba_2MoO_5 , an additional 5 solution calorimetry experiments should be performed with both BaO and BaMoO_4 .

To remove the 1008K temperature limitation of the $\text{BaMoO}_4 - \text{MoO}_3$ and $\text{SrMoO}_4 - \text{MoO}_3$ TGDSC measurements, a method should be found to eliminate the evaporation of MoO_3 , for example by using an encased DSC crucible. It is also recommended to buy new BN, MoO_3 and SrMoO_4 , to test them with a DSC and to use them for future experiments.

More $\text{BaMoO}_4 - \text{MoO}_3$ TGDSC measurements are needed at higher values of $x(\text{MoO}_3)$ and at a higher temperature, to corroborate the position of the liquidus line. More measurements also need to be done around $0.82 \leq x(\text{MoO}_3) \leq 0.845$ to determine how many events occur there and what they represent, preferably at a higher temperature than 1008K to ensure that the liquidus events are recorded.

It is strongly recommended to find a method to achieve a 4-cycle measurement for $\text{BaMoO}_4 - \text{Cs}_2\text{MoO}_4$ TGDSC experiments, because this would eliminate first cycle noise and would give statistically significant data. Possibly using very low cooling rates to give the decomposed $\text{BaCs}_2(\text{MoO}_4)_2$ more time to reassemble before the next heating cycle. This can be combined with an encased DSC crucible to prevent some of the weight loss at higher $x(\text{Cs}_2\text{MoO}_4)$ values. Multiple 1-cycle measurements of the same composition would also provide more clarity, but this does not eliminate the 1st cycle noise. Lower heating rates at higher $x(\text{Cs}_2\text{MoO}_4)$ values would help to separate the large amount of event peaks in that area.

Chapter 4 - Vapour pressure studies: results and discussion

Two repeat KEMS measurements with $\text{BaMoO}_4(\text{s})$ should be performed using the JRC Karlsruhe facilities (up to the same temperature and using the same ionisation energy). One measurement with temperature intervals (at the same temperatures 1886 and 2192K during which the ionisation energy is varied) and one without, so that the calculated partial pressure curves are continuous. The sample

should not be evaporated completely and subsequently quenched it so that the composition of the sample may be analysed by means of XRD (and possibly microscopic analysis). This will show if a reduction to BaMoO_3 has taken place.

A high temperature XRD measurement under vacuum could shed more light onto the changes that the sample undergoes while it is heated (and thus if reduction occurs). This experiment would mimic some of the conditions of the KEMS experiment.

More thermodynamic investigations into BaMoO_3 are needed to discover how the compound behaves under the KEMS measurement conditions and if it would have melted.

New pure $\text{BaMoO}_4(\text{s})$ TGDSC measurements under Ar and O_2 are needed with 4 cycles. This will show the development of the weight curve and the possible recurrence of the event over multiple cycles. Both measurements should be accompanied by a blank measurement so that the weight gain might be accurately accessed.

Bibliography

- [1] Effusion and diffusion of gases. https://opentextbc.ca/chemistry/chapter/9-4-effusion-and-diffusion-of-gases/of_Diffusion_and_Effusion.
- [2] TAM III precision solution calorimeter and solcal software - user manual. Technical report, TA Instruments, 2 2012.
- [3] Graham's laws of diffusion and effusion, 9 2020. [https://chem.libretexts.org/Bookshelves/Physical_and_Theoretical_Chemistry_Textbook_Maps/Map%3A_Physical_Chemistry_for_the_Biosciences_\(Chang\)/02%3A_Properties_of_Gases/2.9%3A_Graham%27s_Laws_of_Diffusion_and_Effusion](https://chem.libretexts.org/Bookshelves/Physical_and_Theoretical_Chemistry_Textbook_Maps/Map%3A_Physical_Chemistry_for_the_Biosciences_(Chang)/02%3A_Properties_of_Gases/2.9%3A_Graham%27s_Laws_of_Diffusion_and_Effusion).
- [4] Powder x-ray diffraction, 8 2020. [https://chem.libretexts.org/Bookshelves/Analytical_Chemistry/Supplemental_Modules_\(Analytical_Chemistry\)/Instrumental_Analysis/Diffraction_Scattering_Techniques/Powder_X-ray_Diffraction](https://chem.libretexts.org/Bookshelves/Analytical_Chemistry/Supplemental_Modules_(Analytical_Chemistry)/Instrumental_Analysis/Diffraction_Scattering_Techniques/Powder_X-ray_Diffraction).
- [5] Mass analyzers (mass spectrometry), 5 2021. [https://chem.libretexts.org/Bookshelves/Analytical_Chemistry/Supplemental_Modules_\(Analytical_Chemistry\)/Instrumental_Analysis/Mass_Spectrometry/Mass_Spectrometers_\(Instrumentation\)/Mass_Analyzers_\(Mass_Spectrometry\)](https://chem.libretexts.org/Bookshelves/Analytical_Chemistry/Supplemental_Modules_(Analytical_Chemistry)/Instrumental_Analysis/Mass_Spectrometry/Mass_Spectrometers_(Instrumentation)/Mass_Analyzers_(Mass_Spectrometry)).
- [6] Solid state synthesis, 2022. <https://www.sigmaaldrich.com/NL/en/applications/materials-science-and-engineering/solid-state-synthesis>.
- [7] L.T. Aldrich. The evaporation products of barium oxide from various base metals and of strontium oxide from platinum. *Journal of Applied Physics*, 22:1168–1174, 1951.
- [8] P. Atkins and J. De Paula. *Physical Chemistry*. W.H. Freeman and Company, ninth edition, 2010.
- [9] P. Aursand, M.A. Gjennestad, E. Aursand, M. Hammer, and Ø. Wilhelmsen. The spinodal of single- and multi-component fluids and its role in the development of modern equations of state. *Fluid Phase Equilibria*, 436:98–112, 3 2017.
- [10] P. Benigni, G. Mikaelian, E. Ruiz, C. Perrin-Pellegrino, and J. Rogez. Calorimetric determination of the formation enthalpies of Cs polymolybdates at 298.15 K and 0.1 MPa. *Journal of Chemical and Engineering Data*, 65:3875–3883, 8 2020.
- [11] M. Benjamin and H.P. Rooksby. LXV. emission from oxide-coated cathodes. *The London, Edinburgh, and Dublin Philosophical Magazine and Journal of Science*, 15:810–829, 4 1933.
- [12] J.C. Bernède, L. Cattin, and M. Morsli. About MoO₃ as buffer layer in organic optoelectronic devices. *Technology Letterd*, 1:5–17, 2014.

- [13] B.O. Boehm, S. Rosinger, D. Belyi, and J.W. Dietrich. The parathyroid as a target for radiation damage. *The New England Journal of Medicine*, 365:676–678, 2011.
- [14] G. Brillant. Interpretation and modelling of fission product Ba and Mo releases from fuel. *Journal of Nuclear Materials*, 397:40–47, 2 2010.
- [15] E.C. Buck, B.D. Hanson, and B.K. Mcnamara. The geochemical behaviour of Tc, Np and Pu in spent nuclear fuel in an oxidizing environment. *Geological Society*, 236:65–88, 2004.
- [16] W.G. Burgers. Röntgenographische untersuchung des verhaltens von BaO-SrO-gemischen beim glühen. *Zeitschrift für Physik*, 80:352–360, 1933.
- [17] S.R. Byrn, G. Zografi, and X. Chen. *Differential Scanning Calorimetry and Thermogravimetric Analysis*, chapter 10, pages 124–141. John Wiley, first edition, 6 2017.
- [18] J.E. Campbell, G.K. Murthy, A.S. Goldin, H.B. Robinson, C.P. Straub, F.J. Weber, and K.H. Lewis. The occurrence of strontium-90, iodine-131 and other radionuclides in milk. *American Journal of Public Health*, 49:225–235, 1959.
- [19] H. Cember and J.A. Watson. Carcinogenic effects of strontium 90 beads implanted in the lungs of rats. *American Industrial Hygiene Association Journal*, 19:36–42, 2 1958.
- [20] A. Claassen and C.F. Veenemans. Dampfdruckbestimmungen von BaO, SrO, CaO und deren mischungen aus verdampfungsgeschwindigkeitsmessungen. *Zeitschrift für Physik*, 80:342–351, 1933.
- [21] P. Clausing. The flow of highly rarefied gases through tubes of arbitrary length. *Journal of Vacuum Science and Technology*, 8:636–646, 12 1971.
- [22] M.W.D. Cooper, S.C. Middleburgh, and R.W. Grimes. Partition of soluble fission products between the grey phase, ZrO₂ and uranium dioxide. *Journal of Nuclear Materials*, 438:238–245, 2013.
- [23] M.W.D. Cooper, S.C. Middleburgh, and R.W. Grimes. Swelling due to the partition of soluble fission products between the grey phase and uranium dioxide. *Progress in Nuclear Energy*, 72:33–37, 2014.
- [24] E.H.P. Cordfunke, A.S. Booi, V. Smit-Groen, P. van Vlaanderen, and D.J.W. IJdo. Structural and thermodynamic characterization of the perovskite-related Ba_{1+y}UO_{3+x} and (Ba, Sr)_{1+y}UO_{3+x} phases. *Journal of Solid State Chemistry*, 131:341–349, 1997.
- [25] Advanced Lab Course. High-resolution x-ray diffraction. Technical report, Technical University of Munich, 10 2020.
- [26] S. Dash, Z. Singh, R. Prasad, and V. Venugopal. Computer calculation of the 700K isothermal section of the Ba-Mo-O system from thermodynamic data. *High Temperatures - High Pressures*, 32:215–225, 2000.
- [27] N.H.C. de Zoete. Fission products chemistry and scenario analysis of severe accident progression at fukushima-daiichi nuclear power station: investigation of the Ba-Sr-Cs-Mo-O system, October 2018. TU Delft, Bachelor thesis.
- [28] G. DeMaria, R.P. Burns, J. Drowart, and M.G. Inghram. Mass spectrometric study of gaseous molybdenum, tungsten, and uranium oxides. *J. Chem. Phys.*, 32:1373–1377, 1960.

- [29] H. Deutsch, K. Becker, R. Basner, M. Schmidt, and T. D. Märk. Application of the modified additivity rule to the calculation of electron-impact ionization cross sections of complex molecules. *J. Phys. Chem. A.*, 102:8819–8826, 11 1998.
- [30] H. Deutsch, K. Becker, and T.D. Märk. A modified additivity rule for the calculation of electron impact ionization cross-section of molecules AB_n . *International Journal of Mass Spectrometry and Ion Processes*, 167:503–517, 1997.
- [31] H. Deutsch, C. Cornelissen, L. Cespiva, V. Bonacic-Koutecky, D. Margreiter, and T.D. Märk. Total electron impact ionization cross sections of free molecular radicals: the failure of the additivity rule revisited. *International Journal of Mass Spectrometry and Ion Processes*, 129:43–48, 1993.
- [32] Dieke and Frederlitse. *American Institute of Physics Handbook*. 1963.
- [33] A.T. Doig. Baritosis: a benign pneumoconiosis. *Thorax*, 31:30–39, 1976.
- [34] J. Drowart, C. Chatillon, J. Hastie, and D. Bonnell. High-temperature mass spectrometry: Instrumental techniques, ionization cross-sections, pressure measurements, and thermodynamic data (iupac technical report). *Pure and Applied Chemistry*, 77:683–737, 4 2005.
- [35] G. Ducros, P.P. Malgouyres, M. Kissane, D. Boulaud, and M. Durin. Fission product release under severe accidental conditions: general presentation of the program and synthesis of VERCORS 1-6 results. *Nuclear Engineering and Design*, 208:191–203, 2001.
- [36] J.M. Dyke, M. Fehér, B.W.J. Gravenor, and A. Morris. High-temperature photoelectron spectroscopy: A study of the alkaline earth oxides SrO and BaO. *J. Am. Chem. Soc.*, 91:4476–4481, 1987.
- [37] I. Efthimiopoulos, K. Kunc, S. Karmakar, K. Syassen, M. Hanfland, and G. Vajenine. Structural transformation and vibrational properties of BaO_2 at high pressures. *Phys. Rev. B*, 82, 10 2010.
- [38] R.J.M. Konings E.H.P. Cordfunke. Thermochemical data for reactor materials and fission products; thermochemical data for reactor materials and fission products, 1990.
- [39] A. Eisenstein. A study of oxide cathodes by X-ray diffraction methods: Part I. methods, conversion studies, and thermal expansion coefficients. *Journal of Applied Physics*, 17:434–443, 1946.
- [40] G.V. Flidlidze, T.V. Kovtunencko, E.V. Kiseleva, and A.A. Bundel. The relation between the heats of formation of solid solutions of alkaline earth metal oxides and their capacity for thermionic emission. *Russian Journal of Physical Chemistry*, 40:1329–1331, 1966.
- [41] Centers for Disease Control and Prevention. Molybdenum (soluble compounds, as Mo), 12 2014.
- [42] H. Gaertner. VI. electron diffraction on oxide-coated filaments. *The London, Edinburgh, and Dublin Philosophical Magazine and Journal of Science*, 19:82–103, 1 1935.
- [43] C. Le Gall, E. Geiger, A. Gallais-During, Y. Pontillon, J. Lamontagne, E. Hanus, and G. Ducros. Fission products and nuclear fuel behaviour under severe accident conditions part 3: Speciation of fission products in the VERDON-1 sample. *Journal of Nuclear Materials*, 495:291–298, 11 2017.
- [44] E.J. Huber G.C. Fitzgibbon and C.E. Holley. The enthalpy of formation of barium monoxidet. *J. Chem. Thermodynamics*, 5:577–582, 1973.

- [45] E. Geiger, C. Guéneau, Y. Pontillon, and E.C. Corcoran. Modelling nuclear fuel behaviour with TAF-ID: Calculations on the VERDON-1 experiment, representative of a nuclear severe accident. *Journal of Nuclear Materials*, 522:294–310, 8 2019.
- [46] V.B. Goncharov and E.F. Fialko. Structure and reactivity of gas-phase molybdenum oxide cluster ions. *Journal of Structural Chemistry*, 43:777–782, 2002.
- [47] W. Gong and Z. Jin. Thermodynamic description of BaO-SrO-TiO₂ system. *Calphad*, 26:403–418, 2002.
- [48] V.B. Grebenyuk, I.V. Kavich, O.G. Mikolaichuk, and I.T. Romanchuk. *Ukr. Phys. J.*, 12, 1967.
- [49] J.-C. Grivel. Subsolidus phase relations of the SrO-Ta₂O₅-CuO system at 900°C in air. *Journal of Alloys and Compounds*, 486:293–298, 11 2009.
- [50] C. Guéneau, M. Asta, and B. Sundman. *Computational Thermodynamics: Application to Nuclear Materials*, volume 1, chapter 1, pages 814–847. Elsevier, second edition, 2020.
- [51] C. Guéneau, N. Dupin, L. Kjellqvist, E. Geiger, M. Kurata, S. Gossé, E. Corcoran, A. Quaini, R. Hania, A. L. Smith, M. H.A. Piro, T. Besmann, P. E.A. Turchi, J. C. Dumas, M. J. Welland, T. Ogata, B. O. Lee, J. R. Kennedy, C. Adkins, M. Bankhead, and D. Costa. TAF-ID: An international thermodynamic database for nuclear fuels applications. *CALPHAD*, 72, 3 2021.
- [52] H.K. Hardy. A "sub-regular" solution model and its application to some binary alloy systems. *Acta Metallurgica*, 1:202–209, 1953.
- [53] L. Herrmann. Fission product chemistry of the Ba-Mo-O system for the safety assessment of the behaviour of nuclear fuel, January 2020. TU Delft, Bachelor thesis.
- [54] M. Heyrman, C. Chatillon, H. Collas, and J. L. Chemin. Improvements and new capabilities for the multiple knudsen cell device used in high-temperature mass spectrometry. *Rapid Communications in Mass Spectrometry*, 18:163–174, 2004.
- [55] Z. Hiezl, D.I. Hambley, C. Padovani, and W.E. Lee. Processing and microstructural characterisation of a UO₂-based ceramic for disposal studies on spent AGR fuel. *Journal of Nuclear Materials*, 456:74–84, 2015.
- [56] H.R. Hoekstra. The Cs₂MoO₄ - MoO₃ system. *Inorg. Nucl. Chem. Lett.*, 9:1291–1301, 12 1973.
- [57] S. Imoto. Chemical state of fission products in irradiated UO₂. *Journal of Nuclear Materials*, 140:19–27, 1986.
- [58] D. Sedmidubský J. Leitner, P. Voňka and P. Svoboda. Application of neumann-kopp rule for the estimation of heat capacity of mixed oxides. *Thermochimica Acta*, 497:7–13, 1 2010.
- [59] K.T. Jacob and V. Varghese. Solid-state miscibility gap and thermodynamics of the system BaO-SrO. *J. Mater. Chem.*, 5:1059–1062, 1995.
- [60] N. Jacobson, D. Kobertz, and D. Sergeev. Introduction to proceedings of the workshop on knudsen effusion mass spectrometry. *Calphad*, 65:111–126, 6 2019.
- [61] N.S. Jacobson, E.H. Copland, G.M. Mehrotra, and J. Auping. *Knudsen cell studies of Ti-Al thermodynamics*, volume 5, pages 226–232. The Electrochemical Society, INC., 2002.
- [62] J.L. Jorda and T.K. Jondo. Barium oxides: equilibrium and decomposition of BaO₂. *Journal of Alloys and Compounds*, 327:167–177, 2001.

- [63] H. Karlsson and U. Litzén. Revised Ba I and Ba II wavelengths and energy levels derived by fourier transform spectroscopy. *Phys. Scr.*, 60:321–328, 1999.
- [64] G. Kauric. Presentation: Interactions between sodium and fission products in case of a severe accident in a sodium-cooled fast reactor. *GEN-IV International Forum*, 2019. <https://www.youtube.com/watch?v=vmJlXb61kb8&t=2077s>.
- [65] G. Kauric, E. Epifano, P.M. Martin, L. van Eijck, D. Bouëxière, N. Clavier, C. Guéneau, and A.L. Smith. Structural and thermodynamic investigation of the perovskite $\text{Ba}_2\text{NaMoO}_5 \cdot 5$. *Inorganic Chemistry*, 59:6120–6130, 5 2020.
- [66] O.V. Kedrovskii, I.V. Kovtunenkov, E.V. Kiseleva, and A.A. Bundel. Interaction of oxygen with alkaline earth metal oxides. I. equilibria in the system barium oxide - oxygen at pressures close to atmospheric. *Russ. J. Phys. Chem.*, 41:205–208, 1967.
- [67] H. Kleykamp. The chemical state of the fission products in oxide fuels. *Journal of Nuclear Materials*, 131:221–246, 1985.
- [68] H. Kleykamp, J.O. Paschoal, R. Pejasa, and F. Thommler. Composition and structure of fission product precipitates in irradiated oxide fuels: correlation with phase studies in the Mo-Ru-Rh-Pd and BaO-UO₂-ZrO₂-MoO₂ systems. *Journal of Nuclear Materials*, 130:426–433, 1985.
- [69] C. F. Knights and B. A. Phillips. The Cs-O system; phase diagram and oxygen potentials. *Journal of Nuclear Materials*, 84:196–206, 1979.
- [70] M. Koitabashi. Mass spectrum of barium oxide vapor. *Jpn. J. Appl. Phys.*, 33:5995–6000, 1994.
- [71] V.N. Kondratev. Bond breakage energy. ionisation potentials and electron affinity [in russian], 1974.
- [72] R. Koningsveld, W.H. Stockmayer, and E. Nies. *Polymer Phase Diagrams: A Textbook*. Oxford University Press, 2001.
- [73] A. Kovács and R.J.M. Konings. Molecular data of mixed metal oxides with importance in nuclear safety. *Journal of Nuclear Materials*, 477:134–138, 8 2016.
- [74] U. Kramar. *X-ray fluorescence spectrometers*, pages 695–706. Elsevier, third edition, 9 2016.
- [75] M. Kröger, S. Hamwi, J. Meyer, T. Riedl, W. Kowalsky, and A. Kahn. Role of the deep-lying electronic states of MoO₃ in the enhancement of hole-injection in organic thin films. *Appl. Phys. Lett.*, 95, 2009.
- [76] M. Königstein. Structural properties of nonstoichiometric barium and strontium peroxides: BaO_{2-x} (1.97 ≥ 2 - x ≥ 1.72) and SrO_{2-x} (1.98 ≥ 2 - x ≥ 1.90). *Journal of Solid State Chemistry*, 147:478–484, 1999.
- [77] B.Y. Lalit, T.V. Ramachandran, and S. Rajan. Strontium-90 and caesium in indian tea. *Radiat Environ Biophys*, 22:75–83, 1983.
- [78] J. Leitner, P. Chuchvalec, D. Sedmidubský, A. Strejc, and P. Abrman. Estimation of heat capacities of solid mixed oxides. *Thermochimica Acta*, 395:27–46, 1 2002.
- [79] S. Levine, G.D. Kaiser, W.C. Arcieri, H. Firstenberg, P.J. Fulford, P.S. Lam, R.L. Ritzman, and E.R. Schmidt. Source terms: an investigation of uncertainties, magnitudes, and recommendations for research, 3 1982.

- [80] S.G. Lias, J.E. Bartmess, J.F. Liebman, J.L. Holmes, R.D. Levin, and W.G. Mallard. Gas-phase ion and neutral thermochemistry. *J. Phys. Chem.*, 1988.
- [81] D.R. Lide. *CRC Handbook of Chemistry and Physics*. CRC Press, 73 edition, 1992.
- [82] H.-P. Looock, B. Simard, S. Wallin, and C. Linton. Ionization potentials and bond energies of TiO, ZrO, NbO and MoO. *J. Chem. Phys.*, 109:8980–8992, 1998.
- [83] X. Lu and Z. Jin. Thermodynamic assessment of the BaO-TiO₂ quasi binary system. *Calphad*, 24:319–338, 2001.
- [84] P.G. Lucuta, R.A. Verrall, H. Matzke, and B.J. Palmer. Microstructural features of SIMFUEL-simulated high-burnup UO₂-based nuclear fuel. *Journal of Nuclear Materials*, 178:48–60, 1991.
- [85] F.A. Mellon. *Mass Spectrometry*, pages 3739–3749. Elsevier, second edition, 2003.
- [86] E. Murad. Thermochemical properties of the gaseous alkaline earth monohydroxides. *J. Chem. Phys.*, 75:4080–4085, 1981.
- [87] Z. Naima, T. Siro, G.-D. Juan-Manuel, C. Chantal, C. Rene, and D. Jerome. Interactions between carbamazepine and polyethylene glycol (PEG) 6000: characterisations of the physical, solid dispersed and eutectic mixtures. *European Journal of Pharmaceutical Sciences*, 12:395–404, 2001.
- [88] V. Nassif, R.E. Carbonio, and J.A. Alonso. Neutron diffraction study of the crystal structure of BaMoO₄: A suitable precursor for metallic BaMoO₃ perovskite. *Journal of Solid State Chemistry*, 146:266–270, 1999.
- [89] M.A. Andrianov O.A. Ustinov, G.P. Novoselov and N.T. Chebotarev. The MoO₃ - BaO system. *Russ. J. Inorg. Chem.*, 9:1320–1321, 1970.
- [90] Division of Toxicology and Human Health Sciences. Public health statements, 2 2021.
- [91] H. Okamoto. Cs-O (cesium-oxygen). *Journal of Phase Equilibria and Diffusion*, 31:86–87, 2 2010.
- [92] S. Ono and K. Kanaya. The energy dependence of secondary emission based on the range-energy retardation power formula. *J. Phys. D: Appl. Phys.*, 12:619–632, 1979.
- [93] E.P. Ostapchenko. X-ray investigation of the systems of binary and ternary carbonates and oxides of the alkaline earth metals. *Russ. Acad. Sci.*, 20:997–1003, 1956.
- [94] V.D. Ozrin. A model for evolution of oxygen potential and stoichiometry deviation in irradiated UO₂ fuel. *Journal of Nuclear Materials*, 419:371–377, 12 2011.
- [95] B.-O. Marinder P-E Werner, M. Moustiakimov and K. S. Knight. Crystal structure of BaMo₃O₁₀ solved from powder diffraction data. *Zeitschrift für Kristallographie*, 212:665–670, 1997.
- [96] S. C. Parida, S. Dash, Z. Singh, R. Prasad, and V. Venugopal. Thermodynamic studies on uranium - molybdenum alloys. *J. Phys. Chem. Solids*, 62:585–597, 2001.
- [97] P. Patnaik. *Handbook of Inorganic Chemicals*. McGraw-Hill Professional, 1 edition, 2002.
- [98] D.L. Perry. *Handbook of Inorganic Compounds*. Taylor & Francis Group, 2011.
- [99] B.D. Pierson, L.R. Greenwood, M. Flaska, and S.A. Pozzi. Fission product yields from ²³²Th, ²³⁸U, and ²³⁵U using 14 MeV neutrons. *Nuclear Data Sheets*, 139:171–189, 1 2017.

- [100] B.H. Post, W. Vassen, W. Hogervorst, M. Aymar, and O. Robaux. Odd-parity rydberg levels in neutral barium: term values and multichannel quantum defect theory analysis. *J. Phys. B: At. Mol. Phys.*, 18:187–206, 1985.
- [101] C. Pupp, R. Yamdagni, and R.F. Porter. Mass spectrometric study of the evaporation of BaMoO₄ and BaWO₄. *J. Inorg. Nucl. Chem.*, 31:2021–2029, 1969.
- [102] L. Qiu and M.A. White. The constituent additivity method to estimate heat capacities of complex inorganic solids. *Journal of Chemical Education*, 78:1076, 8 2001.
- [103] J.P. Besse R. Sabatier, M. Wathle and G. Baud. Sur les pérovskites oxygénées A₃BO₆ (A = Ba, Sr; B = W, Mo). *C.R. Seances Acad. Sci., Ser. C*, 271:368–371, 1970.
- [104] K.-J. Range, F. Rau, U. Schießl, and U. Klement. Verfeinerung der kristallstruktur von SrO₂. *Z. Anorg. Allg. Chem*, 620:879–881, 1994.
- [105] D.M. Rayner, S.A. Mitchell, L. Bourne, and P.A. Hackett. First-ionization potential of niobium and molybdenum by double-resonance, field-ionization spectroscopy. *J. Opt. Soc. Am. B*, 4:900–905, 1987.
- [106] J. Rest and A.W. Cronenberg. Modelling the behaviour of Xe, I, Cs, Te, Ba, and Sr in solid and liquefied fuel during severe accidents. *Journal of Nuclear Materials*, 150:203, 1987.
- [107] D. Risold, B. Hallstedt, and L.J. Gauckler. The strontium - oxygen system. *Calphad*, 20:353–361, 1996.
- [108] E.H.P. Cordfunke R.J.M. Konings. Chemical interactions in water-cooled nuclear fuel: A thermochemical approach. *Journal of Nuclear Materials*, 152:301–309, 1988.
- [109] T. Roisnel and J. Rodríguez-Carvajal. WinPLOTR: a windows tool for powder diffraction patterns analysis. Technical report, Materials Science Forum, 2001.
- [110] R.S. Roth, C.J. Rawn, J.D. Whitler, C.K. Chiang, and W.K. Wong-Ng. Phase equilibria and crystal chemistry in the quaternary system Ba-Sr-Y-Cu-O in air. *J. Am. Ceram. Soc.*, 72:395–399, 1989.
- [111] M. Rutten. Thermodynamic characterization of nuclear fission products: A study into the Ba-Sr-Cs-Mo-O system, October 2019. Master thesis.
- [112] L.M.N.B.F. Santos, A.I.M.C., L. Ferreira, V. Štejfa, A.S.M.C. Rodrigues, M.A.A. Rocha, M.C. Torres, F.M.S. Tavares, and E.S. Carpinteiro. Development of the knudsen effusion methodology for vapour pressure measurements of low volatile liquids and solids based on a quartz crystal microbalance. *Journal of Chemical Thermodynamics*, 126:171–186, 11 2018.
- [113] C Sari and C.T. Walker. Solubility and migration of fission product barium in oxide fuel. *Journal of Nuclear Materials*, 79:255–259, 1979.
- [114] N. Saunders and A.P. Miodownik. *Thermodynamic Models for Solution and Compound Phases*, volume 1, chapter 5, pages 91–126. Elsevier Science Ltd., 1998.
- [115] P.O. Schissel and O.C. Trulson. Mass-spectrometric study of the oxidation of tungsten. *J. Chem. Phys.*, 43:737–743, 1965.
- [116] Shoemaker and Garland. Knudsen effusion. Technical report, McGraw-Hill, 11 2002.
- [117] M.R. Sievers, Y.-M. Chen, and P.B. Armentrout. Metal oxide and carbide thermochemistry of Y⁺, Zr⁺, Nb⁺, and Mo⁺. *J. Chem. Phys.*, 105:6322–6333, 1996.

- [118] A. L. Smith, G. Kauric, L. van Eijck, K. Goubitz, G. Wallez, J. C. Griveau, E. Colineau, N. Clavier, and R. J.M. Konings. Structural and thermodynamic study of dicesium molybdate $\text{Cs}_2\text{Mo}_2\text{O}_7$: Implications for fast neutron reactors. *Journal of Solid State Chemistry*, 253:89–102, 9 2017.
- [119] A. L. Smith, M. C. Pignié, L. van Eijck, J. C. Griveau, E. Colineau, and R. J.M. Konings. Thermodynamic study of $\text{Cs}_3\text{Na}(\text{MoO}_4)_2$: Determination of the standard enthalpy of formation and standard entropy at 298.15k. *Journal of Chemical Thermodynamics*, 120:205–216, 5 2018.
- [120] A. L. Smith, M. Rutten, L. Herrmann, E. Epifano, R. J.M. Konings, E. Colineau, J. C. Griveau, C. Guéneau, and N. Dupin. Experimental studies and thermodynamic assessment of the Ba-Mo-O system by the CALPHAD method. *Journal of the European Ceramic Society*, 2021.
- [121] A. L. Smith, J. Vlieland, M. C. Pignié, M. Abbink, G. Mikaelian, and P. Benigni. New insights into the Cs-Mo-O system: Experimental studies of the Cs_2MoO_4 - MoO_3 pseudo-binary system. *Thermochimica Acta*, 696, 2 2021.
- [122] A.L. Smith. *Structural and Thermodynamic Properties of Sodium Actinide Ternary Oxides*. PhD thesis, University of Cambridge, 5 2015.
- [123] A.L. Smith, N. De Zoete, M. Rutten, L. Van Eijck, J. Christophe Griveau, and E. Colineau. Report of the double-molybdate phase $\text{Cs}_2\text{Ba}(\text{MoO}_4)_2$ with a palmierite structure and its thermodynamic characterization. *Inorganic Chemistry*, 59:13162–13173, 9 2020.
- [124] F.E. Stafford and J. Berkowitz. Mass-spectrometric study of the reaction of water vapor with solid barium oxide. *J. Chem. Phys.*, 40:2963–2969, 1964.
- [125] V.L. Stolyarova. Review: previous experimental data on vaporisation of Ba-bearing compounds by high temperature mass spectrometric method, 2019.
- [126] A. Strang. Effusion, 5 2012. <https://en.wikipedia.org/wiki/Effusion#/media/File:Effusion.svg>.
- [127] T.M. Sugden. Excited species in flames. *Annu. Rev. Phys. Chem.*, 13:369–390, 1962.
- [128] B. Sundman, X. Gang Lu, and H. Ohtani. The implementation of an algorithm to calculate thermodynamic equilibria for multi-component systems with non-ideal phases in a free software. *Computational Materials Science*, 101:127–137, 4 2015.
- [129] F. Takeiri, A. Watanabe, A. Kuwabara, H. Nawaz, N.I.P. Ayu, M. Yonemura, R. Kanno, and G. Kobayashi. Ba_2SCHO_3 : H^- conductive layered oxyhydride with H^- site selectivity. *Inorganic Chemistry*, 58:4431–4436, 4 2019.
- [130] V.M. Zhukovskii T.M. Yanushkevich and T.F. Telnykh. Phase diagram of the MoO_3 - SrO system. *Inorg. Mater. (Engl. Transl.*, pages 1794–1795, 1 1972.
- [131] M.J. Tribelhorn and M.E. Brown. Thermal decomposition of barium and strontium peroxides. *Thermochimica Acta*, 255:143–154, 1995.
- [132] W. van Burik. JOG-properties in MOX-fuel, February 2021. TU Delft, Master thesis.
- [133] W.J.M. van der Kemp, J.G. Blok, P.R. van der Linde, H.A.J. Oonk, A. Schuijff, and M.L. Verdonk. Binary alkaline earth mixtures: estimation of the excess thermodynamic properties and calculation of the phase diagrams. *Calphad*, 18:255–267, 1994.
- [134] W.J.M. van der Kemp, H.A.J. Oonk, C. Bergman, and R. Chastel. Determination of the excess molar gibbs energy of $(1-x)\text{BaO} + x\text{SrO}(s)$ by means of knudsen-effusion mass spectrometry. *J. Chem. Thermodynamics*, 24:857–862, 1992.

- [135] M.A. Veen. Class: Crystallography II. *Structure/ Property Relationships of Advanced Chemical products*, 12 2018. TU Delft.
- [136] M.A. Veen. Class: Crystallography III. *Structure/ Property Relationships of Advanced Chemical products*, 12 2018. TU Delft.
- [137] E.V. Tkachenko V.M. Zhukovskii and T.A. Rakova. Phase diagrams of the systems MoO_3 - MeMoO_4 (Me = Mg, Ca, Sr, Ba). *Russ. J. Inorg. Chem.*, 12:1734–1736, 1970.
- [138] G. Wallez, P.E. Raison, A.L. Smith, N. Clavier, and N. Dacheux. High-temperature behavior of dicesium molybdate Cs_2MoO_4 : Implications for fast neutron reactors. *Journal of Solid State Chemistry*, 215:225–230, 2014.
- [139] X. Xu, Y. Pan, Y. Zhong, L. Ge, S.P. Jiang, and Z. Shao. From scheelite BaMoO_4 to perovskite BaMoO_3 : Enhanced electrocatalysis toward the hydrogen evolution in alkaline media. *Composites Part B*, 198, 10 2020.
- [140] Ye.K., Yu.V. Tsvetkov, I.O. Samoiloova, G.K. Astahova, and A.A. Kazenas Petrov. Mass spectrometric study of barium molybdate sublimation. *Russian Metallurgy*, 1:14–17, 2003.
- [141] S. Zhou, R. Arroyave, C.A. Randall, and Z.-K. Liu. Thermodynamic modeling of the binary barium - oxygen system. *J. Am. Ceram. Soc.*, 88:1943–1948, 2005.
- [142] E. Zimmermann, K. Hack, and D. Neuschütz. Thermochemical assessment of the binary system Ba-O. *Calphad*, 19:119–127, 1995.
- [143] P. Zugenmaier. *X-ray analysis of partial crystalline fibre structure*, volume 1, chapter 3, pages 46–120. Woodhead Publishing, 1 edition, 10 2009.

Appendices

Appendix A

Partially successful synthesis methods

The results of the partially successful synthesis methods described in table 3.1 in chapter 3 are discussed here. This table is repeated here for clarity.

Table A.1: Synthesis conditions

| Compound | Starting reagents ^a | Atmosphere ^b | Crucible | Conditions ^c | Result |
|--|---|-------------------------|--------------------------------|---|----------------------|
| BaMoO ₄ | BaCO ₃ + MoO ₃ | Air | Al ₂ O ₃ | 2 cycles for 12h at 973K ^d | Successful |
| BaMo ₃ O ₁₀ | BaMoO ₄ + 2MoO ₃ | O ₂ | Platinum | 1 cycle for 12h at 823K and 2h at 993K and 3 cycles at 823K for 12h each. | Partially successful |
| | | O ₂ | Platinum | 3 cycles for 12h at 823K | Partially successful |
| | BaCO ₃ + MoO ₃ | Air | Platinum | 1 cycle for 4 days at 893K and 1 cycle for 2 days at 893K | Successful |
| Ba ₂ MoO ₅ | BaMoO ₄ + BaO | O ₂ | Al ₂ O ₃ | 3 cycles for 12h at 1473K | Partially successful |
| | | O ₂ | Al ₂ O ₃ | 2 cycles for 12h at 1273K | Successful |
| Ba ₃ MoO ₆ | BaMoO ₄ + BaO | O ₂ | Al ₂ O ₃ | 2 cycles for 12h at 1273K | Partially successful |
| | Ba ₂ MoO ₅ + BaO | O ₂ | Al ₂ O ₃ | 3 cycles for 12h at 1273K | Partially successful |
| Cs ₂ MoO ₄ | Cs ₂ CO ₃ + BaO | O ₂ | Al ₂ O ₃ | 2 cycles for 12h at 973K | Successful |
| BaCs ₂ (MoO ₄) ₂ | BaMoO ₄ + Cs ₂ MoO ₄ | O ₂ | Al ₂ O ₃ | 3 cycles for 24h, 14h and 24h at 1023K ^e | Successful |

^aAll mixtures were mixed and ground for 15 minutes using a mortar and pestle to ensure a homogeneous mixture.

^bAll in high-temperature furnaces. O₂: Ceradel tubular furnace, model PTF 12/50/250, air: Borel furnace, model TL1100-6.

^cAlways a 15 minute regrinding step in between cycles.

^dInitially attempted at 1073K, but this caused melting of MoO₃ (MP = 1074K [38])

^eNumber of cycles was not specified by Smith et al. [123], 3 cycles were chosen for practical reasons.

A.1 BaMo₃O₁₀



Two variations of this method were tried, that were unfortunately only partially successful. Table A.2 provides an overview of both variations for clarity:

Table A.2: Overview of the two variations that were done for the method 1 BaMo₃O₁₀ synthesis

| Variation 1 | Variation 2 |
|---|---|
| 1 cycle for 12h at 823K and 2h at 993K and 3 cycles at 823K for 12h each, all under O ₂ atmosphere | 3 cycles at 823K for 12h each under O ₂ atmosphere |
| Partially successful | Partially successful |

Variation 1: Partially successful

This variation is based on the method used by Lex Herrmann in his thesis [53]. BaMoO₄ and MoO₃ were mixed in stoichiometric ratio, ground for 15 minutes and heated under O₂ atmosphere for 1 cycle for 12h at 823K and for 2h at 993K in two platinum crucibles (150 mg per crucible).

When it came out of the oven, the compound looked yellow and crystallised inside the platinum crucibles. It became whiter during grinding but kept a slight yellow hue. As can be seen from the Rietveld refinement in figure A.1, the sample was not pure. There are missing peaks around 13, 23, 26, 28 and 43°. A Rietveld analysis of this data with two phases (BaMo₃O₁₀ and BaMoO₄) was attempted, but it failed to converge (probably due to the large amount of atomic positions that BaMo₃O₁₀ has). Powder-cell analysis (Appendix: figures B.1 and B.2) shows that there is still some BaMoO₄ (28 and 43 degrees) and MoO₃ (13, 23 and 26°) present in the mixture.

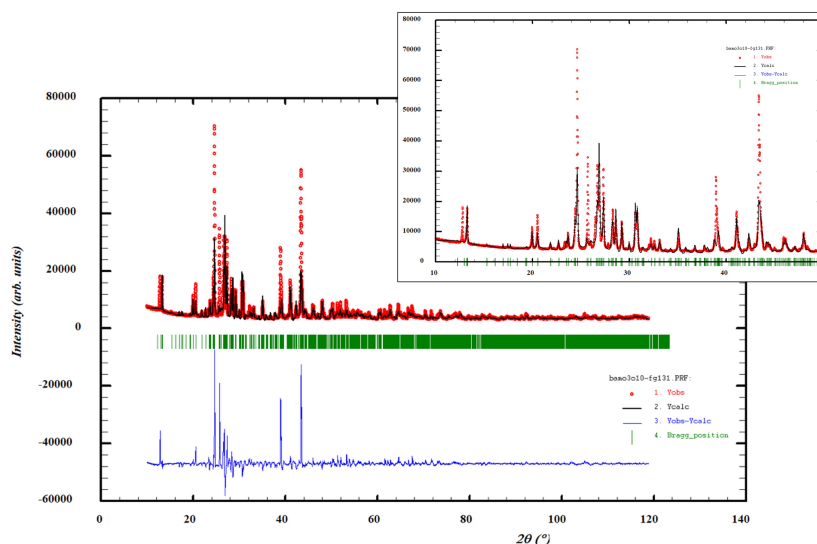


Figure A.1: Rietveld refinement of BaMo₃O₁₀ after 1 cycle with a zoomed in section between 10 and 50 degrees ($\chi^2 = 136.2$). Comparison between the observed (Y_{obs} , in red) and calculated (Y_{calc} , in black) X-ray diffraction patterns. $Y_{\text{obs}} - Y_{\text{calc}}$, in blue, is the difference between the experimental and calculated intensities. The Bragg's reflection angular positions are marked in green.

According to Smith et al. [120], the synthesis should include one more cycle at 823K for 12h under O₂ atmosphere. This second cycle was done (at a 5K/min heating and cooling rate) with two platinum crucibles (± 130 mg each). Rietveld refinement showed that the missing peaks at 13 and 23 degrees have disappeared, while the peaks at 26, 28 and 43 degrees have a lower intensity. This indicates that MoO₃ and BaMoO₄ are still present.

Because an extra cycle improved the purity of the sample, a third cycle was done with ± 125 mg in each platinum crucible. The Rietveld refinement showed that the peak at 28 degrees (BaMoO₄) has disappeared, but the peaks at 26 (MoO₃) and 43 (BaMoO₄) degrees are still visible.

Unsurprisingly, a fourth cycle was carried out (± 110 mg in each crucible) to see whether the purity could be improved further. The Rietveld refinement is shown in figure A.2. Both missing peaks are still visible, but the remainder of the XRD pattern appears to be in good alignment with the pattern made by the FullProf programme. No additional cycle was done, since the purity increase after the two extra cycles was not significant enough to suggest that another cycle would be useful.

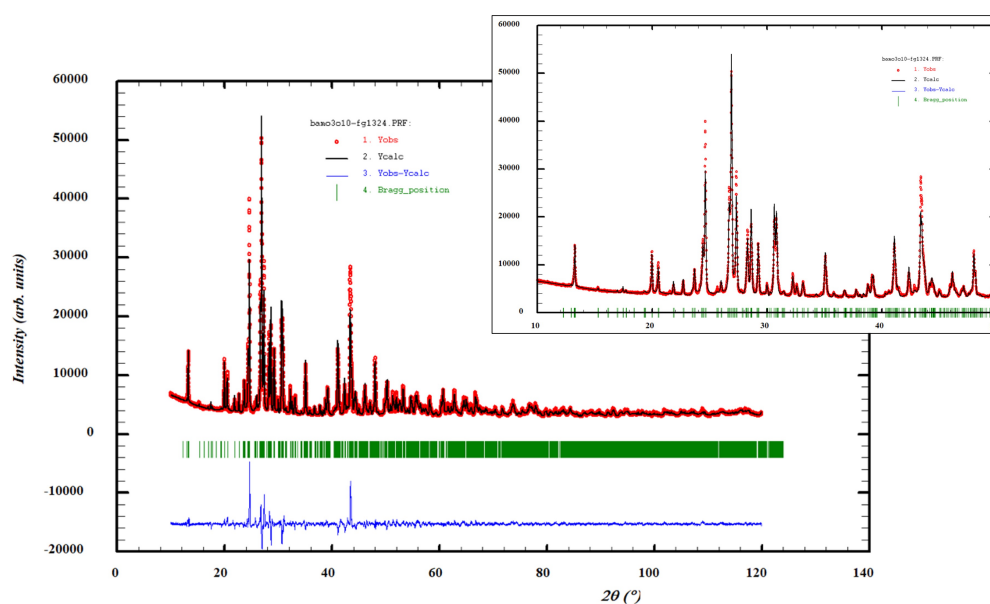


Figure A.2: Rietveld refinement of BaMo₃O₁₀ after 4 cycles with a zoomed in section between 10 and 50 degrees ($\chi^2 = 39.5$). Comparison between the observed (Y_{obs} , in red) and calculated (Y_{calc} , in black) X-ray diffraction patterns. $Y_{obs} - Y_{calc}$, in blue, is the difference between the experimental and calculated intensities. The Bragg's reflection angular positions are marked in green.

It is strange why the method described by Lex Herrmann [53] and Smith et al. [120] did not yield a pure sample. The reagents used for this synthesis were pure (BaMoO₄ was synthesised according to the method described above and MoO₃ was bought), so there could have been no contamination resulting from these compounds.

This thesis considers two probable causes. One, the platinum crucibles contained too much of the reagent mixture, causing only a part of the reagents to react. Second, the synthesis temperature was too high, causing part of the mixture to melt. The latter is supported by the crystals that formed in the platinum crucible after the last heating cycle up to 993K. The melting points of BaMo₃O₁₀ (predicted

to be 1056K by the Thermo-Calc model) and MoO_3 (1074K [38]) are both quite close to the maximum synthesis temperature. MoO_3 is also volatile and has been found to evaporate at temperatures near its melting point (as found during the synthesis of BaMoO_4). Evaporated MoO_3 unbalances the stoichiometric ratio with BaMoO_4 , leaving some of the reagents unreacted and decreasing the purity of the end-product.

A.1.1 Variation 2: partially successful

To test the two reasons mentioned above, a second variation of this synthesis was done. To keep the amount of changed variables to a minimum, the originally ground unreacted reagent mixture was used. A smaller amount of mixture (90 mg instead of 150 mg) was added to each platinum crucible, which was heated under O_2 atmosphere for two cycles at 823K for 12h with a regrinding step in between. After the synthesis, the powder was easily removable from the crucibles and contained no crystals. The resulting Rietveld can be seen in figure A.3.

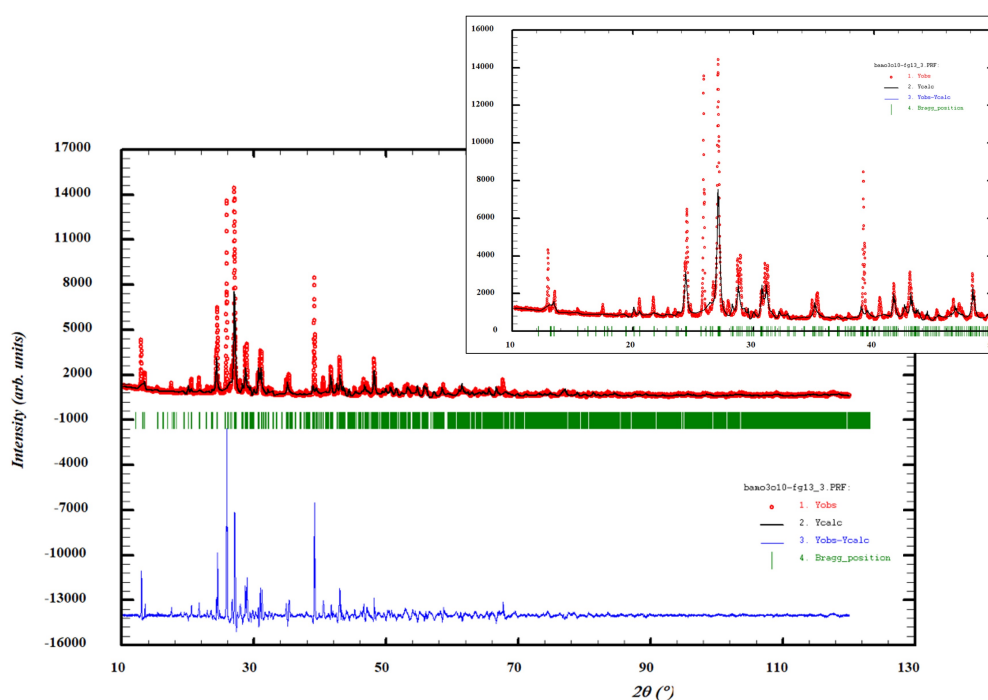


Figure A.3: Rietveld refinement of $\text{BaMo}_3\text{O}_{10}$ after 2 cycles with a zoomed in section between 10 and 50 degrees ($\chi^2 = 44.4$). Comparison between the observed (Y_{obs} , in red) and calculated (Y_{calc} , in black) X-ray diffraction patterns. $Y_{\text{obs}} - Y_{\text{calc}}$, in blue, is the difference between the experimental and calculated intensities. The Bragg's reflection angular positions are marked in green.

Figure A.3 shows that two cycles of this variation also did not result in a pure product. The same missing peaks are still present. Therefore, a third cycle was done at 823K for 12h and at 993K for 2h. The sample stuck to the inside to the crucibles and was very difficult to extract (figure A.4), implying that it had melted (just like during the first variation). The Rietveld analysis is shown in figure A.5. The third cycle does seem to have decreased the intensity of the missing peaks, but the sample is still not pure. A powdercell analysis can be found in the Appendix (figure B.3).



Figure A.4: Picture of two platinum crucibles with $\text{BaMo}_3\text{O}_{10}$ batch FG13.3 after the third cycle in the oven

From this it can be concluded that the $\pm 150\text{mg}$ per crucible was not the problem during the first synthesis, but that the higher 2h synthesis temperature should be decreased. The recommendation is to try 973K , since that is enough to prevent the MoO_3 from melting or evaporating during the $\text{BaCO}_3 + \text{MoO}_3 \rightarrow \text{BaMoO}_4$ synthesis, which resulted in a pure product.

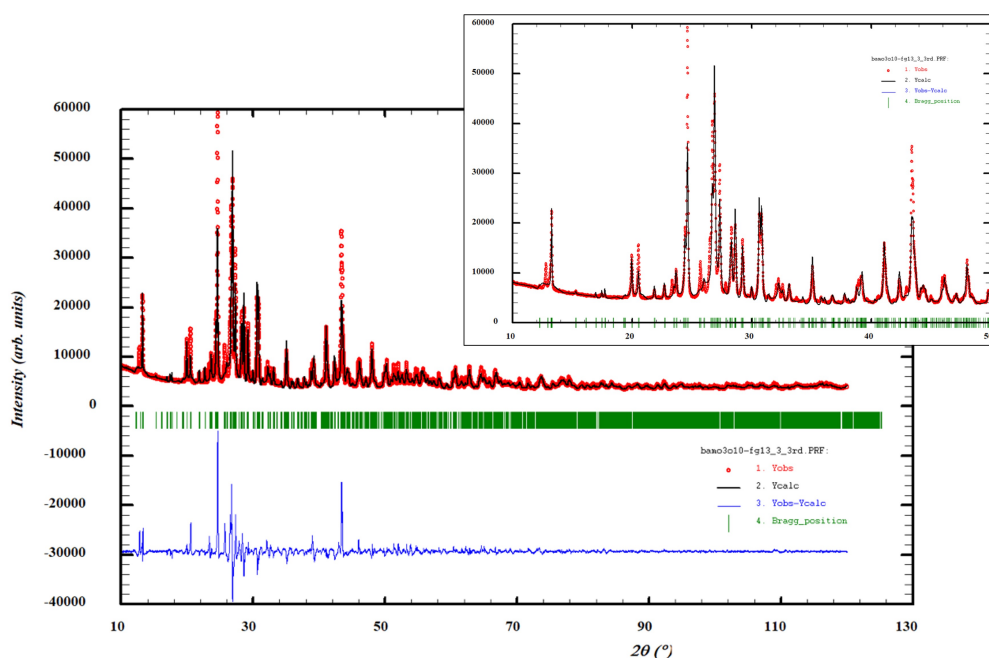


Figure A.5: Rietveld refinement of $\text{BaMo}_3\text{O}_{10}$ after 3 cycles with a zoomed in section between 10 and 50 degrees ($\chi^2 = 51.6$). Comparison between the observed (Y_{obs} , in red) and calculated (Y_{calc} , in black) X-ray diffraction patterns. $Y_{\text{obs}} - Y_{\text{calc}}$, in blue, is the difference between the experimental and calculated intensities. The Bragg's reflection angular positions are marked in green.

A.2 Ba_2MoO_5



This method was based on Lex Herrmann's thesis [53] where it was partially successful, resulting in a mixture of BaMoO_4 and Ba_2MoO_5 . The method was repeated here by mixing BaMoO_4 and BaO in a

1:1 ratio and grinding them for 15 minutes with a mortar and pestle. 300 mg of the mixture was added to a large aluminum oxide crucible and placed in the O₂ oven for two cycles at 1473K for 12h with a 15 minute regrinding step in between. The resulting powder was brown and consisted of hard clumps (figure A.6). After grinding, the texture became softer and the colour also lightened.



Figure A.6: Picture of aluminum oxide crucible with Ba₂MoO₅ after the first cycle in the oven

The Rietveld analysis is shown in figure A.7. Several large peaks in the graph do not correspond to the Ba₂MoO₅ structure (with missing peaks around 27 and 32 degrees) indicating that is another compound present.

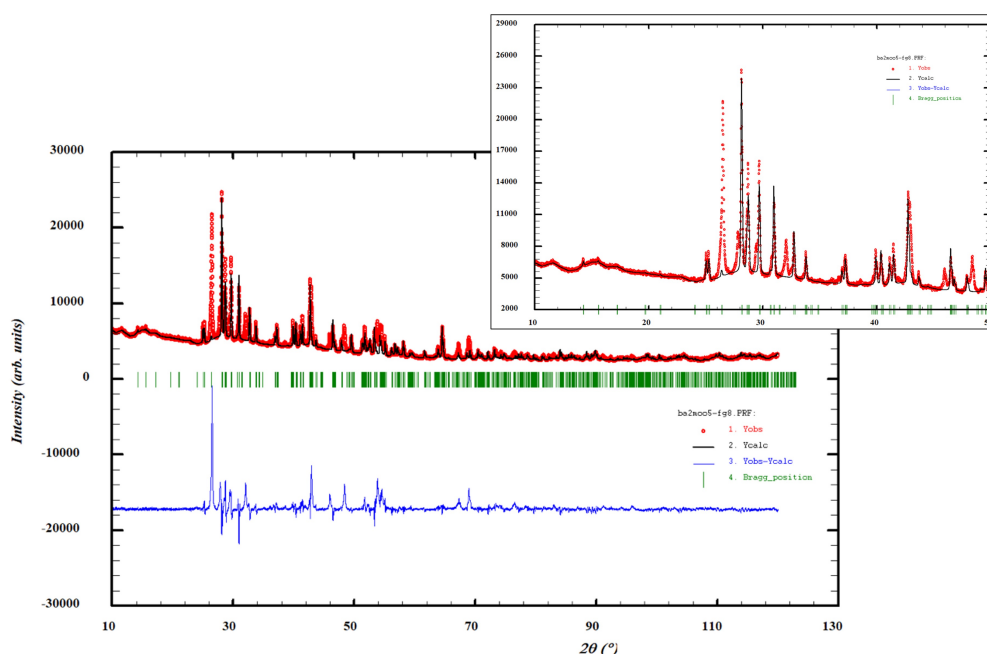


Figure A.7: Rietveld refinement of Ba₂MoO₅ after 1 cycle with a zoomed in section between 10 and 50 degrees ($\chi^2 = 56.3$). Comparison between the observed (Y_{obs} , in red) and calculated (Y_{calc} , in black) X-ray diffraction patterns. $Y_{obs} - Y_{calc}$, in blue, is the difference between the experimental and calculated intensities. The Bragg's reflection angular positions are marked in green.

A three-phase refinement was done (with BaMoO₄, BaO and Ba₂MoO₅) which showed that the sample consisted of 62.9 ± 0.4 % Ba₂MoO₅, 33.8 ± 0.3 % BaMoO₄ and 3.3 ± 0.4 % BaO.

An extra cycle was done at 1473K for 12h to test if this would improve the sample's purity. When it came out of the oven, the powder looked much the same as it had before and became lighter again

after grinding. The Rietveld refinement showed no noticeable improvement (figure A.8). Interestingly, a three-phase Rietveld analysis showed that the percentage of BaMoO_4 had increased to $55.5 \pm 0.3 \%$ (figure A.8) (Ba_2MoO_5 : $43.9 \pm 0.3\%$ and BaO : $0.6 \pm 0.1\%$). This implied that Ba_2MoO_5 had decomposed after it was formed and that the temperature of the synthesis was probably too high. Therefore, a second method was attempted with a lower synthesis temperature.

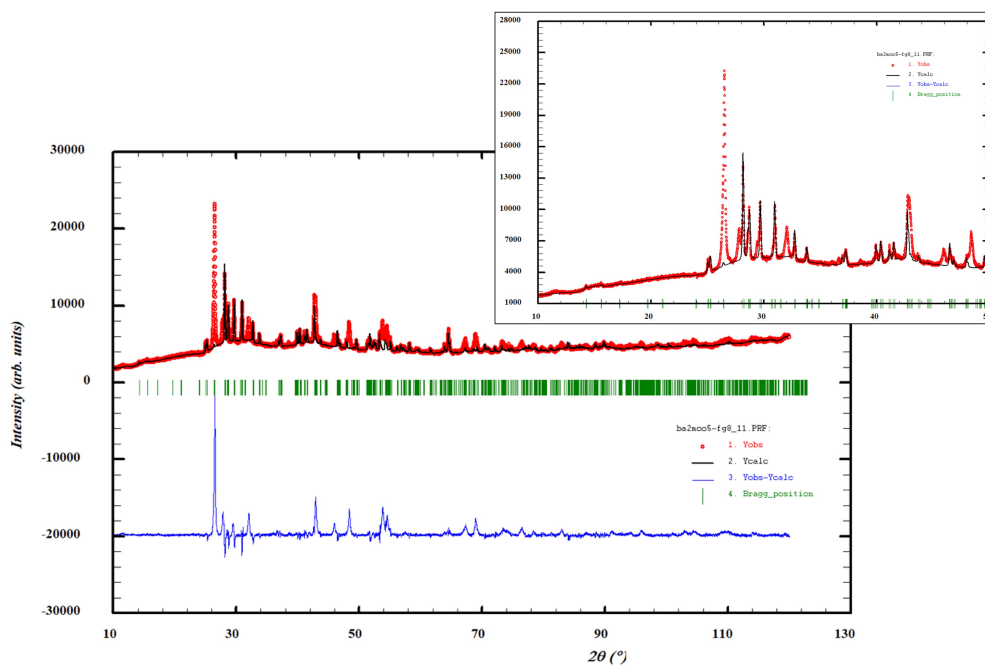


Figure A.8: Rietveld refinement of Ba_2MoO_5 after 1 cycle with a zoomed in section between 10 and 50 degrees ($\chi^2 = 56.0$). Comparison between the observed (Y_{obs} , in red) and calculated (Y_{calc} , in black) X-ray diffraction patterns. $Y_{\text{obs}} - Y_{\text{calc}}$, in blue, is the difference between the experimental and calculated intensities. The Bragg's reflection angular positions are marked in green.

Appendix B

Additional Rietveld and PowderCell analyses

Additional Rietveld and Powdercell analyses from chapter 4

B.1 $\text{BaMo}_3\text{O}_{10}$

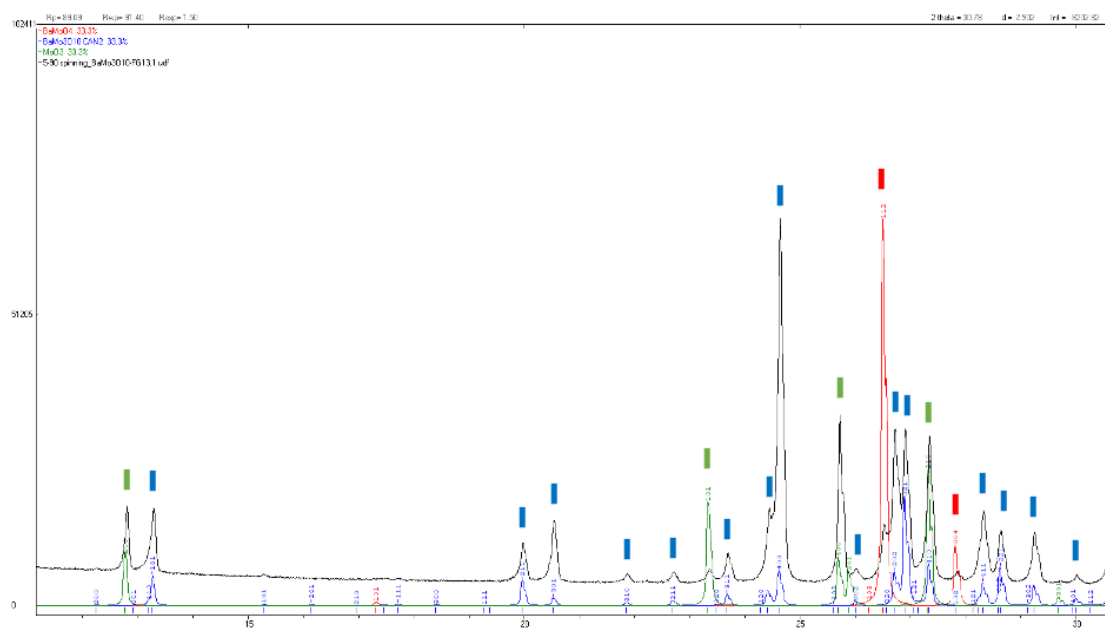


Figure B.1: Powdercell analysis of $\text{BaMo}_3\text{O}_{10}$ batch FG13.1 (in blue) with BaMo_4 in red and MoO_3 in green between 5 and 30 degrees. The sample still contains BaMo_4 and MoO_3

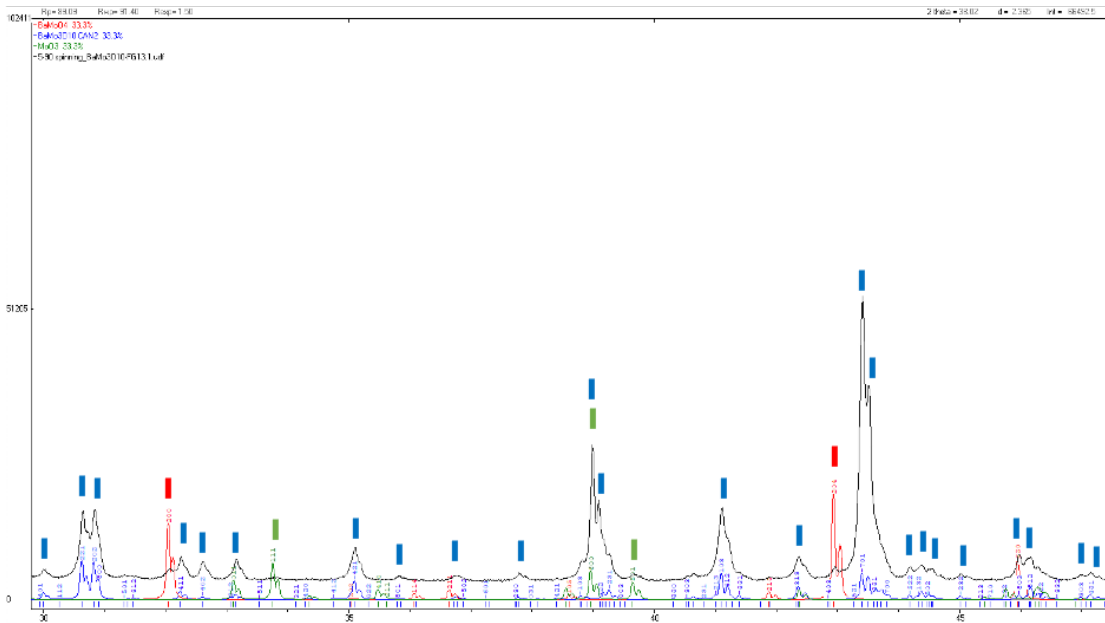


Figure B.2: Powdercell analysis of BaMo₃O₁₀ batch FG13.1 (in blue) with BaMoO₄ in red and MoO₃ in green between 30 and 50 degrees. The sample still contains BaMoO₄ and MoO₃

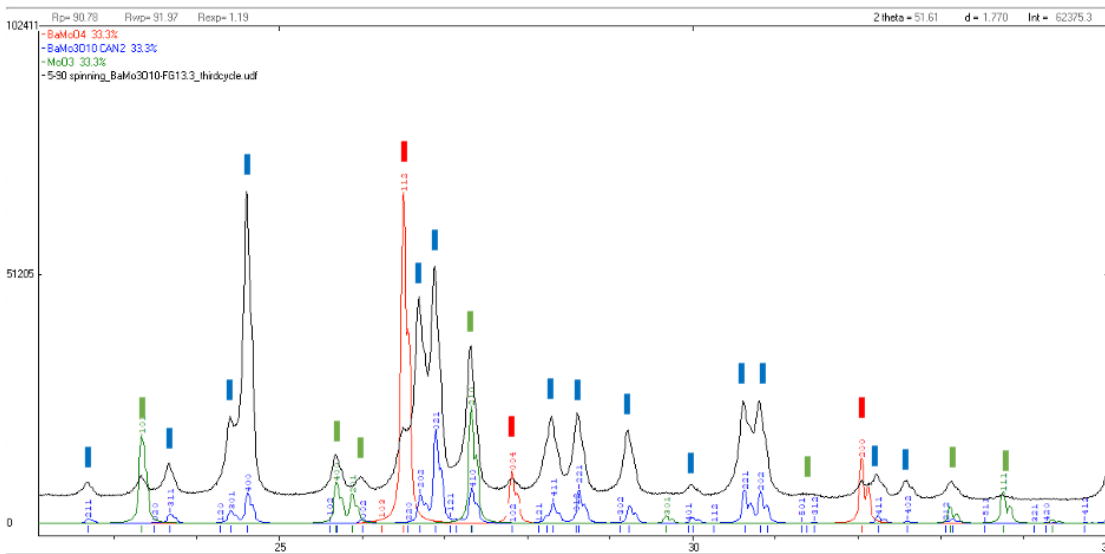


Figure B.3: Powdercell analysis of BaMo₃O₁₀ batch FG13.3 after 3 cycles (in blue) with BaMoO₄ in red and MoO₃ in green between 22 and 35 degrees. The sample still contains BaMoO₄ and MoO₃

B.2 Ba₂MoO₅

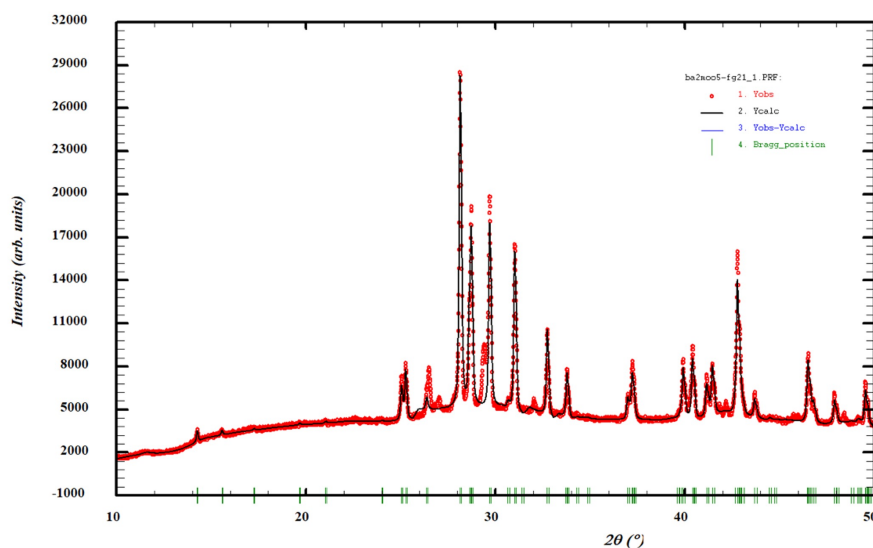


Figure B.4: Rietveld analysis of Ba₂MoO₅ after one cycle ($\chi^2 = 11.02$). Comparison between the observed (Y_{obs} , in red) and calculated (Y_{calc} , in black) X-ray diffraction patterns. $Y_{\text{obs}} - Y_{\text{calc}}$, in blue, is the difference between the experimental and calculated intensities. The Bragg's reflection angular positions are marked in green.

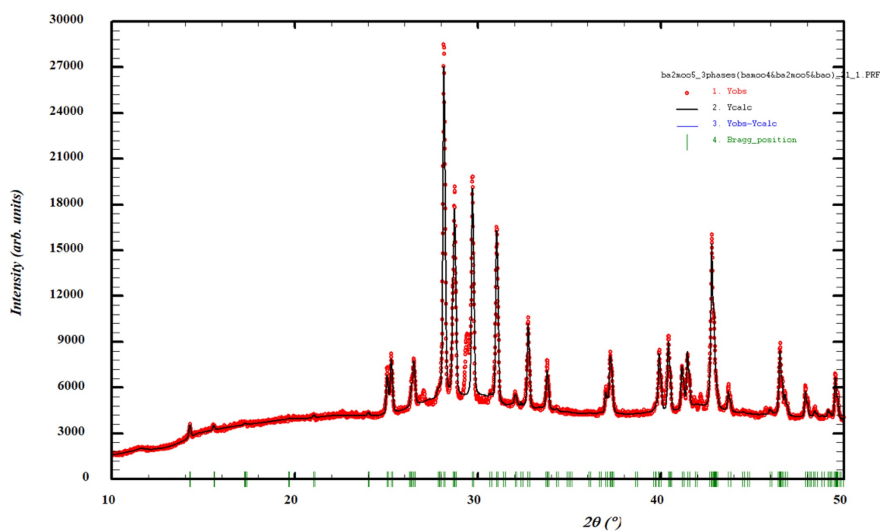


Figure B.5: Three-phase rietveld analysis of Ba₂MoO₅ after one cycle, with Ba₂MoO₅, BaMoO₄ and BaO ($\chi^2 = 7.67$). Comparison between the observed (Y_{obs} , in red) and calculated (Y_{calc} , in black) X-ray diffraction patterns. $Y_{\text{obs}} - Y_{\text{calc}}$, in blue, is the difference between the experimental and calculated intensities. The Bragg's reflection angular positions are marked in green.

Appendix C

Outlying data point discussions

C.1 Ba-Mo-O system

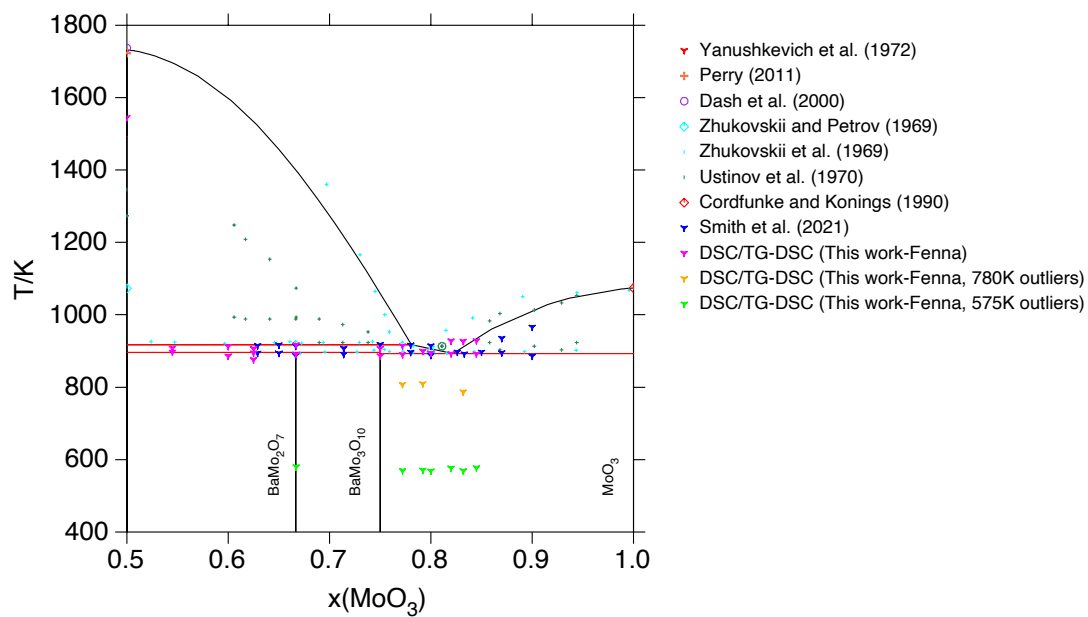


Figure C.1: BaMo₄ - MoO₃ phase diagram with all TGDSC results collected in this work (pink symbols), showing two sets of outlying peaks at ± 575 K (in green) and ± 780 K (in orange)

Figure C.1 shows the BaMo₄ - MoO₃ phase diagram with the collected TGDSC results. It is clear that not all data points follow the lines of the phase diagram model and these outliers will be discussed first. There are a set of ± 575 K outlying data points for all BaMo₃O₁₀ : MoO₃ compositions (average temperature = 579.41 K with a standard deviation of 9.16K) as well as a set of ± 780 K outlying data points showing at $x(\text{MoO}_3) = 0.772, 0.792$ and 0.832 (average temperature = 782.29K with a standard

deviation of 28.02K). Only compositions with BaMoO_4 and $\text{BaMo}_3\text{O}_{10}$ in the area $0.50 \leq x \leq 0.75$ have no outlying data points.

A Powdercell analysis of the XRD patterns of these compositions (table 3.11) revealed notable unidentified impurities (U.I.s) for compositions at $x(\text{MoO}_3) = 0.792, 0.80$ and 0.845 . It is possible for these impurities to interfere with the TGDSC measurement and to cause unwanted thermal events to occur. The compositions with a U.I. however are not the only compositions with outlying data points, so there must be another explanation. The most evident reason seems to be contaminated MoO_3 , since outlying peaks only occur for compositions with MoO_3 (especially the $\pm 575\text{K}$ data points).

To find the reason behind these outlying data points, a measurement case study was performed using the $x(\text{MoO}_3) = 0.792$ composition (because it had both outlying peaks and the U.I.). The following experiments were carried out:

1. A blank measurement with the empty DSC crucible to determine if it was contaminated
2. A measurement with pure MoO_3 without BN up to 863K to test if it was contaminated
3. A new $x(\text{MoO}_3) = 0.792$ composition measurement with a different $\text{BaMo}_3\text{O}_{10}$ batch, in case the previous one contained any undetected contaminating compound
4. A measurement with only BN powder
5. A measurement of the dried BN powder
6. A new $x(\text{MoO}_3) = 0.792$ composition measurement with BN that was dried in the air furnace (and with the same $\text{BaMo}_3\text{O}_{10}$ batch as 3.)
7. A new $x(\text{MoO}_3) = 0.792$ composition measurement with no BN powder up to 693K to see if the first $\pm 575\text{K}$ peak would be visible (with the same $\text{BaMo}_3\text{O}_{10}$ batch as 3.)

Measurements without BN powder were conducted approximately 100K below the melting point of the sample to prevent it from reacting with the crucible. The results of the measurements were as follows. The (1.) empty DSC crucible measurement showed no peaks, confirming that the crucible was not contaminated. The (2.) MoO_3 measurement showed a clear peak at $801.8 \pm 5\text{K}$. According to the phase diagram model there should be no event at this temperature. This event fits within the parameters of the $\pm 780\text{K}$ outlying points in figure C.1 and could therefore explain the outlying data points there. It is however curious why this peak does not occur for all MoO_3 compositions.

The (3.) measurement with a different batch of $\text{BaMo}_3\text{O}_{10}$ did not show the $\pm 780\text{K}$ event (but it did show the $\pm 575\text{K}$ peak). The $\pm 780\text{K}$ event was detected for two other compositions (at $x(\text{MoO}_3) = 0.772$ and 0.832) that both used different batches of $\text{BaMo}_3\text{O}_{10}$. These batches were also used for other compositions that did not show the $\pm 780\text{K}$ peaks. Therefore, it is doubtful that the occurrence of the $\pm 780\text{K}$ peaks is linked to a contaminated batch of $\text{BaMo}_3\text{O}_{10}$.

The (4.) measurement with only BN powder did not show any significant peaks, although there was some noise in the heating and cooling curves around 788K and 743K respectively. Therefore, the decision was made to dry some of the BN powder for 18h at 673K in order to remove any water that it might contain. Water could interfere with the sample during the measurement, resulting in outlying peaks. The (5.) TGDSC measurement of the dried BN powder showed small (but distinct) peaks around the same two temperatures. The drying process appeared to have made the problem worse. This could be associated with a contamination that was present in the air furnace or the crucible that the BN was dried in. To see if the dried powder had an effect, it was used during the next measurement.

The (6.) measurement with the $x(\text{MoO}_3) = 0.792$ composition (and the dried BN powder) showed

peaks around 780K, like the DSC curves of the dried BN. However, no $\pm 575\text{K}$ event was detected. This indicates that the water hypothesis was correct and that drying the BN powder solved the $\pm 575\text{K}$ outlying data points. To be certain that $\text{BaMo}_3\text{O}_{10}$ or MoO_3 were not causing the $\pm 575\text{K}$ event, a last measurement (7.) with the $x(\text{MoO}_3) = 0.792$ composition was done, without BN and up to 693K . This temperature was chosen because it was below the melting points of both compounds so that they could be tested without the potential interference of BN and because the 575K peak would be visible, but the 780K peak would not. The resulting measurement did not show any peaks, therefore suggesting that the $\pm 575\text{K}$ events were not due to either $\text{BaMo}_3\text{O}_{10}$ or MoO_3 .

To summarise, it seems likely that the $\pm 575\text{K}$ and $\pm 780\text{K}$ data points are due to a contamination in BN and MoO_3 respectively. It is unclear why the $\pm 780\text{K}$ events were not detected during all $\text{BaMo}_3\text{O}_{10} : \text{MoO}_3$ TGDSC measurements, or why drying the BN powder made its outlying peaks more noticeable. It is recommended to buy new MoO_3 and BN and to test it with a DSC measurement. Because the current MoO_3 and BN powders have probably been used for some time, contamination from a dirty spatula or crucible is not inconceivable.

C.2 $\text{BaMoO}_4 - \text{Cs}_2\text{MoO}_4$ system

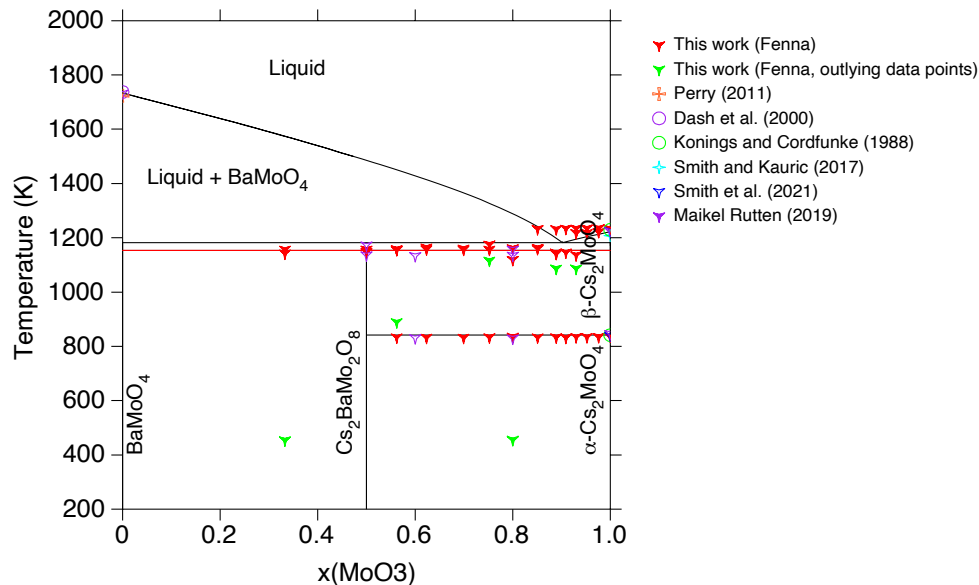


Figure C.2: Initial CALPHAD model with all TGDSC results and outlying peaks marked by green symbols. Data points by Perry [98], Dash et al. [96], Konings and Cordfunke [38] and Smith and Kauric [119] and Smith et al. [121]

XRD analysis of the TGDSC samples showed the presence of Cs_2O in compositions $x(\text{Cs}_2\text{MoO}_4) = 0.699, 0.80, 0.851, 0.889, 0.909$ and 0.952 . This is probably due to a small amount of decomposition of $\text{BaCs}_2(\text{MoO}_4)_2$. Looking at the Cs - O phase diagram (figure C.3) [69, 91], the Cs_2O peritectic event at 768K does not come close to matching any of the outlying data points. Moreover, it is unlikely that the quantity of this impurity would be significant enough to be detected by a TGDSC measurement.

Therefore it can be concluded that the outlying data points are not due to the presence of Cs_2O in the sample.

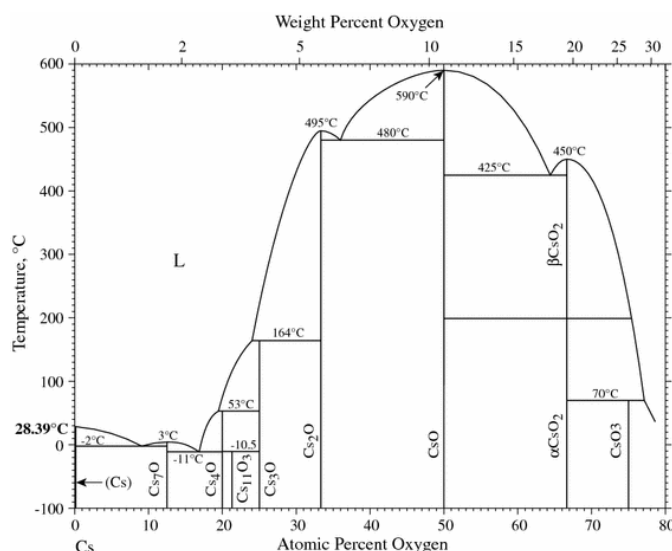


Figure C.3: Cs-O phase diagram as described by C.F Knights et al. [69] and H. Okamoto [91]

To see if the outlying data points could be caused by a specific batch of Cs_2MoO_4 (even though there is no apparent pattern), a contamination of the DSC crucible or the Al_2O_3 powder, the following experiments were done:

1. Measurement with pure Cs_2MoO_4
2. A blank measurement with an empty DSC crucible
3. A measurement with only Al_2O_3 powder
4. A measurement with newly bought Al_2O_3 powder
5. A measurement with dried new Al_2O_3 powder

The results were as follows. There were no unexpected peaks in the (1.) measurement with Cs_2MoO_4 or the (2.) blank measurement with an empty DSC crucible. Both (3. and 4.) measurements with Al_2O_3 powder (the old and the new) showed a peak around 455K comparable to the $\pm 455\text{K}$ peaks for $x(\text{Cs}_2\text{MoO}_4) = 0.333$ and 0.80. These peaks disappeared when Al_2O_3 was dried in the O_2 oven for 14h at 675K (5. measurement), indicating that they were caused by water present in the Al_2O_3 powder.

These measurements did not give any indication as to the origin of the other outlying peaks that are shown in figure C.2. There are however, multiple observations that might form some form of explanation. Firstly, the best and cleanest TGDSC patterns resulted from samples made with Al_2O_3 powder that had previously done four cycles of testing in the TGDSC. In theory, there should be no difference between the powder that was dried in the oven and the powder that was submitted to four cycles in the TGDSC (both in O_2 and up to 1373K), but still the results are cleaner with Al_2O_3 from the TGDSC.

Secondly, repeated measurements with the same composition often showed a different pattern. The general outline would be the same, but it was possible for an additional outlying peak to occur or

for a previous outlying peak to disappear with no clear explanation. These repeated measurements would be done with a different batch of Cs_2MoO_4 or $\text{BaCs}_2(\text{MoO}_4)_2$, which could mean that one batch contained some form of contamination causing unexpected events to occur. That is very unlikely however, since all batches were tested for purity after their synthesis by means of XRD and subsequent Rietveld analysis. If there were any significant contaminations they would have been detected. Also, the same batches of Cs_2MoO_4 and $\text{BaCs}_2(\text{MoO}_4)_2$ were used for many different measurements, all of which would then be expected to show the same outlying peak(s). This was not the case. Therefore, it can be concluded with some certainty that the outlying peaks shown in figure C.2 were not caused by contaminations in the $\text{BaCs}_2(\text{MoO}_4)_2$ and Cs_2MoO_4 batches.

Thirdly, first cycle DSC results can sometimes be unusual, with unexpected peaks or noise in the heating curve. Normally, a 1 cycle measurement is done before a 4 cycle measurement to check if the set temperature is correct (to see whether or not all expected events are detected within the set temperature range) and its results are not considered in the analysis of the DSC data. However, since only first cycle measurements of the BaMoO_4 - Cs_2MoO_4 system are possible, the final data analysis could contain some strange 1st cycle peaks.

Finally, weight loss was detected for some compositions with a higher amount of Cs_2MoO_4 after approximately 1120 - 1175K. This is probably connected to the melting of Cs_2MoO_4 (MP = $1229.5 \pm 0.2\text{K}$ [108]) resulting in a small amount of evaporation. This phenomenon was also observed during the pure Cs_2MoO_4 measurement (figure C.4). Weight loss and melting could complicate the transitions that occur in the DSC crucible and result in unexpected peaks. Because the model of this phase diagram is so new and only based on two sets of data, it is difficult to determine which events are expected to occur and which events are outliers. The weight loss discussion could be relevant for the $\pm 1087\text{K}$ and 1116K outlying data points, since they occur in a similar temperature range, but it is not possible to be certain. It is also unclear why weight loss was detected only in some of the compositions with higher $x(\text{Cs}_2\text{MoO}_4)$ values.

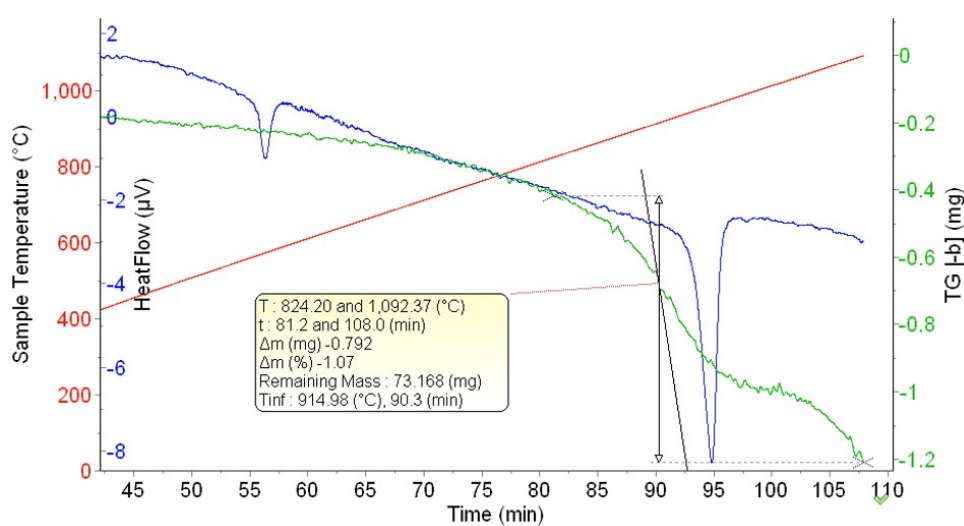


Figure C.4: Mass loss of the pure Cs_2MoO_4 TGDSC measurement normalised against a blank measurement with the same DSC crucible. Shows significant 0.79 mg mass loss during the last event.

To conclude this section, the $\pm 455\text{K}$ peaks are quite clearly caused by water contained in the Al_2O_3

powder, since they disappear after the powder has been dried. The remaining outlying peaks might have occurred due to a combination of the observations listed above, but it is not possible to determine a definitive reason for them. Multiple measurements of the same compositions could provide clarity and statistically significant data, possibly with a capped DSC crucible to prevent some of the weight loss at higher $x(\text{Cs}_2\text{MoO}_4)$ values. It is strongly recommended to find a method to achieve a 4 cycle measurement, because this would eliminate first cycle noise and would give statistically significant results.

C.3 Sr-Mo-O system

It is clear that not all data points follow the lines of the phase diagram model. These outlying points will be addressed first. It seems that there are two groups: the first at $\pm 790\text{K}$ and the second at $\pm 855\text{K}$. In order to determine the reason for these peaks, the following measurements were done:

1. A blank measurement with the empty DSC crucible to see if it was contaminated
2. A $x(\text{MoO}_3) = 0.769$ composition measurement without BN up to 863K to test if the outlying peaks would still occur without BN
3. Pure SrMoO_4 without BN up to 1008K
4. Pure MoO_3 without BN up to 863K (same measurement as for $\text{BaMoO}_4 - \text{MoO}_3$ section)

The measurements without BN were performed approximately 100K under the melting point of MoO_3 (measurements 2. and 4.) and SrMoO_4 (measurement 3.) to prevent the sample from sticking to the crucible. Besides these listed measurements, two out of the four initial compositions ($x(\text{MoO}_3) = 0.781$ and 0.820) were measured with dried BN powder because it had already been dried for the $\text{BaMoO}_4 - \text{MoO}_3$ measurements at that time. Also, it was not possible to do measurements with a different SrMoO_4 or MoO_3 batch, because they were bought and had not been synthesised. It should also be mentioned that all outlying peaks were very small compared to the peaks representing expected events.

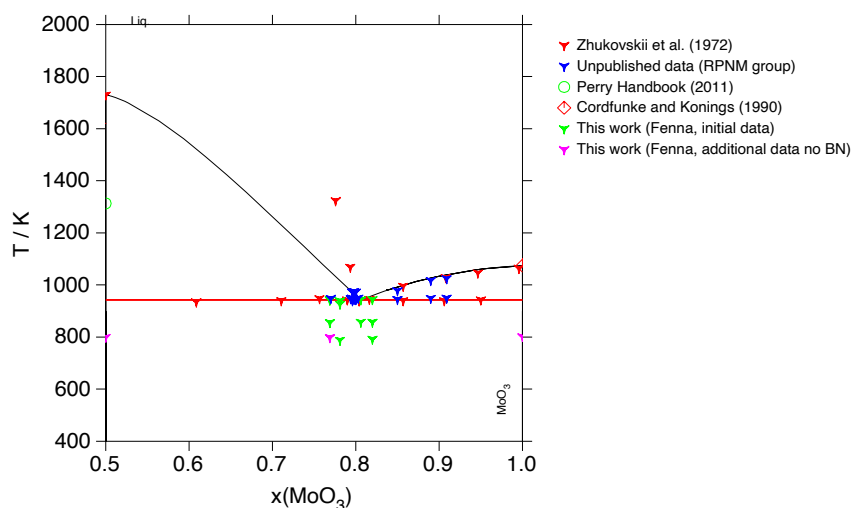


Figure C.5: $\text{SrMoO}_4 - \text{MoO}_3$ phase diagram including additional measurements without BN in pink

The results of these measurements are shown in figure C.5. The pink data points represent the measurements done without BN powder (2., 3. and 4.) and the green data points show the initial results depicted in figure 3.31. It is clear that all pink data points resemble the first outlying events at $\pm 790\text{K}$, suggesting that a contamination in SrMoO_4 and/or MoO_3 is causing them. The blank measurement (1.) did not show any peaks, so the DSC crucible was not contaminated.

The $\text{BaMoO}_4 - \text{MoO}_3$ TGDSC results (section 3.1.3.2) showed similar outlying peaks at $\pm 790\text{K}$ which were ascribed to a contamination in MoO_3 , although the tested BN powder (dried as well as undried) also showed a peak around 788K . It was ultimately concluded that MoO_3 was probably the culprit, because a composition measurement without BN showed the 780K outlying peak. Figure C.5 represents a similar picture, where all measurements without BN have the 790K peak, indicating that SrMoO_4 and MoO_3 are contaminated. It seems unlikely that both MoO_3 and SrMoO_4 contain enough of the same impurity that it would be detected by a TGDSC measurement, yet that is what these results suggest. BN possibly has the same impurity, since it shows a peak at the same temperature. XRD analysis of these TGDSC measurements did not show any contaminations (table 3.20).

It is interesting to mention that the $\text{BaMoO}_4 - \text{MoO}_3$ TGDSC results showed peaks at $\pm 575\text{K}$ that went away after the BN powder was dried and were thus assumed to be due to some water that it contained. The $\text{SrO} - \text{MoO}_3$ measurements that were done with undried BN (at $x(\text{MoO}_3) = 0.769$ and 0.806) did not show these $\pm 575\text{K}$ peaks.

The listed measurements did not show the cause of the outlying peaks at $\pm 850\text{K}$. It is unsatisfying not to be able to determine the reason behind many of the outlying data points, not only for the $\text{SrO} - \text{MoO}_3$ system, but for all phase diagrams that were discussed during this thesis. It seems unlikely that contaminations in either SrMoO_4 , MoO_3 or BN caused unexpected events to occur, but TGDSC measurements did detect these peaks, so they must be caused by something. It is recommended to repeat the four initial measurements in figure 3.31 with newly bought MoO_3 , SrMoO_4 and BN compounds to see whether the outlying peaks occur again.

Appendix D

Neumann-Kopp Approximation

D.1 Neumann-Kopp Approximation

The Neumann-Kopp rule states that “*Each element (in the solid state) has essentially the same specific or atomic heat in compounds as it has in the free state*” and can be expressed as such (considering compound $A_aB_bC_c$ that is formed by solid elements $A(s)$, $B(s)$ and $C(s)$):

$$aA(s) + bB(s) + cC(s) = A_aB_bC_c(s) \quad (D.1)$$

where,

$$C_{pm}(A_aB_bC_c, s) = aC_{pm}(A, s) + bC_{pm}(B, s) + cC_{pm}(C, s) \quad (D.2)$$

It can be modified to predict the heat capacity of a complex compound [58, 78, 102] for example for the solid compound $A_aB_bC_c$ that is formed in a reaction of solid binary compounds AC_{c1} and BC_{c2} :

$$aAC_{c1}(s) + bBC_{c2}(s) = A_aB_bC_c(s) \quad (D.3)$$

where,

$$C_{pm}(A_aB_bC_c, s) = aC_{pm}(AC_{c1}, s) + bC_{pm}(BC_{c2}, s) \quad (D.4)$$

In this case, $BaCs_2(MoO_4)_2$ can be described with a three sublattice model with Ba , Cs_2 and MoO_4 representing A , B and C respectively. This gives:



and

$$C_{pm}(BaCs_2(MoO_4)_2, s) = C_{pm}(BaMoO_4, s) + C_{pm}(Cs_2MoO_4, s) \quad (D.6)$$

The Neumann-Kopp rule was based on a C_{pm} data set collected at ambient temperatures, which is why the result can deviate from the experimental C_{pm} function at higher temperatures [58]. However, at this early modelling stage this is considered to be acceptable. The BaMoO_4 heat capacity function was taken from the TAF-ID project.

Combining the $\text{BaCs}_2(\text{MoO}_4)_2$ heat capacity function with the standard enthalpy of formation and standard entropy gives the calculated Gibbs energy function:

$$G^{\text{BaCs}_2(\text{MoO}_4)_2} [\text{J/mol}] = 298.15 - 3143399.04432646 + 1145.36339T - 217.6657 \cdot T \ln T - 0.1137012T^2 + 1.1719 \cdot 10^{-5}T^3 + 360152.95T^{-1} \quad (\text{D.7})$$